Piezoelectric Cantilever for Mechanical Energy Harvesting

by

Seon-Bae Kim

A dissertation submitted to the Graduate Faculty of
Auburn University
in partial fulfillment of the
requirements for the Degree of
Doctor of Philosophy

Auburn, Alabama
December 8, 2012

Keywords: Piezoelectric cantilever, energy harvesting, piezoelectric mode,
PZT cantilever, magnetic cantilever

Approved by

Dong-Joo Kim, Chair, Associate Professor of Materials Engineering
Zhongyang Cheng, Professor of Materials Engineering
Barton Prorok, Associate Professor of Materials Engineering
Subhash Sinha, Professor of Mechanical Engineering

Abstract

Renewable energy based power sources are of great interest in mobile and wireless devices due to limitations of capacity and disposal in chemical reaction based batteries. Piezoelectric energy harvester (PEH) is one of the most appropriate devices which can replace or back up the battery in such applications. The PEH converts vibration energy, typical form of mechanical energy, to electrical energy. However, harvested power density of the PEH is relatively low compared to other renewable energy based devices, which may be insufficient to operate current mobile and wireless devices. In addition, the operational frequency range of a linear PEH is too narrow for practical applications. Therefore, the operational frequency range needs to be expanded to harvest a wider range of environmental vibration.

In this dissertation, the improvement of the output power of PEH was investigated as functions of temperature and piezoelectric modes. Hybridization of piezoelectric material with magnetic material was also studied to expand the frequency range of harvested vibration.

The temperature effect on PEHs resulted in the degradation of the output power. Soft PZT based PEH degrades faster than the hard PZT based device up to about 100 $^{\circ}$C. Above 100 $^{\circ}$C with approaching T_c, the hard PZT based device appears to show faster degradation. In general, MEMS PEH degrades slower than bulk scale PEH. The most influential material parameter responsible for such degradation was the dielectric constant. Therefore, the reduction of the power density of the PEH at higher operating temperatures can be minimized by controlling the dielectric constant of a piezoelectric material

MEMS scale PZT cantilevers based on d_{33} and d_{31} mode were designed, fabricated and evaluated to compare the output power density of the devices depending on the piezoelectric mode; d_{33} and d_{31}. Since output power estimation model for d_{33} mode PEH has been rarely reported, a theoretical model was derived by combining Roundy's analytical model and conformal mapping method. The derived mathematical model was also verified by the experiment results. The d_{31} mode device produced higher output power density than the d_{33} mode device in the fabricated devices. However, theoretical modeling suggested that higher output power can be generated from d_{33} mode device when finger electrodes become narrower than those of the fabricated devices. Under optimal electrode design, the d_{33} mode device can offer higher efficiency output power conversion due to higher voltage than d_{31} mode device. The d_{33} mode device can exhibit higher output power with the narrow finger electrode design, so that the effective spacing/actual spacing of piezoelectric layer is less than one.

Piezoelectric ZnO cantilevers grown on magnetic substrates were fabricated to demonstrate harvesting vibration energy in a wide frequency range. Cu was doped to enhance piezoelectricity of ZnO thin films by lowering leakage current. The ZnO cantilever/magnetic substrate was vibrated driven by external magnetic force and showed energy harvesting from 20 Hz to 180 Hz vibration. Such a range covers almost the entire frequency range that is available in our environment.

Acknowledgments

First of all, I would like to thank my advisor, Dr. Dong-Joo Kim for not only his guidance in academic area, but also highly respectable generosity. His consideration and encouragement for me were the biggest support during my Ph. D study.

I would like to express my gratitude to my committee members, Dr. Zhongyang Cheng, Dr. Barton Prorok, Dr. Subhash Sinha, and Dr. Minseo Park. It was great time sharing and discussing with my previous and current lab members; Dr. Sang H. Yoon, Dr. Jung-Hyun Park, Dr. H. Clyde Wikle, Dr. Hosang Ahn, Dr. Dan Liu, Mr. Dong Liu, Mr. Jing Dai, Mr. Jaeyoung Jeong, Ms. Hyejin Park, Ms. Yoonsung Chung.

I would like to give appreciation to my family: my wife, Kyungmi Cho, for her unstinting support; my daughter, Kaylin, happiness of my life; my parents that I love.

Table of Contents

List of Tables

List of Figures

List of Abbreviations

ac	Alternative Current
AOE	Advanced Oxide Etcher
ASE	Advanced Silicon Etcher
dc	Direct Current
FWHM	Full Width Half Maximum
ICP	Inductively Coupled Plasma
IDE	InterDigital Electrode
MEMS	MicroElectroMecahnical Systems
MPB	Morphotropic Phase Boundary
OCV	Open Circuit Voltage
P-E	Polarization vs. Electric field
PEH	Piezoelectric Energy Harvester
PMN -PT	Pb(Mg1/3Nb2/3)O3-PbTiO3
PZN-PT	Pb(Zn1/3Nb2/3)O3-PbTiO3
PZT	Lead Zirconate Titanate
RF	Radio Frequency
RIE	Reactive Ion Etching
rms	Root Mean Square
SEM	Scanning Electron Microscope

SOI	Silicon On Insulator
TBE	Top and Bottom Electrode
TEM	Transmission Electron Microscope
WSN	Wireless Sensor Networks
XRD	X-Ray Diffraction

CHAPTER 1 INTRODUCTION

1.1 Motivation and research background

Many wireless and portable devices such as wireless sensor networks (WSN), intelligent monitoring systems, and mobile communication devices are powered by chemical reaction based batteries. Operational lifetime of the devices can be raised by adding more batteries, but the reduced efficiency of the battery due to self-discharge of the batteries is unavoidable [1]. Lifetime of the devices is limited by the battery, which should be recharged or replaced to extend the lifetime. Since WSN consists of a great number of nodes, it is inconvenient and costly to recharge or replace the battery [2]. In addition, the power consumption cannot be identical in every node because active time is different from node to node. In the case of rechargeable batteries, recharging process is time consuming because it takes several hours to charge AA size battery. In disposable batteries, waste disposal may cause environmental concerns. Dimensions of WSN and mobile devices decreases with the advance of technology for light-weight and low power consumption, but WSN needs 1 mW to 60 mW for operation depending on active mode [3]. The maximum capacity of AA sized commercial battery is three thousand mAh with 1.25 V, and thus it is possible to fabricate a millimeter-sized device due to bulky battery, so the battery based device is not compatible with miniaturization. Therefore, additional power supply based on a renewable energy source is required to support rechargeable batteries or to replace the batteries.

To determine a suitable renewable energy source, the mobile and independent power

sources need to be characterized in terms of electric and physical properties [4]. The electric properties include power density, voltage and current. The power density can be the crucial factor to determine feature size. The generated voltage from the renewable source may also influence circuit operation because of minimum voltage requirement. The physical properties encompass size, shape, and weight of a harvesting device.

The most popular renewable energy is solar energy, and the other energy sources could be mechanical energy and thermal energy [5]. The power density obtained from various energy sources are compared in table 1.1.

Table 1.1 Power density obtained from renewable power sources [4].

Source	Power density (mW/cm^3)
Solar energy	15
Mechanical energy	0.33
Thermal energy	0.04

Advantages and disadvantages of different renewable power sources for electronic devices are also summarized in table 1.2 [4]. Solar energy can produce the highest power density as shown in the table, but utilization of the optical energy is limited by weather conditions such as cloud, snow, and rain. Thermal energy may not be appropriate for mobile applications and WSN because the energy is immobile and available in specific areas. In contrast, mechanical energy appears to be the most pervasive energy sources in common surroundings. The power density obtained from mechanical energy is lower than that from solar energy, but the power supply harvested from mechanical energy can manage to operate WSN, as

shown in figure 1.1 [6]. In the figure 1.1, the electromagnetic and piezoelectric energy harvesting correspond to the power energy density obtainable from the mechanical energy sources. Various vibration sources in daily life, such as their frequency and acceleration values were also summarized [7, 8]. Typical frequency ranges from 60 Hz to 240 Hz, and its acceleration ranges between 0.1 m/s^2 (refrigerator) to 10 m/s^2 (machine tool). Therefore, vibration energy can be the most suitable energy source to supply electric energy to various independent electronic device such as WSN and mobile devices.

Table 1.2 Advantages and disadvantages of various energy sources as a power source for mobile, or independent electronic device [4].

Source	Advantage	Disadvantage
Solar enegy	High power density	Limited by weather condition Large surface area is required
Mechanical energy	Common energy source	Low power density
Thermal energy	High reliability, Long lifetime, Low maintenance cost	Low power density, Immobility

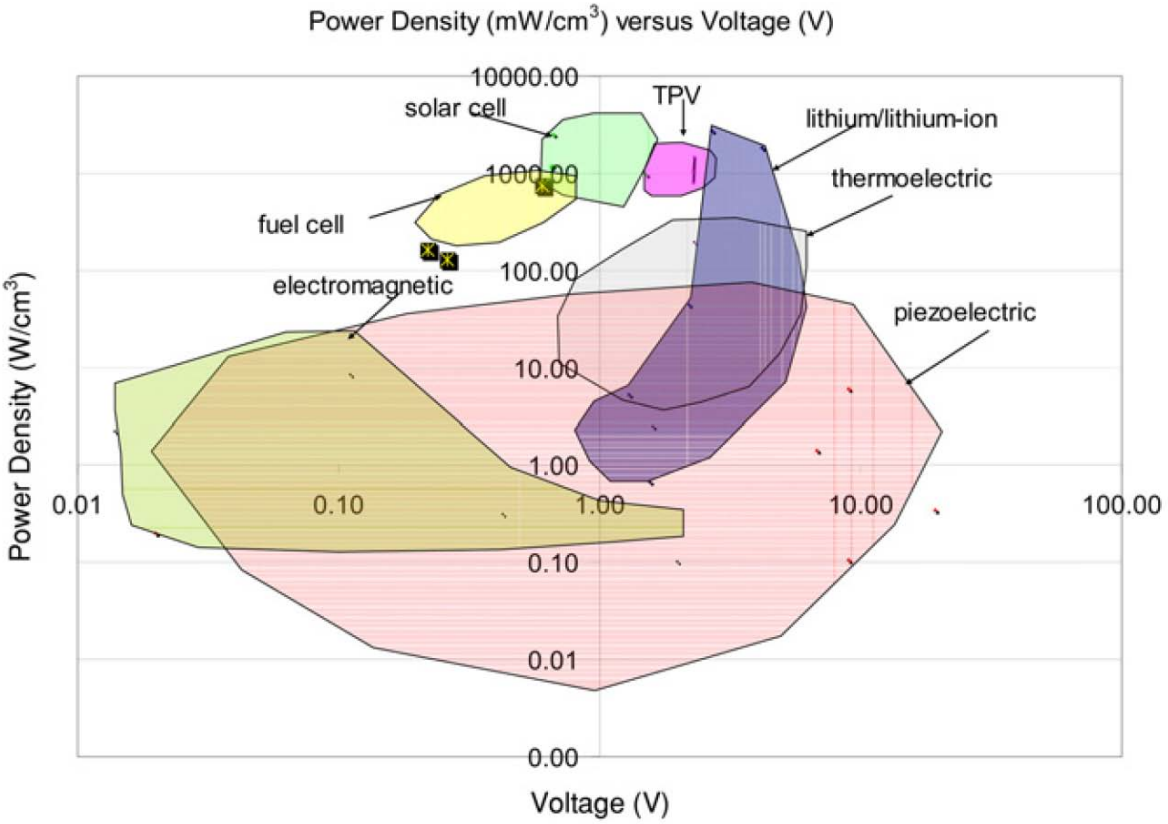

Figure 1.1 Power density range from the energy sources [6].

Table 1.3 Comparison of the mechanisms for vibration energy harvesting [4, 6, 9].

There are three mechanisms that can convert vibration energy into electricity; Electrostatic, electromagnetic, and piezoelectric energy harvesting. Three mechanisms are summarized by comparing their electric and physical properties, merits and demerits in table 1.3 [4, 6, 9]. In the table, output power density and voltages show maximum values from literatures.

Piezoelectricity is the most suitable mechanism to collect vibration energy for mobile and portable electronic devices because piezoelectric energy harvester can provide the highest power density, voltage, and their fabrication is also compatible with the microfabrication process.

In the table 1.3, piezoelectric energy harvesting could achieve 15 mW/cm^3 comparable the power density of solar cell, but there was aid of external circuit which extracts generated charge from the device. In other words, efficiency of a piezoelectric energy harvester should be improved for practical applications.

1.2 Research objectives

This research is to investigate three critical factors for the output power density of piezoelectric energy harvesters (PEHs) operating in our environment conditions. Investigated factors are the role of environment temperature on the performance of PEHs, the effects of piezoelectric mode on the power density of PEHs, and the harvesting of abroad frequency range of vibration sources in our environment. The most significant factor to influence the output power of PEHs during operation can be environmental temperature because materials used to construct energy harvesters strongly depend on temperature. The first task compares temperature effects on the output power of PEH. Since piezoelectric material PZT has different piezoelectricity according to the piezoelectric mode or orientation, the second task investigates the effects of piezoelectric mode on the performance of PEHs. The third study presents a unique concept of PEH that can harvest energy in a wide range of environment vibration frequencies. This investigation can advance fundamental understanding of PEHs and provide engineering solutions to improve the output power of PEHs.

1.2.1 Temperature effect on the performance of PEH

Heat is the most influential factor to function of piezoelectric materials. A piezoelectric material loses polarization at temperature above the Curie temperature. Bulk and microelectromechanical system (MEMS) scale PEHs were prepared to investigate effect of temperature on the output power of PEHs. Bulk scale devices were constructed with soft and hard PZT to compare sensitivity of the devices with different types of PZTs. The comparison between bulk and MEMS scale device shows size effect in the degradation of PEH upon temperature increase. Analysis of temperature dependent materials parameters in mathematical modeling manifests the most influential material parameters in the thermal degradation of the PEH.

1.2.2 Piezoelectric mode for maximum output power in PEH

PEHs are fabricated with two types of electrode configurations for d_{33} and d_{31} mode device in MEMS scale; rectangular shape of top and bottom electrode for d_{31} mode operation, interdigital electrode (IDE) for d_{33} mode operation. A mathematical equation is derived for d_{33} mode device because a correct model has not been reported for output power estimation of the d_{33} mode PEH. The mathematical equation is verified by fabricated devices, and estimates IDE design for maximum power density in PEH. The performance of d_{33} and d_{31} mode PEH is compared through experiment and modeling. In addition, differences in power generation characteristics are investigated in terms of voltage, current, and geometry of electrode through measured values from fabricated devices and computed values from modeling.

1.2.3 A PEH with wide working frequency range

A PEH is fabricated based on magnetic flexible substrate. Piezoelectric ZnO is deposited on the magnetic foil. Electric properties of ZnO for piezoelectric applications are obtained by Cu doping without heat treatment to preserve magnetic property of the amorphous phase substrate. The magnetic cantilever is actuated by a vibrating permanent magnet. Output power is measured in frequency range of 0-200 Hz to determine working frequency range.

1.3 Structure of dissertation

Chapter 1 outlines motivations, research objectives, and structure of this dissertation.

Chapter 2 explains background knowledge for this dissertation with fundamentals of piezoelectricity and piezoelectric materials, and literature survey on previous research.

Chapter 3 describes experimental procedure involved in fabrication and characterization process.

Chapter 4 covers theoretical modeling to estimate output power and behavior of PEHs.

Chapter 5 discusses result from the study about temperature effect on the performance of PEH. Soft and hard PZT based bulk scale PEHs are compared. MEMS PEH is compared with those two bulk scale PEHs to investigate size effect.

Chapter 6 verifies mathematical model for a d_{33} mode PEH with fabricated d_{33} mode devices having various sets of IDE. The output power of the d_{33} mode PEH is studied as a function of IDE configuration. Results from d_{33} mode devices are compared and discussed with those from d_{31} mode devices.

Chapter 7 demonstrates a PEH with wideband working frequency.

Chapter 8 concludes this research and proposes future work to improve quality of the research.

CHAPTER 2 LITERATURE BACKGROUND

2.1 Fundamentals of piezoelectricity

Piezoelectricity is dimensional change (strain) by electric field application, which is direct piezoelectric effect. The development of electric field by strain is reverse piezoelectric effect [10]. Origin of the piezoelectricity is asymmetry in crystallography. There are 32 point groups in crystallographic system. 21 point groups are noncentosymmetric out of 32 groups. 20 groups exhibit piezoelectricity among 21 point groups [11].

2.1.1 Parameters in piezoelectricity

In piezoelectricity, stimulation and response are electric displacement D, electric field E, stress σ, and strain δ. The terms are related by 4 piezoelectric constant; d_{ij}, g_{ij}, e_{ij}, and h_{ij} as shown in equation (2.1), (2.2), (2.3), and (2.4) assuming identical temperature condition. d_{ij} relates electric displacement and stress. g_{ij} relates electric field and stress. e_{ij} relates electric displacement and strain. h_{ij} relates electric field and strain. d_{ij} and g_{ij} are generally called piezoelectric strain (charge) constant and piezoelectric voltage constant, and the two constants are related by dielectric constant ε, as shown in equation (2.5). Metric unit of d_{ij} and g_{ij} are pm/V (pC/N) and mV/N. The subscripts of the constants ij represent direction of stimulation and response as shown in figure (2.1). 1, 2, and 3 denote three axis directions. 4, 5, and 6 are planes. The first in the subscript represents polarization direction and the second denotes stress direction. For example, d_{31} piezoelectric mode means polarization in direction 3 and strain in 1 direction in figure (2.1). The piezoelectric constant is second order tensor so, 36 combinations are available. However, only 3 piezoelectric modes are available due to rotation of unit cell; d_{31}, d_{33},

and d_{15} mode. There is only one shear mode, d_{15}, because shear plane should be normal to the polarization axis.

$$d_{ij} = \left(\frac{\partial D_i}{\partial \sigma_j} \right)_E \tag{1.1}$$

$$g_{ij} = -\left(\frac{\partial E_i}{\partial \sigma_j} \right)_D \tag{1.2}$$

$$e_{ij} = \left(\frac{\partial D_i}{\partial \delta_j} \right)_E \tag{1.3}$$

$$h_{ij} = -\left(\frac{\partial E_i}{\partial \sigma_j} \right)_D \tag{1.4}$$

$$g_{ij} = \frac{d_{ij}}{\varepsilon_{ii}} \tag{1.5}$$

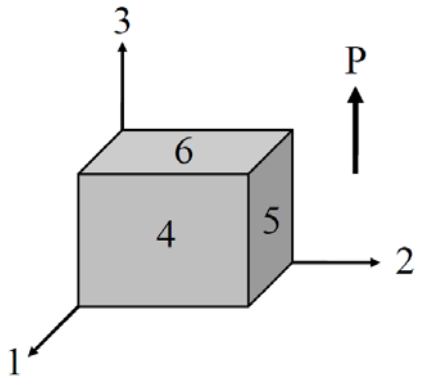

Figure 2.1 Direction and plane labeling for piezoelectricity.

Equations from (2.6) to (2.9) show relation between D, E, σ, and δ, where s is elastic compliance and the superscript stands for the constant is invariable. Electromechanical coupling

coefficient k represents transformation efficiency between mechanical energy and electrical energy, which is defined by equation (2.10), where E_1, E_2, and E_{12} are electric energy, mechanical energy, and piezoelectric energy density.

$$D = d\sigma + \varepsilon^{\sigma} E \tag{1.6}$$

$$E = -g\sigma + D / \varepsilon^{\sigma} \tag{1.7}$$

$$\delta = s^{E}\sigma + dE \tag{1.8}$$

$$\delta = s^{D}\sigma + gD \tag{1.9}$$

$$k^2 = \frac{E_{12}^2}{E_1 E_2} = \frac{d^2}{s^E \varepsilon^{\sigma}} \tag{1.10}$$

2.2 Piezoelectric materials

Physical and electrical properties of popular piezoelectric materials are summarized in table 2.1 [10, 12-17]. Details of PZT, $Pb(Mg_{1/3}Nb_{2/3})O_3$-$PbTiO_3$ (PMN-PT), $Pb(Zn_{1/3}Nb_{2/3})O_3$-$PbTiO_3$ (PZN-PT), ZnO, and AlN are reviewed in this section.

2.2.1 Lead zirconate titanate (PZT)

$Pb(Zr_xTi_{1-x})O_3$ (PZT) is one of the most popular piezoelectric materials due to superior piezoelectric constant d, high dielectric constant, and electromechanical coupling coefficient. The PZT is a perovskite structure as shown in figure 2.2. Displacement of Ti^{4+} or Zr^{4+} ions located from the center of octahedron is origin of polarization. The PZT is solid solution of $PbTiO_3$ and $PbZrO_3$. Structure of PZT changes from rhombohedral to tetragonal with increase of $PbTiO_3$ as described in figure 2.3 [18]. Excellent piezoelectric property of PZT appears in the vicinity of morphotropic phase boundary (MPB). There are 14 distortion states at MPB, which is

explained by coexistence of rhombohedral and tetragonal phase. Rhombohedral and tetragonal structure can have 8 and 6 polarization directions, respectively [19].

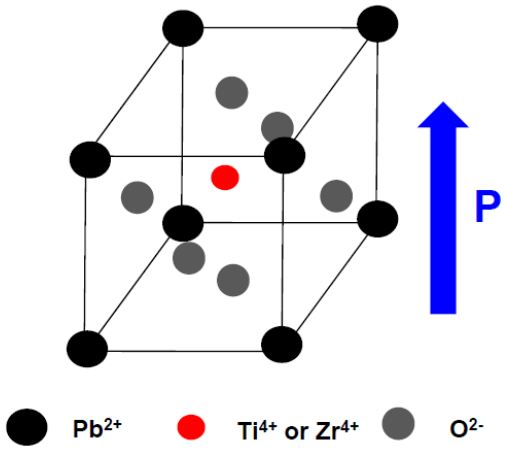

Figure 2.2 Perovskite structure of PZT.

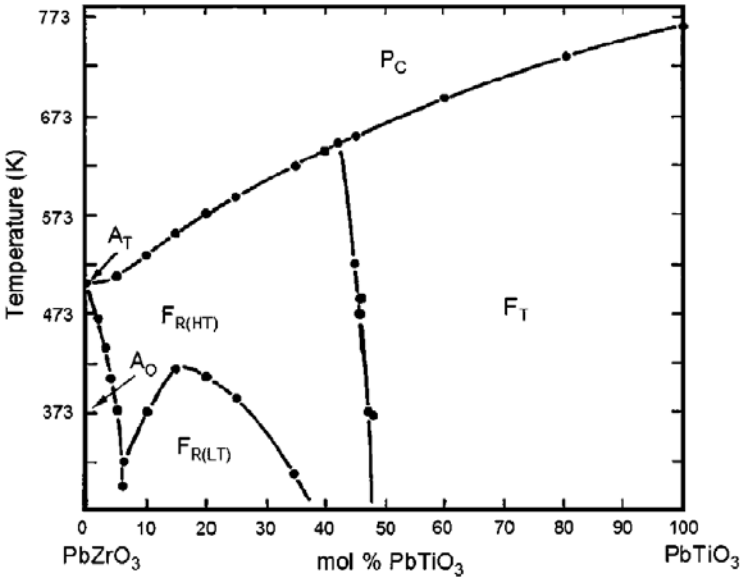

Figure 2.3 Phase diagram of PZT (Solid solution of $PbTiO_3$ and $PbZrO_3$) [18].

Table 2.1 Physical and electrical properties of piezoelectric materials [10, 12-17].

Property	s_{11} ($\mu m^2/N$)	s_{33} ($\mu m^2/N$)	d_{31} (pC/N)	d_{33} (pC/N)	d_{15} (pC/N)	ε_r	density (kg/m^3)	k_{31}	k_{33}
Quartz	12.8	9.6	2.3			4.6	2650	0.1	
$BaTiO_3$	8.6	9.1	-79	190	270	1600~1900	5700	0.21	0.49
PZT -bulk	12.2	14.6	-119~ -234	268~ 480	335	1200~ 2800	7700~ 7900	0.33~ 0.39	0.68~ 0.79
PZT -film	14.2	18.7	-30~ -70	190~ 250	440	1300~ 1500	7500	0.17	0.54
$PbNb_2O_6$	29	25	-11	80		225~ 560	5900	0.07	0.045
$(Na_{1/2}K_{1/2})NbO_3$	9.6	10	-50	160		400~ 600	4500	0.27	0.53
$LiNbO_3$	5.8	5	-0.82	6	69	29~ 85	4640	0.02	0.17
$PbTiO_3$	11	11	-7.4	47		203~ 494	7120	0.052	0.35
PMN-PT	47.6	125	-1154~ -1330	1500~ 2820		835~ 1110	7600~ 8060	0.73	0.94
PZN-PT	66.7	142.9	-1154	2000		3100~ 5200	8310	0.66	0.78
ZnO	11	8	-5.4	11.7	-11.3	7.57~ 9.03	5665	0.12~ 0.2	0.26~ 0.41
AlN	3	3	-2~ -2.8	4~ 5.8		9	3300	0.13~ 0.18	0.27~ 0.39

Striking origin is controversial in high piezoelectric property of PZT. Noheda and coworkers [20] investigated PZT near the MPB, and found presence of monoclinic phase in at MPB. The monoclinic phase was resulted from rotation of polar axis, which was argued as a origin of high piezoelectricity [21]. The monoclinic phase was observed as a function of temperature using transmission electron microscope (TEM), and found triclinic phase from heated PZT. The triclinic phase transformed to monoclinic phase upon cooling, and was argued as an origin of superior piezoelectricity due to lower symmetry by polarization.

2.2.2 Soft and hard PZT

Electric properties of PZT can be controlled by doping element for practical applications while there is little change in physical properties as summarized in table 2.2. Properties of PZT are changed to soft and hard type by higher and lower valence state ions doping, respectively. Oxygen vacancies are incorporated by doping of lower valence state ions, and cation vacancies are formed by substitution of higher valence state ions. Oxygen ions are bigger than cations and closely located so that oxygen vacancies are highly mobile. In contrast, cation and cation vacancies movement are relatively constraint due to high energy barrier formed by oxygen ion network. Mobility of impurities was studied with K^{+1} and La^{3+} doped PZT. It was found from the work that lower valence state ions are more mobile than higher valence state impurities, and the former suppresses dielectric permittivity [22]. Lower valence state ion doping generates acceptor-oxygen vacancy pairs which is thermally unstable and easily reoriented by thermal energy. The rotation stabilizes the polarization domain, thus permittivity is decreased and coercive electric field is increased, which is characteristics of the hard PZT. Higher valence state ion doping reduces oxygen vacancies, so does domain-stabilizing energy. Less stable domain is

easily reoriented by external field, so it is called a soft PZT. The effect of domain stabilizing effect is clearly indicated in terms of material parameters in table 2.2. The soft PZT possesses high dielectric, piezoelectric constant, electromechanical coupling coefficient and lower Curie temperature. High temperature sensitivity, i.e. rapid increase of dielectric and piezoelectric constant, can be expected in the soft PZT from high domain mobility and lower Curie temperature. A soft PZT employed piezoelectric actuator may be operated by lower electric field than an actuator using hard one, but the operation temperature range of the device is narrower than the device made of hard PZT.

Table 2.2 Physical and electrical properties of soft and hard PZT [23].

	Soft PZT	Hard PZT
Doping element	Nb^{5+}, Ta^{5+}, Sb^{5+}	Co^{3+}, Fe^{3+}, Sc^{3+}, Ga^{3+}, Cr^{3+}, Mn^{3+}, Mn^{2+}
ε_r	3800	1800
d_{31}	-320	-190
d_{33}	650	320
k_{31}	0.44	0.32
k_{33}	0.75	0.72
Young's modulus (Gpa)	50	52
Q factor	30	80
T_c	230	350

Domain mobility of soft, hard and normal PZT was compared. Three types of ceramic PZTs were fabricated and textured by compression, and the texture was released by annealing. Out of three types of PZTs, the soft PZT released the largest amount of stress because of highly mobile domains while the greater lattice distortion was remained in hard and normal PZT owing to restrained domain mobility [24]. Since soft and hard PZT have different domain mobility, the piezoelectric constant of the two PZTs will be affected by temperature. There are two types of contributions to the piezoelectric effect; intrinsic and extrinsic contribution. The intrinsic piezoelectric effect is originated from lattice distortion and the extrinsic one is donated by piezoelectric domain wall motion. Details of the intrinsic and extrinsic contribution to piezoelectricity are elaborated in 2.3.

2.2.3 PMN-PT and PZN-PT

$Pb(Mg_{1/3}Nb_{2/3})O_3$ (PMN) and $Pb(Zn_{1/3}Nb_{2/3})O_3$ (PZN) are relaxor ferroelectrics. The two materials form solid solution with $PbTiO_3$ (PT). PMN-PT and PZN-PT are attractive piezoelectric materials due to high piezoelectric constant *d*, high electromechanical coupling constant, and high strain level. Ternary phase diagram of $PbZrO_3$, $Pb(B_1,B_2)O_3$ (B_1=Mg^{2+}, Zn^{2+}, Ni^{2+}, Sc^{3+}, B_2=Nb^{5+}, Ta^{5+}, W^{6+}), and $PbTiO_3$ is schematically shown in figure 2.4 [25]. PMN-PT and PZN-PT exhibit the highest piezoelectric constant around MPB as PZT does. Single crystal PZT-PT shows highly anisotropic piezoelectric property due to instability of piezoelectric domain in <111> orientation. The unstable domain is origin of hysteric property because the domain is subject to depoling and reorientation. Rhombohedral crystal with <100> orientation, however, is stable that can induce the maximum strain upon electric field application. According to Muralt and Tadifadapa [17, 26], the ferroelectric relaxors are not superior to the PZT for

piezoelectric MEMS in the light of integration issue, hardness and lower Curie temperature. The growth temperature of relaxor-PT is much higher than that of PZT. The hardness of relaxor-PT is soft and could not transform applied mechanical energy to electric energy. The PMN-PT and PZT-PT have been investigated due to high piezoelectric constant in spite of those disadvantages. Recently, epitaxial PMN-PT was fabricated on Si wafer and demonstrated vibration energy harvesting with cantilever structure [27].

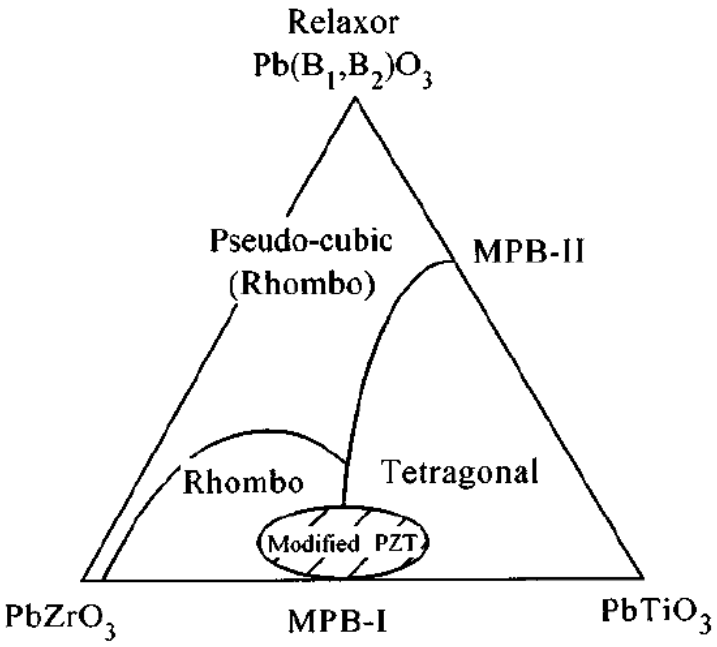

Figure 2.4 Ternary phase diagram of PZT and relaxor-PT showing MPB [25].

2.2.4 ZnO and AlN

ZnO and AlN possess wurtzite structure and are non-ferroelectric and piezoelectric materials. The non-ferroelectric materials should be fabricated with texture to exhibit piezoelectric property because the polar axis cannot be oriented with electric field. The two materials have much lower piezoelectric constant than PZT and relaxor-PT. However, ZnO and

AlN have been used for bulk acoustic wave (BAW) device and resonators because resonators and BAW devices are operated at high frequency range (~ GHz), and signal loss is lower in ZnO and AlN than in PZT in the frequency range.

2.3 Intrinsic and extrinsic contribution to piezoelectric property

Piezoelectric property is resulted from lattice distortion and ferroelectric domain wall motion. In this section, the origin of piezoelectricity and dependency of piezoelectricity to material parameters such as size, composition and crystallographic orientation are reviewed through the most popular piezoelectric material PZT.

2.3.1 Ferroelectric domain and domain wall

A ferroelectric material possesses paraelectric phase with symmetric structure at temperature above Curie temperature. The symmetric structure undergoes distortion during phase transformation from paraelectric to ferroelectric phase while temperature decreases to below Curie temperature. In $PbTiO_3$, the phase transformation occurs between cubic and tetragonal structure, and spontaneous polarization occurs in c-axis direction. A ferroelectric domain forms with unit cells having identical polarization direction. It is unfavorable to be polarized in single direction, so the ferroelectric domain will be oriented into random direction to reduce electrostatic and elastic energy. Domain wall is developed between domains with different orientations as a result of domain split. There are two types of domain walls as shown in figure 2.5; 180° domain wall (figure 2.5 (a)) and non-180° domain wall (figure 2.5 (b)). $PbTiO_3$ transforms to tetragonal phase with 90° domain wall upon cooling from Curie temperature to reduce elastic energy if stress is applied on the top of the material as shown in

figure 2.6. 180˚ domain walls would be dominant without stress as result of electrostatic energy [28]. Motion of the 180˚ domain wall does not accompany strain because flip of the domain can occur without shape deformation. On the contrary, movement of the non-180˚ domain wall involves strain change. Hence, the 180˚ domain wall formation reduces only electrostatic energy, while both electrostatic and elastic energy are decreased by the non-180˚ domain wall formation, i.e. the 180˚ wall motion is related to only dielectric property, and the non-180˚ domain wall motion is to both dielectric and piezoelectric property. There are two types of contributions from ferroelectric domain to piezoelectric property; intrinsic and extrinsic contribution. Behavior of each ferroelectric domain and motion of domain wall contribute piezoelectricity intrinsically and extrinsically, respectively.

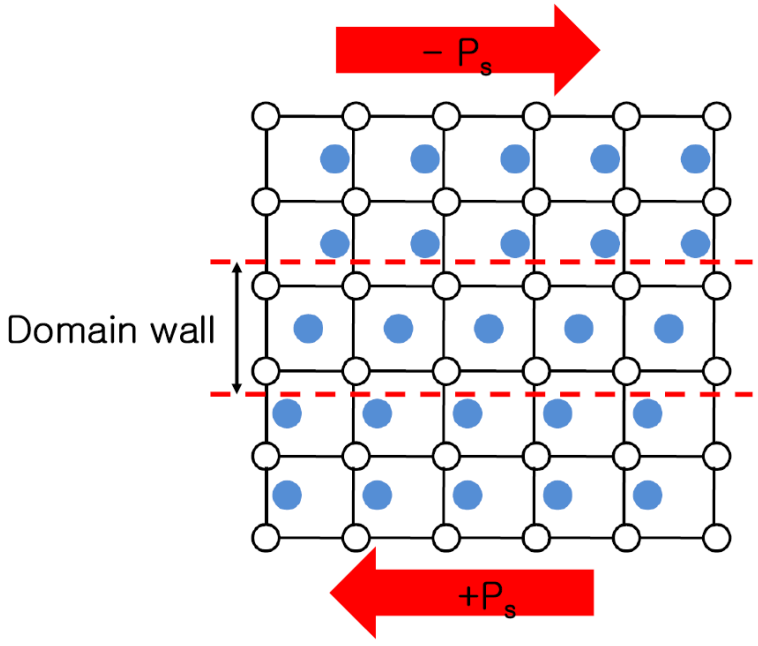

Figure 2.5 (a)

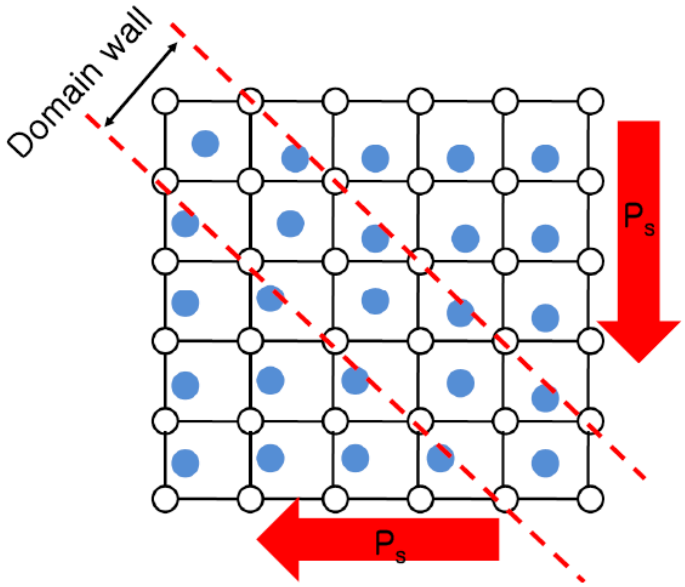

Figure 2.5 (b)

Figure 2.5 Ferroelectric domain and domain wall (a) 180° domain (b) 90° domain (non-180° domain)[28].

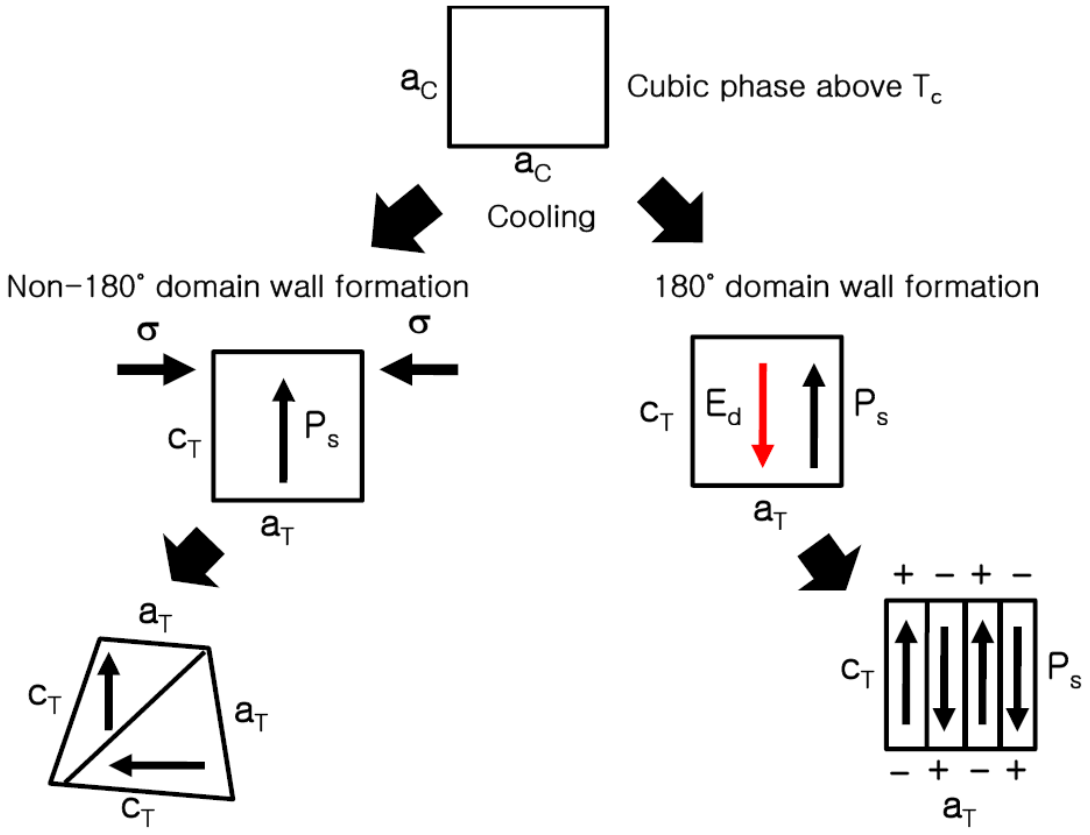

Figure 2.6 Formation of non-180˚ domain wall with stress (σ) (left), and 180˚ domain wall without stress (right) [28].

2.3.2 Studies on the intrinsic and extrinsic piezoelectric contribution

L. Wu et al. [29] studied effect of A-site and O-site vacancies on the quality factor using rare earth element doped PZT. Large electromechanical coupling coefficient was observed with A-site vacancies because mobility of non-180˚ domain walls was promoted with reduced local stress while O-site vacancies hinder movement of domain wall as grain boundary constrain domain motion.

Zhang et al. [30] investigated material constant such as dielectric, piezoelectric constant

as a function of temperature to see and separate intrinsic and extrinsic contribution to the piezoelectric property. Temperature ranged between 0 and 300 K, and they could freeze effect of the doping, i.e. extrinsic contribution in PZT, which was verified by identical dielectric constant from the PZTs with different doping concentration. It was discussed in the report that non-180° domain wall is ferroelastic and responsible for dielectric and piezoelectric property. Steep domain wall energy could be inferred from narrow domain in 180° domain, thus higher energy is required for activation of the 180° domain wall.

Domain wall energy was calculated to show relation between domain wall clamping and orientation of defects [31]. Acceptor doped ferroelectric materials age with reorientation of defects to uniform direction. The alignment of defects reduces extrinsic piezoelectric contribution from domain wall motion due to stabilized domain energy and reduced domain wall motion.

Taylor and Damjanovic [32] reported piezoelectric properties of PZT films with different orientations. PZT thin films were grown with (111), (100), and random orientation. Piezoelectric constant d_{33} was calculated and measured with the orientations as given in figure 2.7. (100) oriented PZT exhibited the highest value and the biggest difference in calculation and experiment. They discussed the causes for the differences; different clamping effect, calculation error, and strong contribution of domain wall motion in (111) oriented film, compensating decrease of piezoelectric constant by substrate clamping. They focused on the third reason that was indirectly verified by the fact dielectric constant in (111) oriented film is comparable to that of (100) oriented film although (111) oriented film possesses 2/3 of dielectric constant of (100) oriented film in calculation. In order to support strong domain wall motion in (111) orientation, they measured piezoelectric constant d_{33} as a function of electric field as given in figure 2.8. The

(100) oriented PZT film showed stronger nonlinearity than (111) oriented PZT film, which indicates weaker extrinsic contribution to piezoelectric property in the former. Orientations of polarization direction could explain the difference in nonlinearity as shown in figure 2.9. Polarization type 1 contributes to piezoelectric constant d_{33} in (111) oriented film, but piezoelectric constant d_{33} of (100) oriented PZT film is not contributed by the domain in figure 2.9.

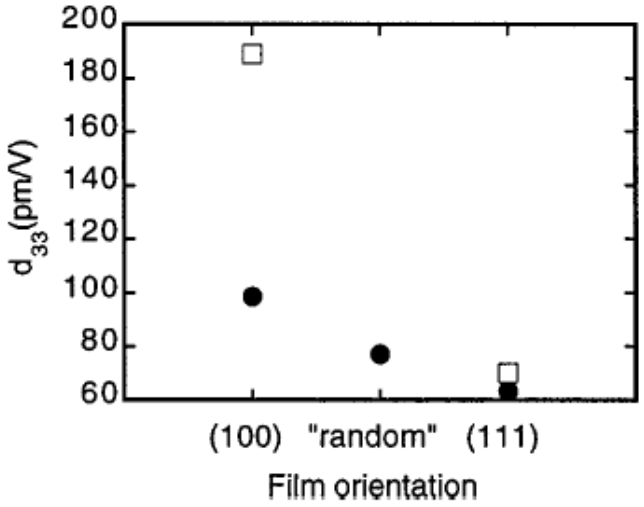

Figure 2.7 Piezoelectric constant d_{33} from PZT thin films with different orientations. Squares and black circles denote calculated and measured values, respectively [32].

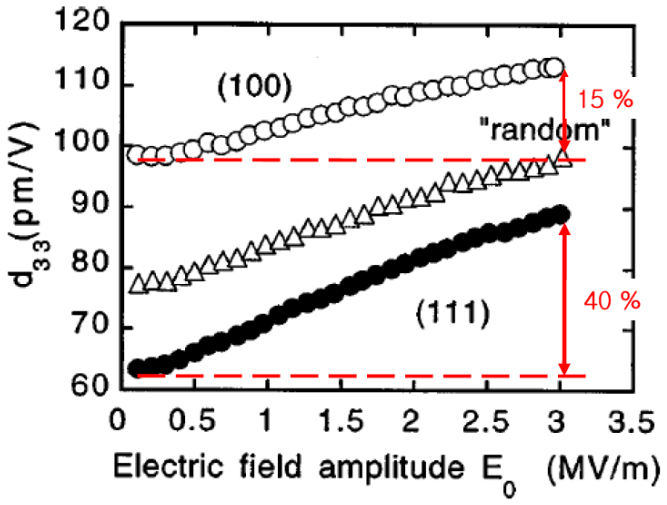

Figure 2.8 Piezoelectric constant d_{33} as a function of electric field [32].

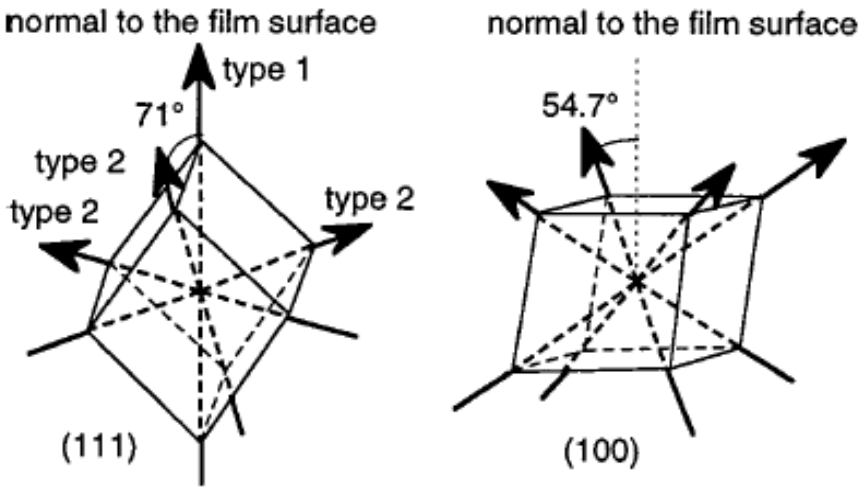

Figure 2.9 Possible polarization directions in (111) and (100) oriented PZT [32].

Xu et al.[33] studied dielectric and piezoelectric property of PZT in terms of domain and domain wall motion. They investigated properties of PZT as a function of orientation, size, temperature, electric field, and stress to isolate contribution from domain and domain wall motion. PZT films were grown with various thicknesses using different chelating agent. Degree of randomness was promoted in film orientation with increasing film thickness due to reduced

effect of sub-layer of the films. Freezing of domain wall motion was clearly shown by similar value of dielectric constant from the PZT films as temperature approaches to 0 K (figure 2.10). In addition, nonlinearity of the extrinsic contribution was shown by dielectric constant as a function of electric field at room temperature and 4.2 K. Size dependent extrinsic and intrinsic contribution were examined, and they manifested that non-180° domain wall motion (extrinsic contribution for piezoelectric property) is clamped by substrate in thin film while the clamping effect is relatively low in 180° domain motion responsible for dielectric constant (figure 2.12).

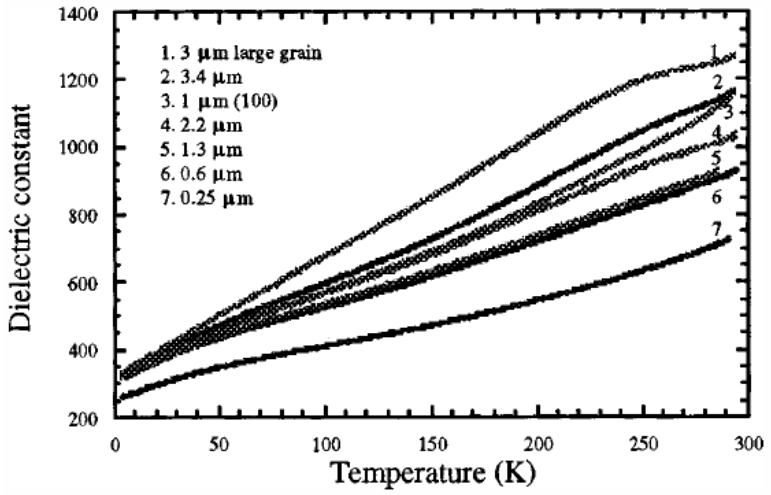

Figure 2.10 Temperature dependent dielectric constant of PZT films with various thickness [33].

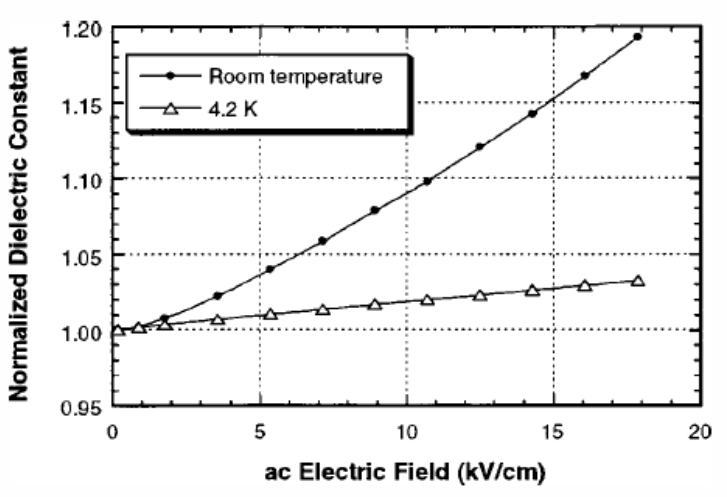

Figure 2.11 Dielectric constant as a function of electric field at room temperature and 4.2 K [33].

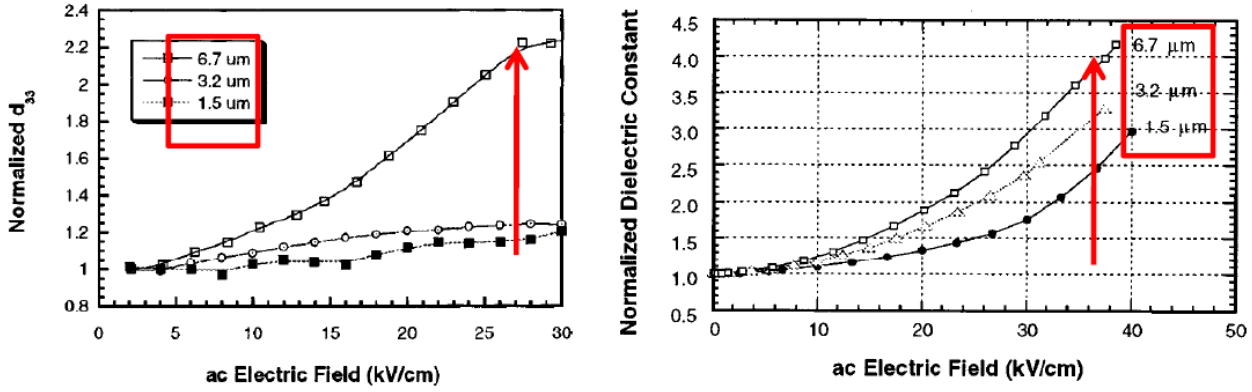

Figure 2.12 Normalized piezoelectric and dielectric constant as a function fo electric field from PZT films with various thickness [33].

Kim et al. [34] reported intrinsic and extrinsic contribution as a function of composition in PZT thin films. They also showed identical dielectric constant at temperature near 0 K regardless of composition as shown in figure 2.13 (a). Therefore, they could separate intrinsic and extrinsic contribution to dielectric constant as described in figure 2.13 (b).

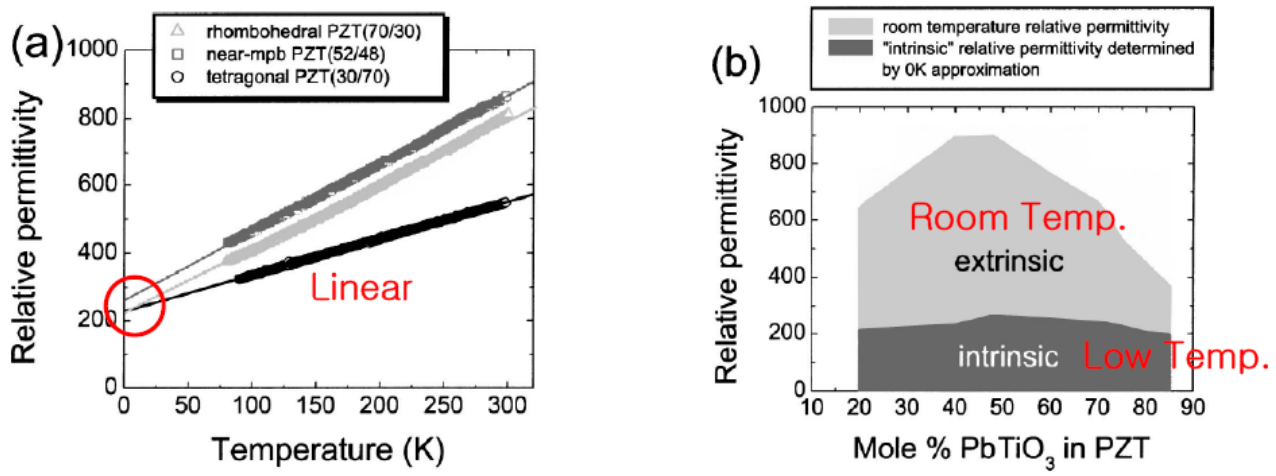

Figure 2.13 Dielectric constant as a function of (a) temperature (b) composition from PZT films [34].

2.4 Temperature dependent piezoelectric property

Piezoelectric property disappears in a piezoelectric material when temperature exceeds Curie temperature because polarization is not stable due to thermal perturbation. Performance of PEHs were compared with PZT, PVDF, and macro fiber composite (MFC) [35]. The power variation upon temperature change would be different depending on materials' constant variation although output power is the highest in PZT based PEH.

Bedekar et al. [35] compared mechanical energy harvesters based on $YCa_4O(BO_3)_3$, $LiNbO_3$, $La_3Ga_5SiO_{14}$, and soft PZT. Soft PZT produced three order higher output power at room temperature, but $YCa_4O(BO_3)_3$ and $La_3Ga_5SiO_{14}$ based devices were the most stable [36]. Sabatea al. [37] measured, compared, and discussed variation of piezoelectric, dielectric, and elastic constant of soft and hard PZT as a function temperature. Soft PZT exhibited larger change than hard PZT in the material's properties due to strong extrinsic contribution by domain wall motion. Schultz et al. [38] tested output voltage of a PEH at elevated temperature range.

The authors considered role of adhesion layer between cantilever and piezoelectric material. However, the analysis was not performed based on different types of piezoelectric sheet. Miclea et al. [39] investigated temperature dependent electromechanical coupling coefficient, dielectric constant, and loss tangent. The authors concluded there is almost no degradation in piezoelectric property of the soft PZT up to 150 ˚C, which is contrary to that of Sabat's report. Miclea's research may be based on incorrect measurement because domain motion of soft PZT is sensitive to temperature. Wolf and Strolier-Mckinstry [40] calculated change of piezoelectric constant as given in figure 2.14.

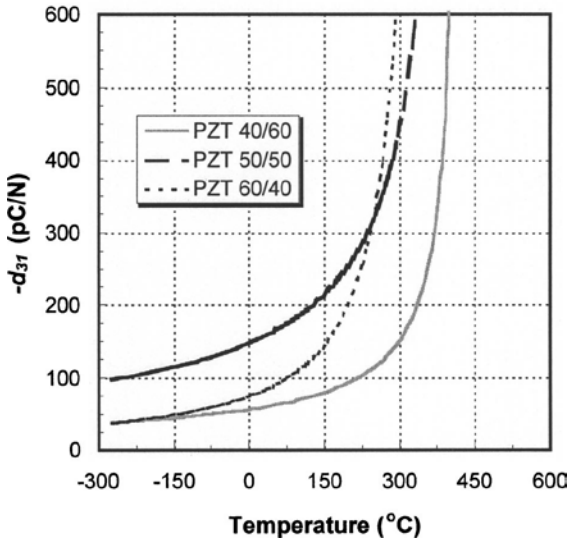

Figure 2.14 Piezoelectric constant d_{31} of PZT as a function of temperature [40].

2.5 PEH based on d_{31} and d_{33} mode

Three piezoelectric modes are available in a piezoelectric material; d_{31}, d_{33}, and d_{15} mode. It is difficult to realize a shear mode based PEH, so this section compares and introduces d_{31} and d_{33} mode based PEHs.

2.5.1 Comparison between d_{31} mode and d_{33} mode PEH

Figure 2.15 describes relation between stress and accompanied polarization direction in d_{31} and d_{33} mode. Electric field is in perpendicular and parallel orientation to stress direction in d_{31} and d_{33} mode, respectively. Figure 2.16 illustrates cross section of bimorph. Since the cantilever vibrates in vertical direction, strain is in in-plane direction. Neutral layer where strain is zero is located center of structural layer when thickness of the piezoelectric layers is identical on the top and bottom. Tensile and compressive stress is applied on the top and bottom piezoelectric layer, respectively, when the cantilever is bent downwards. A d_{31} mode device is constructed with rectangular shape of electrodes on top and bottom electrode (TBE) as shown in 2.17 (a). The bottom electrode serves as a not only conductive layer, but also seed layer for piezoelectric materials growth, which promotes structural and electrical quality of the piezoelectric layer. Direction of strain and generated electric field are different, and electrodes can be easily defined. In addition, piezoelectric constant d_{31} interrelates strain and electric field in a device as the value is derived in figure 2.15 (a). On the contrary, in a d_{33} mode PEH, electrode is not normal to stress as illustrated in figure 2.15 (b) due to ineffectiveness and difficulty in fabrication process. Therefore, most of d_{33} mode PEH is constructed with IDE to overcome the engineering issues as described in figure 2.17 (b). Bent electric field is generated between finger electrodes within piezoelectric layer. The generated electric field is not parallel with strain, and calculation of electric field is not simple because path for electric field cannot be defined as electrode spacing due to bent electric field. The degree of bending in electric field varies as a function of finger electrode width and spacing. Thus, piezoelectric constant d_{33} may not correctly relate strain and generated voltage in a d_{33} mode PEH, which is huge error source in the d_{33} mode device modeling. Therefore, there is much more reports on d_{31} mode PEHs than

d_{33} PEHs.

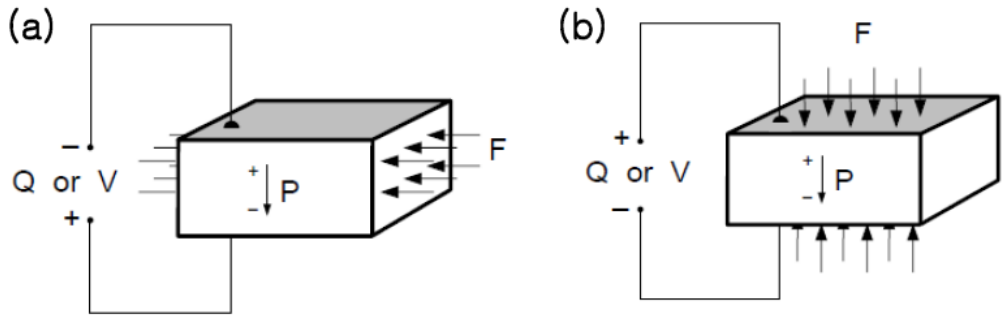

Figure 2.15 Relation between stress and polarization direction (a) d_{31} mode (b) d_{33} mode.

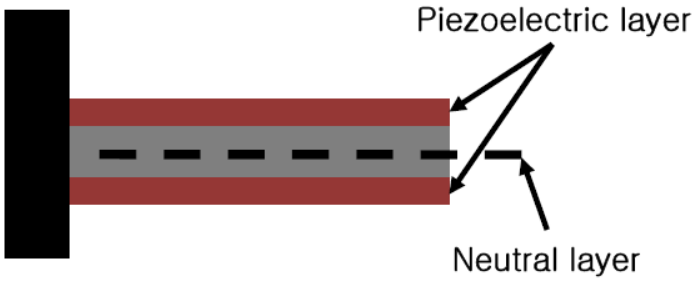

Figure 2.16 Cross section of bimorph. Brown and gray color denote piezoelectric and structural layer.

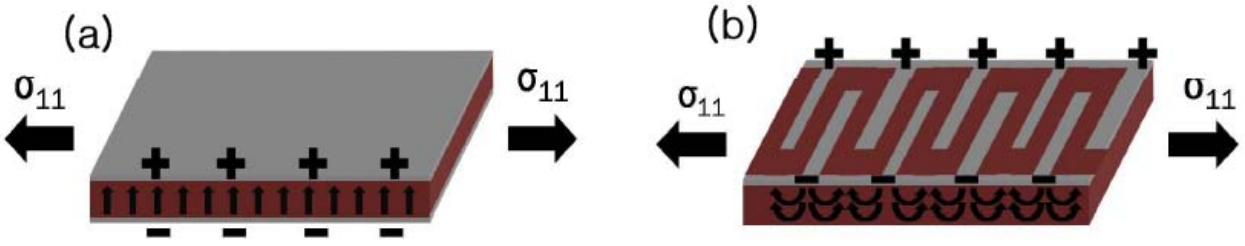

Figure 2.17 Relation between stress and generated electric field in PEHs. (a) d_{31} mode device (b) d_{33} mode device.

2.5.2 Studies for d_{31} mode based PEHs

Power density is of prime interest in PEH research. Various types of approaches were pursued to collect more electric energy from mechanical energy sources.

Jeong et al. [41] investigated PEH with multi-layers for high output power, but the approach is not appropriate to improve power density although power value was increased. Kim et al. [42] applied pre-stress using “Cymbal” structure and higher power was generated that a PEH without pre-stress. Roundy et al. [43] proposed and analyzed trapezoidal cantilever for uniform strain from fixed end to free end. The trapezoidal structure could produce higher power density than the cantilever with uniform width.

Piezoelectric property improvement is a way to promote power density in a PEH. Isarakorn et al. [44] succeeded in fabrication of a PEH with epitaxial PZT thin film. The authors deposited $SrTiO_3$and $SrRuO_3$ as seed layers of piezoelectric layer to grow epitaxial PZT on Si substrate. Power density was improved to 85 $mW/(g^2 \cdot cm^3)$ while 10 $mW/(g^2 \cdot cm^3)$ is power density of polycrystalline PZT based PEH. Morimoto et al. [45] fabricated PEHs with epitaxial piezoelectric thin film, but power density was lower than that of Isarakorn et al.’s device. It is because the authors transferred piezoelectric layer to polymer coated metal foil so that the portion of non-piezoelectric layer is too large compared to piezoelectric layer. Recently epitaxial PMN-PT thin film was grown on Si substrate with buffer layer. The device was demonstrated as an actuator, but the device could perform high output as PEH due to high piezoelectric coefficient [27].

Single crystal piezoelectric material may construct a PEH, but the size and application are limited due to the fabrication of single crystal [46, 47].

2.5.3 Studies for d_{33} mode based PEHs

A d_{33} mode PEH has not been widely studied as much as a d_{31} mode PEH. Choi et al. [48] optimized output power of a d_{33} mode PEH, but the research was oriented for structure optimization such as dimension of cantilever and size of proof mass, which were not related with piezoelectric mode.

The biggest difficulty in the d_{33} mode device research is output power estimation because the piezoelectric constant d_{33} does not correlate strain and electric field generation. Bowen et al. [49] simulated electric field in an actuator with IDE as shown in figure 2.18. The modeling showed piezoelectric layer underneath finger electrode does not participate in device operation as estimated from dipole direction not oriented to other finger electrode. Therefore, the piezoelectric layer not contributing device operation is called dead layer. Beckert and Krecher [50] considered an actuator with IDE on the top and bottom piezoelectric layer. They simulated electric field application between finger electrodes and defined piezoelectric layer underneath finger electrodes as an inactive layer.

Park et al. [51] computed output power of a d_{33} mode PEH using equivalent circuit model. However, the report did not reflect change of electric field bending depending on finger electrode width and electrode spacing. Electric field would be variable depending on electrode spacing because actual finger spacing is not equal to physical distance between finger electrodes. The authors estimated output power as a function of electrode gap and resistive load, but the calculation did not consider capacitance change with electrode configuration variation.

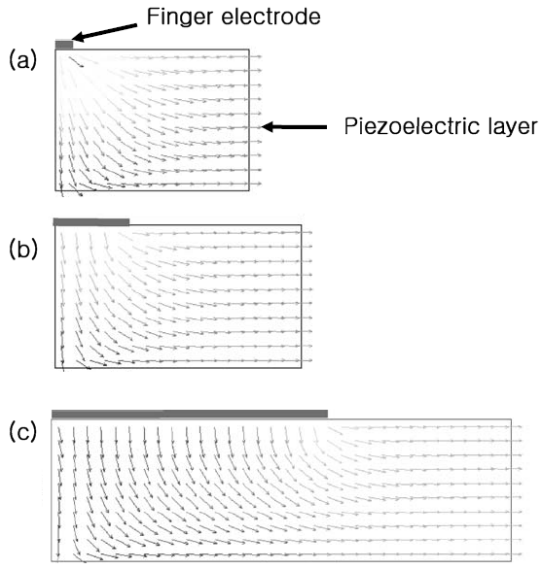

Figure 2.18 Electric field distribution in an actuator with IDE. Electrode width increases from (a) to (c) [49].

2.6 Studies on working frequency range of PEHs

In this section, studies on working frequency range of PEHs are introduced. One of the most serious disadvantage is narrow working frequency range in a mechanical resonance based PEH because sufficient vibration amplitude is available only around at resonance frequency. Various methods have been applied for broad working frequency range in the PEH as summarized in table 2.3; passive structure modulation, multi degree of freedom and stiffness modulation of beam.

Table 2.3 Studies for wideband PEH.

Author	Working frequency range	Method
Jo et al. [52]	10-40 Hz	Movable cantilever
Liu et al. [53]	30-48 Hz	Stoppers at the free end of cantilever
Gu et al. [54]	10-20 Hz	Stoppers at the free end of cantilever
Xu et al. [55]	20-100 Hz	Additional cantilever normal to PEH for two degree of freedom
Kim et al. [56]	9-14 Hz	Rotating proof mass between cantilevers
Challa et al. [57]	32-32 Hz	Cantilever stiffness modulation by magnetic force
Stanton et al. [59]	14-24 Hz	Nonlinear potential energy of cantilever by using magnetic force
Erturk et al. [60]	0-8 Hz	Nonlinear potential energy of cantilever by using magnetic force
Hajati and Kim [61]	1-2.75 kHz	Nonlinear stiffness in bridge structure
Dai et al. [62]	140-180 Hz	Nonlinear stiffness of cantilever by nonlinear springs

Jo et al. [52] demonstrated movable cantilever so that the length of cantilever can be adjusted automatically for resonance mode vibration as given in figure 2.19. The cantilever was displaced by horizontal force exerted from proof mass at large deflection. Liu et al. and Gu [53, 54] placed stoppers on the top and bottom of cantilever to modulate damping and stiffness of

cantilever. Working frequency range was extended although output power at resonance frequency was reduced. The authors proposed additional energy harvesting from stoppers made of piezoelectric materials.

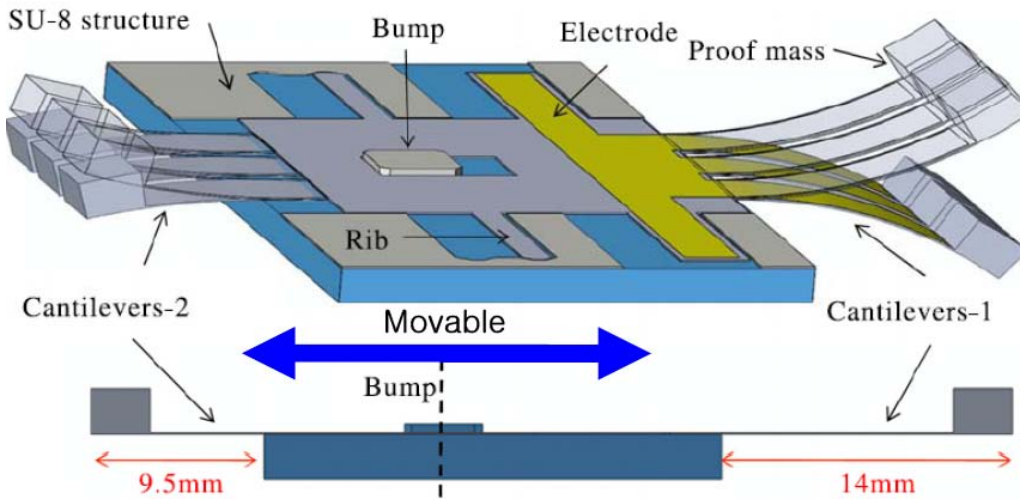

Figure 2.19 Movable cantilever for automatic resonance frequency matching [52].

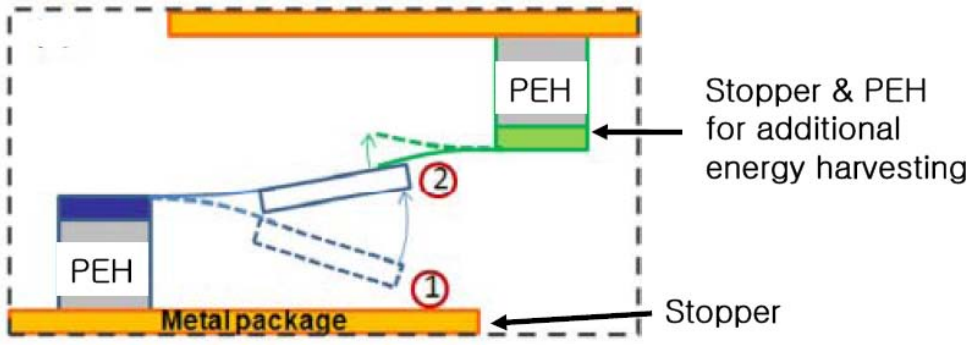

Figure 2.20 PEH with stopper and additional PEH for energy harvesting [53].

A general cantilever vibrates with one degree of freedom in vertical direction. Xu et al. and Kim et al. [55, 56] increased degree of freedom by attaching additional cantilever normal to the PEH and rotating mass between two cantilevers. The PEHs exhibited resonant behavior at

two frequencies and frequency band was observed due to narrow distance between the resonance peaks.

Challa et al.[57] controlled stiffness of cantilever beam using magnetic force. Repulsive and attractive force were applied to the cantilever between permanent magnets attached on the top and bottom of proof mass, and below and over the permanent magnets of the cantilever as shown in figure 2.21. Reasonable power level was produced between 22 and 31 Hz.

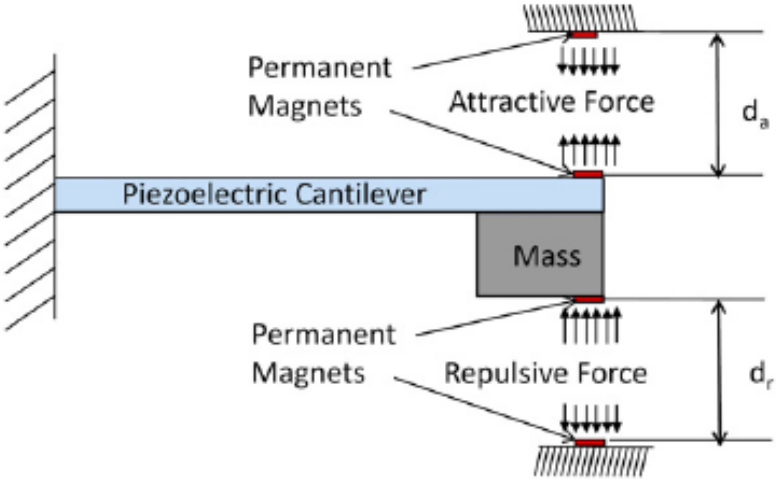

Figure 2.21 Cantilever stiffness control by magnetic force [57].

Nonlinearity is the most widely studied mechanism to extend working frequency range of a PEH. Cottone et al. [58] proposed nonlinear behavior of cantilever by using repulsive force between permanent magnets. The authors calculated potential energy of cantilever as a function of displacement at various distance between magnets as presented in figure 2.22. Width of potential energy well indicates working frequency range of the device. The cantilever is unstable at zero displacement when the repulsive force is strong (distance is 6 and 7 mm), and possesses two stable displacement position off zero displacement. The cantilever works in narrow

frequency range when the repulsive force is low (distance is 15 mm), and has narrow resonance frequency range. The stable displacement range is wide when distance between magnets is 11.2 mm (dotted line in figure 2.22). The broadening of working frequency range is explained two terms; two equilibrium position separated by magnetic repulsive force and jumping between the two potential wells. Stanton et al. and Erturk et al. [59, 60] added two permanent magnets for two equilibrium positions of cantilever.

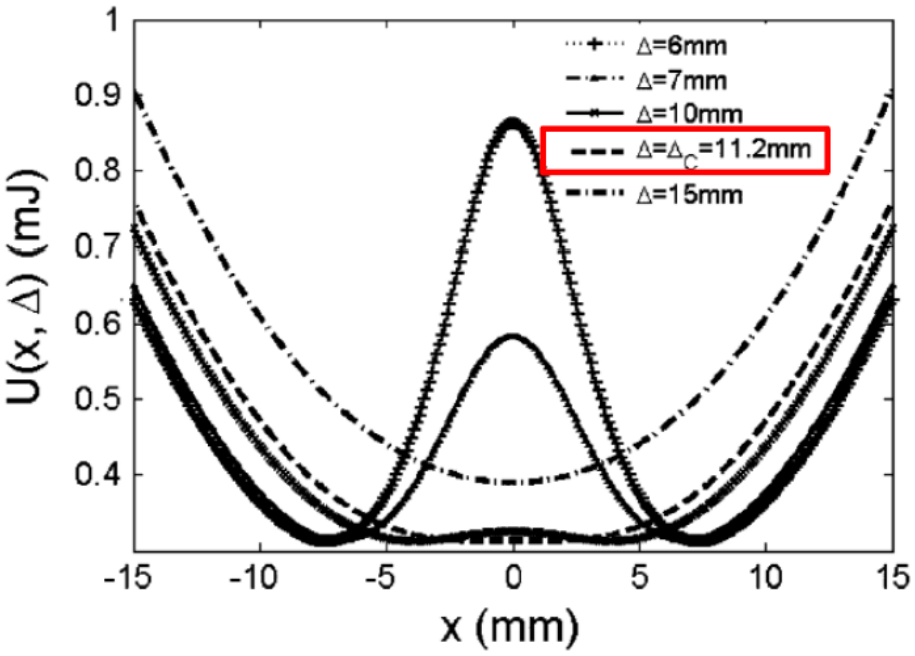

Figure 2.22 Potential energy depending on distance between magnets; one magnet is attached at the end of cantilever free end and the other is placed in length direction of the cantilever [58].

Hajati and Kim [61] achieved nonlinearity of a PEH by using double clamping of a beam. The device produced electric energy in the frequency range between 1 kHz and 2.75 Khz when the tensile force was applied to the beam by clamping. Dai et al. demonstrated nonlinear

behavior from a PEH using various structure as shown in figure 2.23 [62].

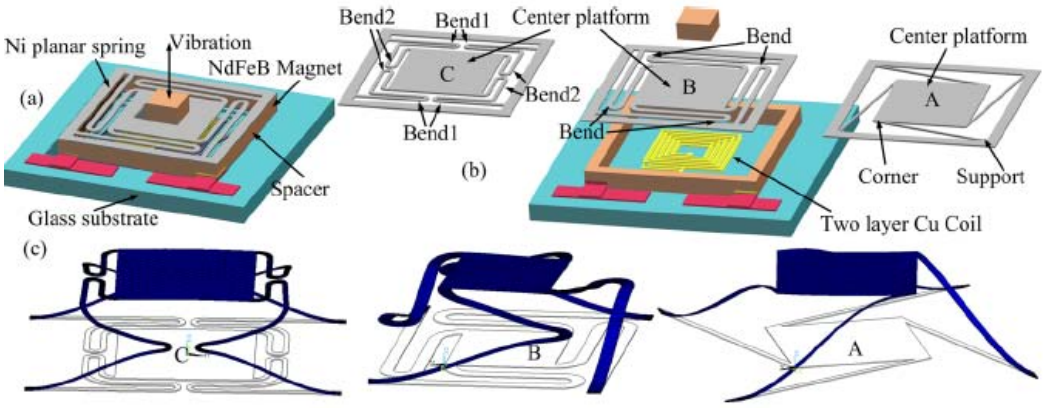

Figure 2.23 Various structures for nonlinear stiffness of PEH [62].

CHAPTER 3 EXPERIMETNAL METHOD

This chapter covers device preparation and characterization process.

3.1 Device fabrication

Three types of devices were prepared for three subjects. This section describes for the devices fabrication processes.

3.1.1 Bulk scale devices based on soft and hard PZT

Bulk scale devices were used in experiment to examine temperature effect on the performance of PEH. The PEHs were based on soft and hard PZT. Bimorphs beams were purchased from a company (piezo.com) to fabricate the PEHs. Picture of the commercial piezoelectric beams is given in figure 3.1. The brown (left) and dark green (right) stripe represent hard (T215-A4-103Y) and soft PZT (T215-H4-103Y) based bimorphs, respectively. The beams consist of three layers, PZT-brass-PZT layer, and covered with conductive Ni electrode. Dimension of as purchased beam is 31.8 x 3.2 x 0.38 mm^3 (length x width x thickness). PZT was removed at the tip for wiring and wired side was fixed between metal holder as shown in figure 3.2 (a). Since poling direction is identical in both PZT layers, three wires were connected as shown in figure 3.2 (b). Nonconductive tape (yellow colored in figure 3.2 (a)) was inserted between metal holder and piezoelectric beam to prevent electric shortage. The assembled cantilever was fixed on stage as presented in figure 3.3. Following subsection covers fabrication of a MEMS scale device used to compare performance of bulk and MEMS scale device in temperature change.

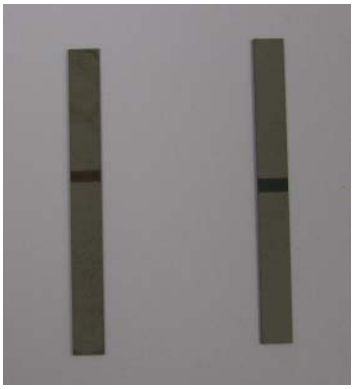

Figure 3.1 Commercial piezoelectric bimorph from piezo.com. Left and right beam are made of hard and soft PZT, respectively.

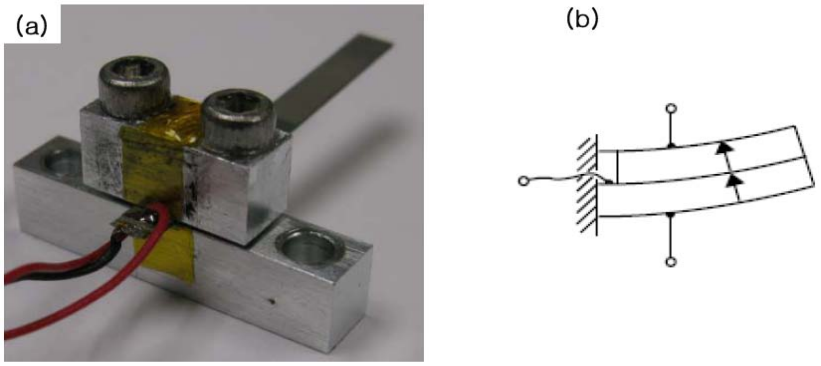

Figure 3.2 (a) A cantilever in metal holder (b) poling direction and wiring for parallel operation.

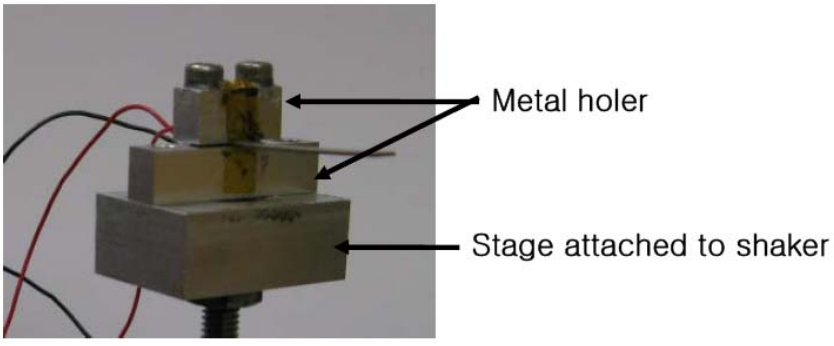

Figure 3.3 A cantilever attached on sample stage of shaker.

3.1.2 MEMS scale PEH fabrication

Silicon based MEMS scale PEHs were used for two subjects; comparison of bulk and MEMS scale devices, verification of output power model in d_{33} mode PEH and performance comparison between d_{31} and d_{33} mode PEH. The design and fabrication process are as following.

Photomasks were designed by Auto CAD program and device dimension were determined considering target frequency. The images of the masks are given in figure 3.4 and 3.5 for d_{31} and d_{33} mode devices, respectively. Resonance frequency was estimated by Yi et al.'s equation [63] as elaborated in chapter 4. Device dimensions were designed with two types in a wafer; type 1 consists of 3 x 1 x 0.021 mm^3 (length x width x thickness) of cantilever and 2 x 1 x 0.521 mm^3 (length x width x thickness) of proof mass; type 2 consists of 4 x 2 x 0.021 mm^3 (length x width x thickness) of cantilever and 3 x 2 x 0.521 mm^3 (length x width x thickness) of proof mass. Type 1 devices were used for research on piezoelectric mode dependent output power of PEH (d_{33} and d_{31} mode based PEHs). Type 2 PEH was used as a MEMS scale device in the research on the thermal degradation of the PEH. Expected resonance frequencies of the devices are 245 and 124 Hz, respectively. The device fabrication process is schematically illustrated in figure 3.6 and 3.7 for the d_{31} and d_{33} mode device, respectively. The cantilever area was covered with top electrode in the d_{31} mode devices. As presented in 3.6 (b), (c), and (d), side of cantilever area (40 μm width) was not coated with top electrode for tolerance in the d_{31} mode device fabrication. IDE was formed in the cantilever area of the d_{33} mode devices, and figure 3.8 shows top view of a d_{33} mode device. Spacings between electrodes (g) are 4, 8, 12, and 16 μm. Widths of finger electrodes (w) are 8, 12, and 16 μm. A set is 12 devices in d_{33} mode PEH. The margin was considered in the d_{33} mode devices as well. Spacing between busbars (side lines) (C_w) is 0.8 mm and 1.8 mm when width of cantilever (M_w) is 1 mm and 2 mm,

respectively. Gap between busbar and finger electrode (*a*) is 150 % of finger spacing (*g*) to collect change only between finger electrodes.

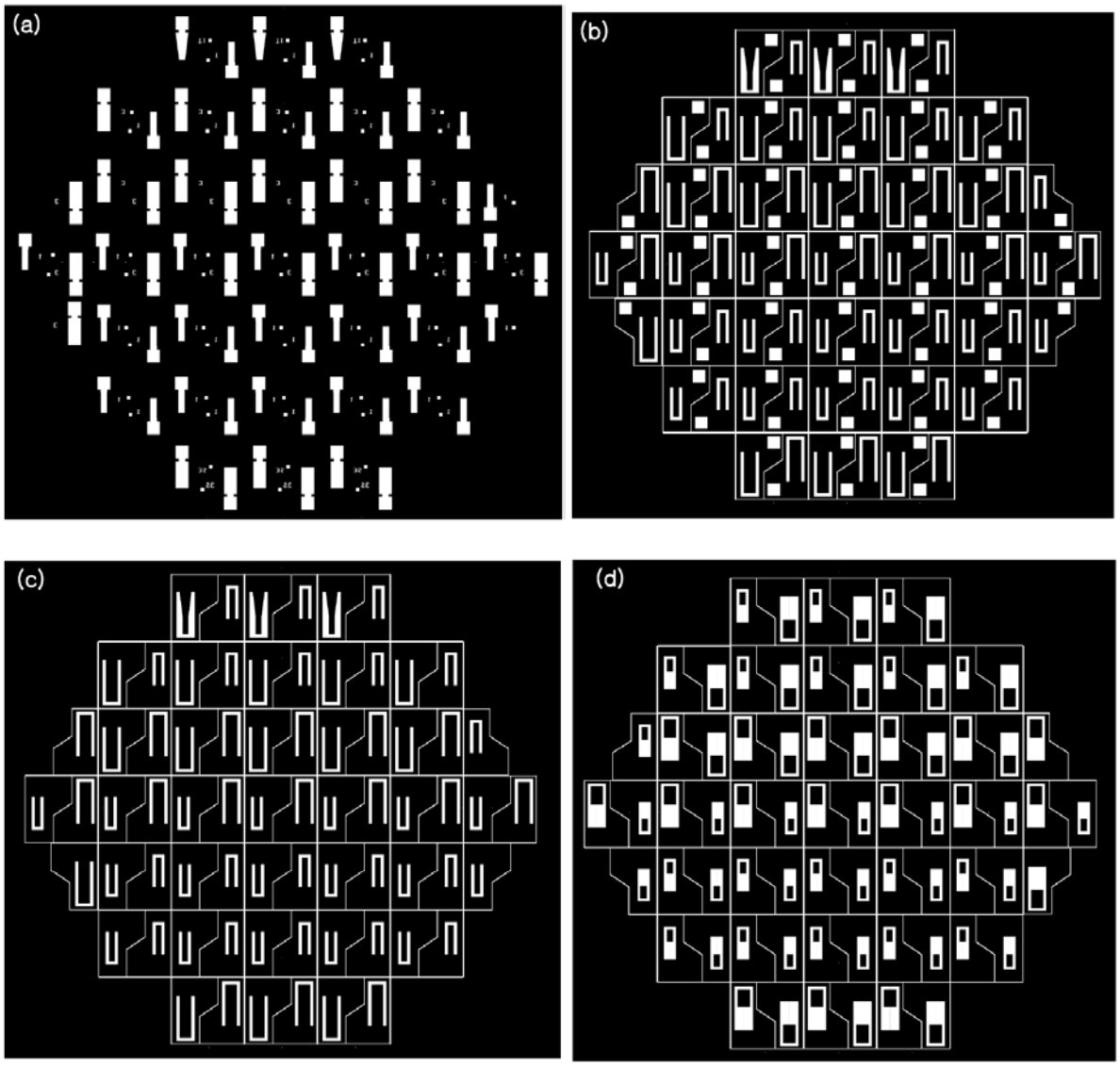

Figure 3.4 Photomask design for d_{31} mode device fabrication. (a) Top electrode deposition (b) Piezoelectric layer etching (c) Cantilever (bottom electrode, SiO_2 electrical passivation layer, Si device layer and buried SiO_2 layer) etching (d) Backside (SiO_2 on backside and Si handling layer) etching.

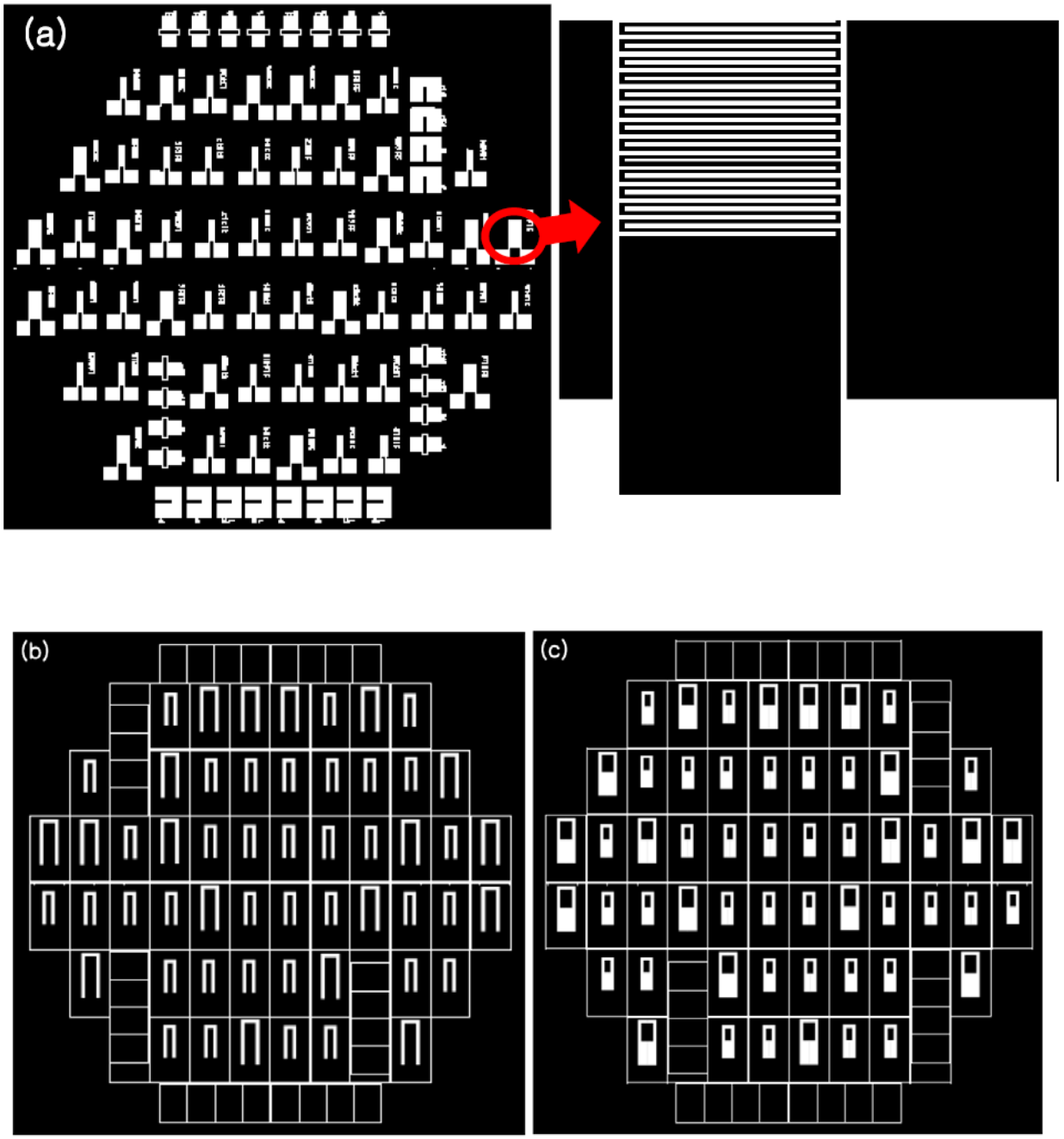

Figure 3.5 Photomask design for d_{33} mode device fabrication. (a) Top electrode (IDE) deposition (b) Cantilever (piezoelectric layer, seed layers, SiO_2 electrical passivation layer, Si device layer and buried SiO_2 layer) etching (c) Backside (Si handling layer).

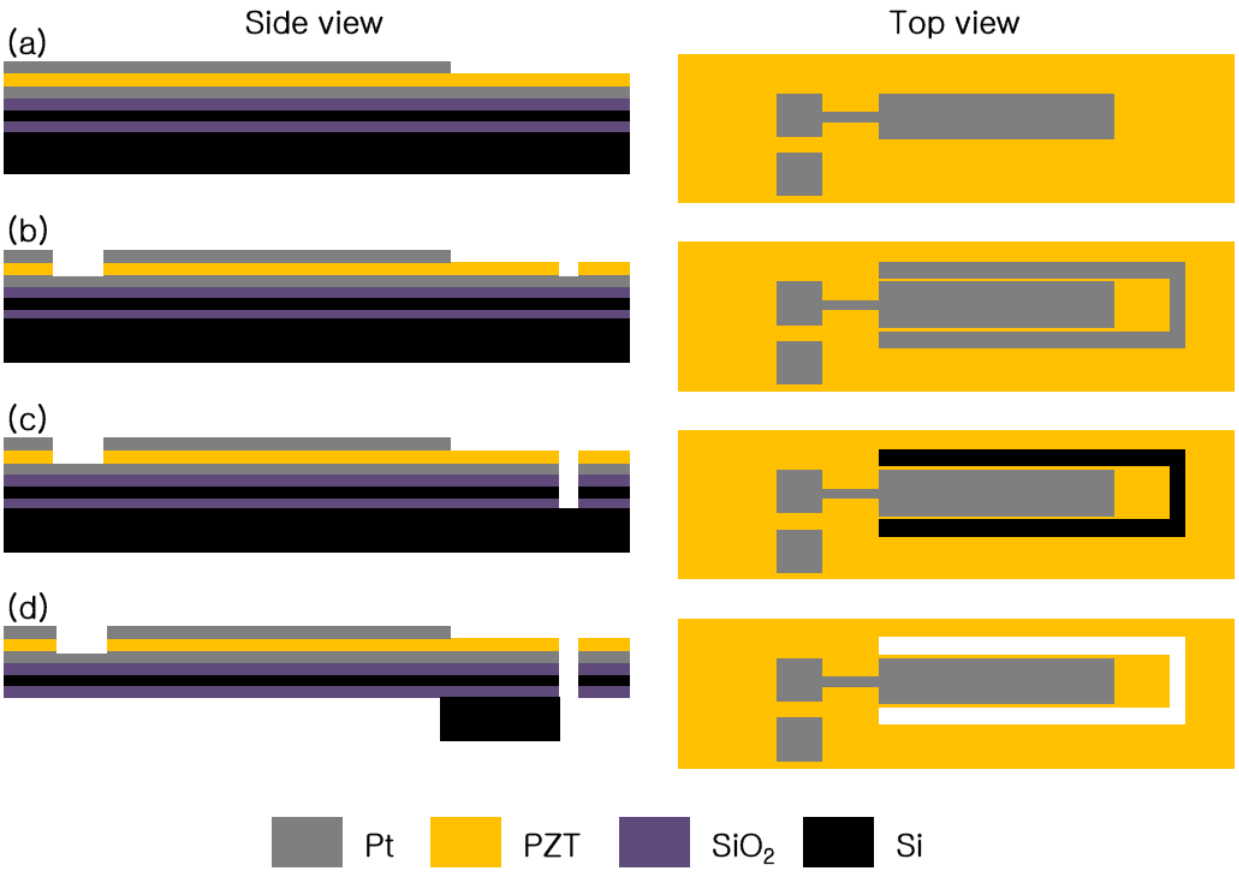

Figure 3.6 Schematic illustrations for a d_{31} mode device fabrication process.

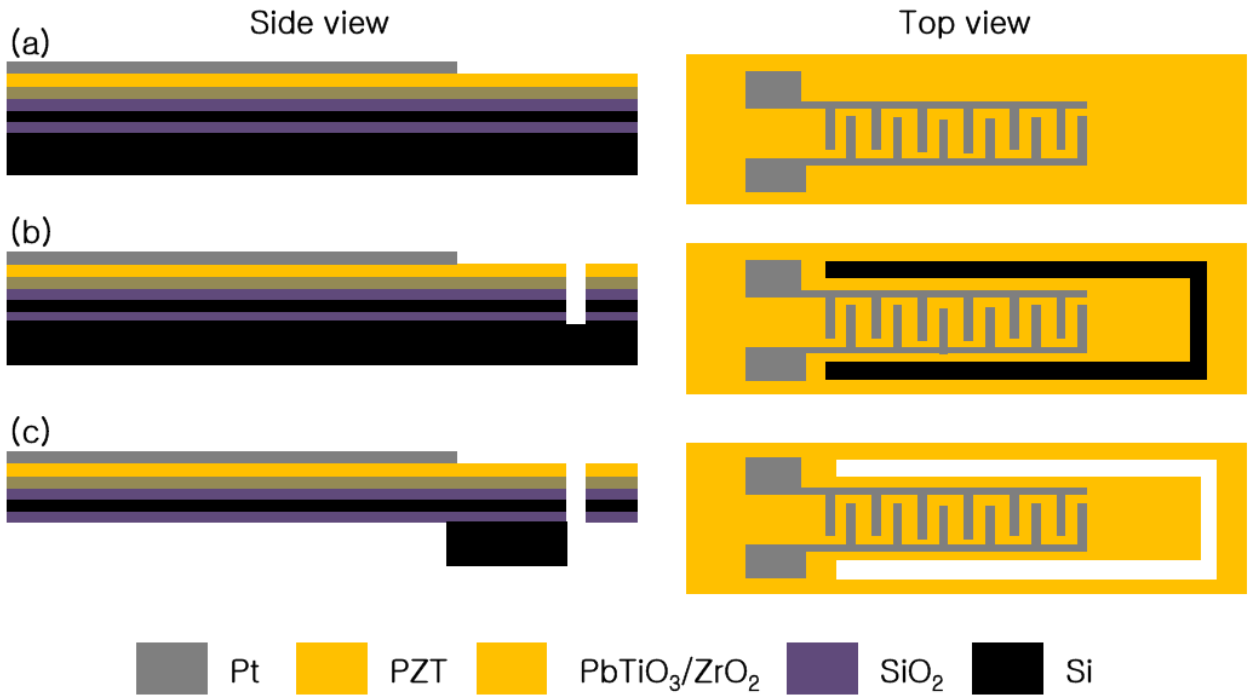

Figure 3.7 Schematic illustrations for d_{33} mode device fabrication process.

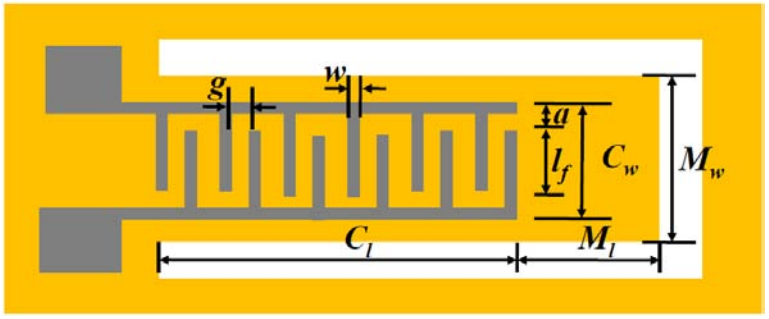

Figure 3.8 Top view of d_{33} mode device.

All Si based PEHs were based on 4 inch silicon on insulator (SOI) wafer for uniform and precise cantilever thickness. The SOI wafer consists of 500 μm thick handling layer, 500 nm thick buried SiO_2, and 20 μm thick Si device layer from bottom to top. Thickness of cantilever may be non-uniform when device is fabricated based on normal Si wafer and physical etching

[64]. Buried SiO_2 in SOI wafer works as a etch stop so that device are made with uniform thickness. 500 nm thick SiO_2 was thermally grown on device layer for electrical passivation. 100 nm thick platinum was deposited as a bottom electrode with (111) orientation for d_{31} mode device by dc sputtering. In the d_{33} mode fabrication, ZrO_2 (180 nm thick) and $PbTiO_3$ (10 nm thick) layer were spin coated on the electrical passivation layer and annealed to serve as diffusion barrier and seed layer for PZT layer, respectively. Sol-gel solutions were prepared by Inostek, Inc, and ratio between Zr/Ti is 52/48 in PZT solution. 1 μm thick PZT film was deposited on seed layers. The piezoelectric layer fabrication process and conditions are illustrated in figure 3.9. Top electrode and IDE were deposited with photo-resist patterning for d_{31} and d_{33} mode device, respectively (figure 3.6 (a) and figure 3.7 (a), respectively). Lift-off process was followed to remove photo-resist pattern in acetone. Etching mask was formed using photo-resist (20 μm thick) by photolithography. Advanced oxide etcher (AOE) and advanced silicon etcher (ASE) etcher etched oxides and silicon layers selectively, respectively. The etching machines are manufactured by STS multiplex and based on inductively coupled plasma reactive ion etching (ICP RIE). Etching order is as follows; d_{31} mode device – PZT etching using mask (b) in figure 3.4 (figure 3.6 (b)) →Pt bottom electrode, SiO_2 electrical passivation layer, Si device layer, buried SiO_2 layer using mask (c) in figure 3.4 (figure 3.6 (c)) → SiO_2 on backside and Si handling layer using mask (d) in figure 3.4 (figure 3.6 (d)); d_{33} mode device – PZT, seed layers, SiO_2 electrical passivation layer, Si device layer and buried SiO_2 layer using mask (b) in figure 3.5 (figure 3.7 (b)) → SiO_2 on backside and Si handling layer using mask (c) of figure 3.5 (figure 3.7 (c)). Figure 3.10 and 3.11 show picture of d_{31} mode device wafer after top side etching, and backside SiO_2 etching, respectively. Picture of final devices are given in figure 3.12.

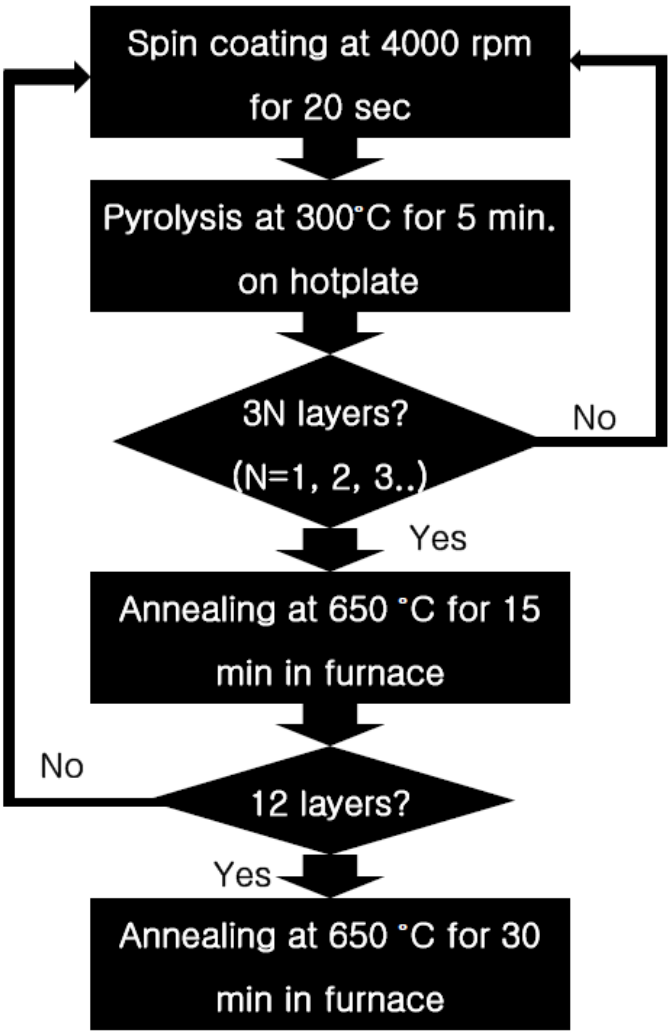

Figure 3.9 PZT film fabrication process.

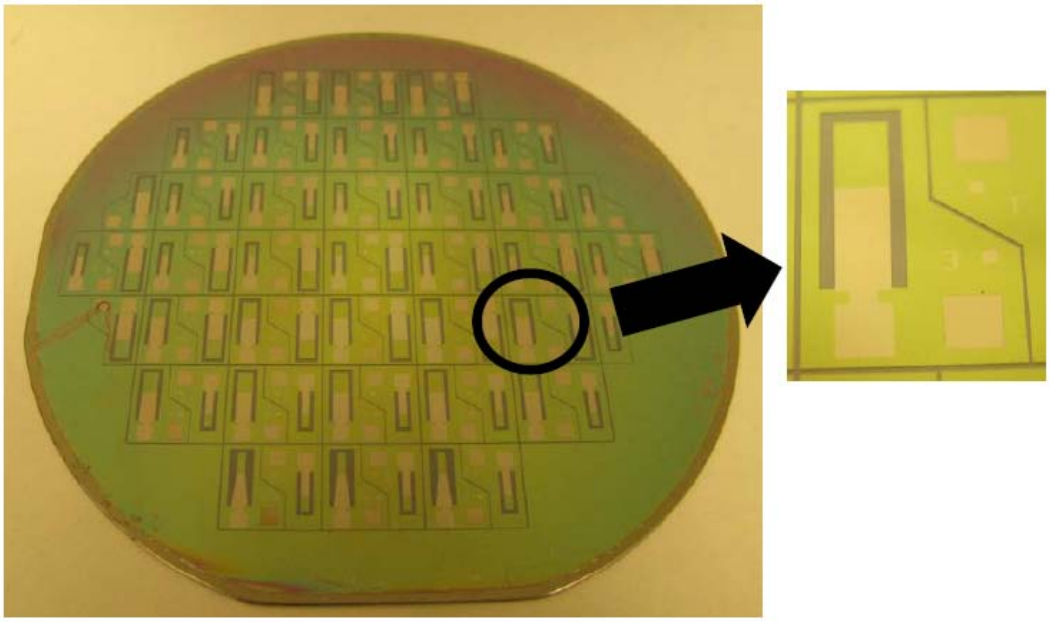

Figure 3.10 Image of d_{31} mode device wafer after top side etching.

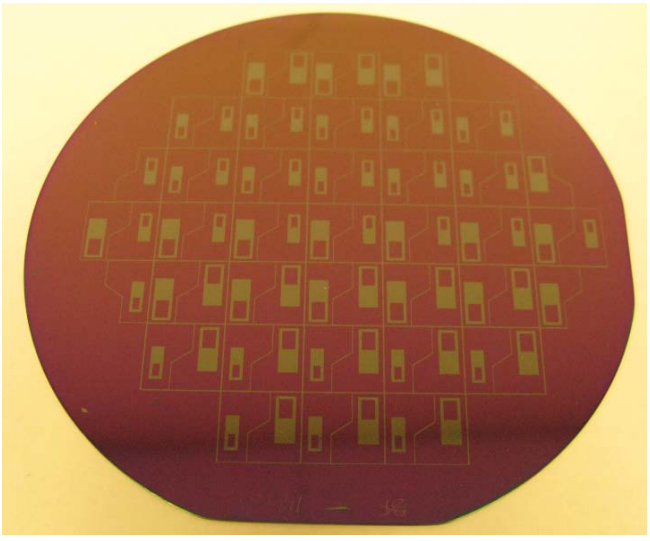

Figure 3.11 Image for d_{31} mode device wafer after backside SiO_2 etching.

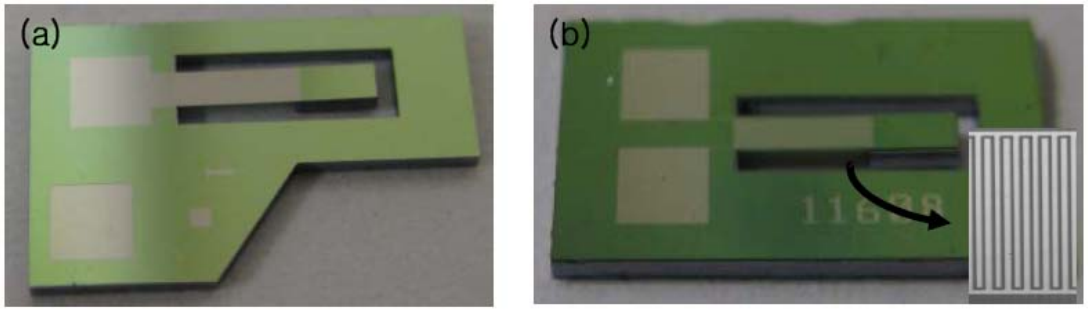

Figure 3.12 Picture of final devices (a) d_{31} mode PEH (b) d_{33} mode PEH.

3.1.3 Magnetic substrate based PEH

Flexible magnetic substrate based PEH is used for the research on wideband PEH. The magnetic sheet is amorphous phase iron-nickel based magnetic alloy (2826 MB) purchased from Metglas Inc. Table 3.1 summarizes electrical and physical properties of 2826 MB.

Table 3.1 Physical and electrical properties Metglas 2826MB [65].

Thickness	28 mm
Density	7.9 g/cm^3
Elastic modulus	100-110 Gpa
Curie temperature	353˚C
Continuous service temperature	125˚C
Electrical resistivity	138 μohm-cm

Since substrate serves as a bottom electrode, piezoelectric ZnO thin film was deposited

with negative pattern of mask in figure 3.4 (b) to prevent material deposition on bottom electrode pad. ZnO thin film was deposited by sputtering and Cu was co-sputtered for doping due to low electrical resistivity of pure ZnO on amorphous phase. Three inch sized ZnO ceramic and Cu metal target were attached on RF and DC cathode, respectively. Power was 80 W on RF cathode. Power for Cu metal target was 1, 3, and 5 W for different doping concentration. Deposition rate was 5.5 nm/min. Photo-mask (a) in figure 3.4 provided pattern for aluminum top electrode. The 100 nm thick top electrode was sputtered for 450 second with 100 W. Substrate was attached on dummy wafer for uniform photo-resist coating and handling during fabrication. Device was cut by scissor with extreme care to define size of cantilever precisely. Each device was wired for characterization as shown in figure 3.14.

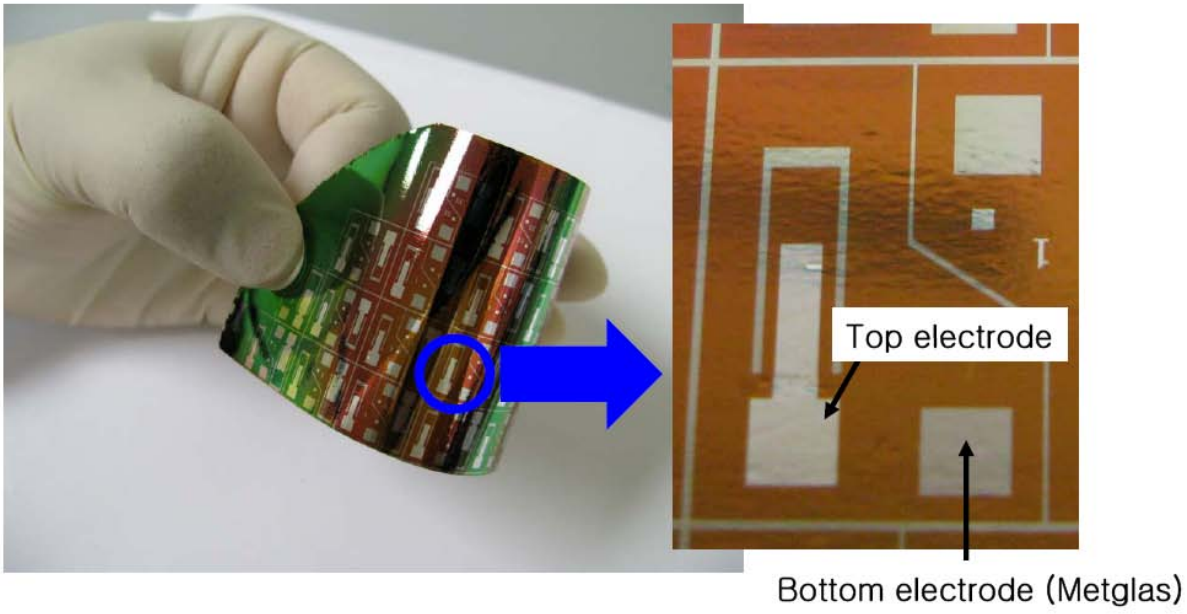

Figure 3.13 Wafer for flexible magnetic substrate based PEH and a device on the wafer.

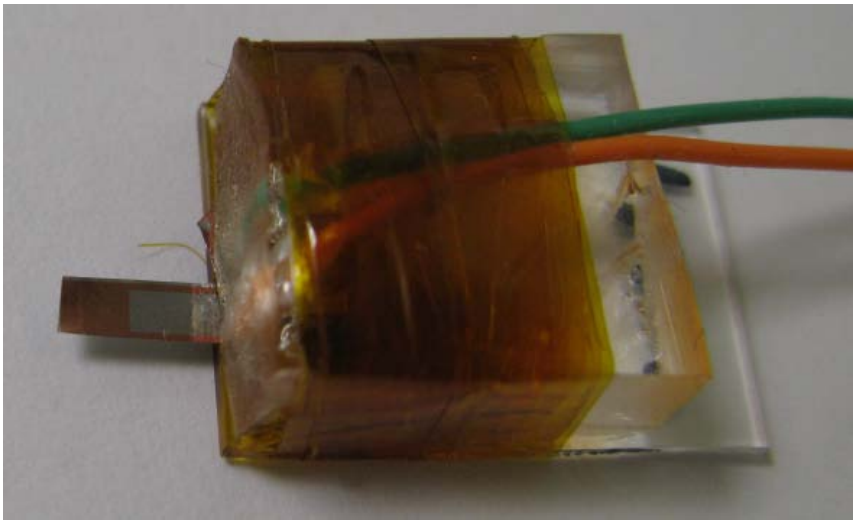

Figure 3.14 A magnetic substrate based PEH with wires.

3.2 Device and material property characterization

This section covers instrumental setup and procedure for material property characterization and performance evaluation.

3.2.1 Materials' property characterization

TF analyzer 2000 (figure 3.15 (a)) and Precision LC (figure 3.16) measured ferroelectric properties and applied DC electric field for poling. Available maximum voltage is 25 V and 40 kV in TF analyzer and Precision LC, respectively. Poling was performed with 200 kV/cm at 100 $^{\circ}$C on hot plate for 10 min. Electric current was monitored for damage by electric field and damaged devices were excluded.

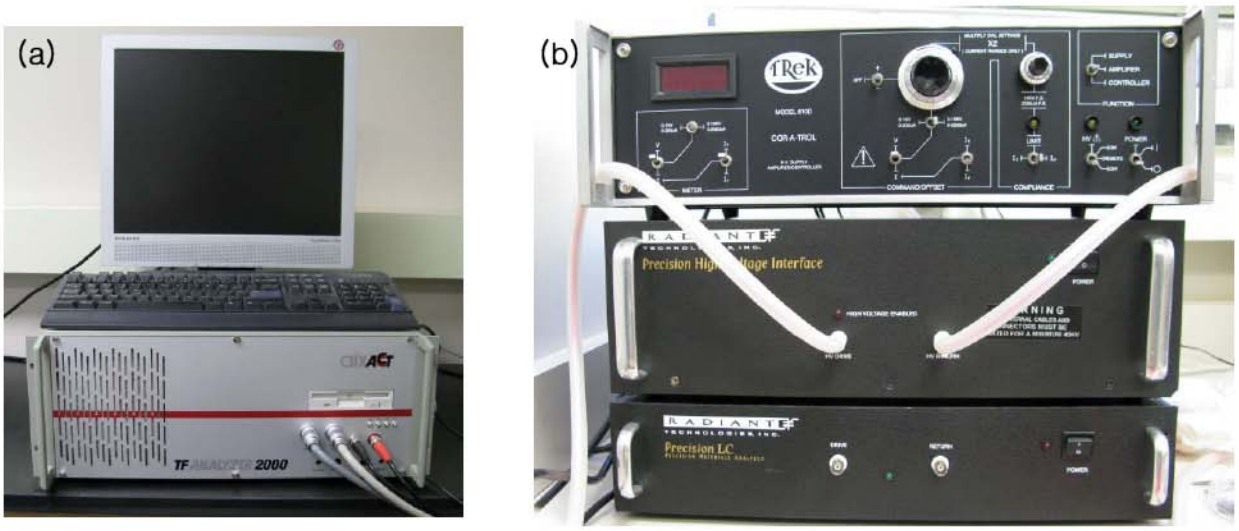

Figure 3.15 Instruments for ferroelectric property characterization and dc poling. (a) TF analyzer 2000 (AixAcct) (b) Precision LC (Radiant).

Impedance analyzer (figure 3.16) characterized capacitance and dielectric property as function of frequency and voltage. Dielectric constant was calculated based on capacitance measurement, thickness of dielectric layer, and area of electrode.

Figure 3.16 Impedance analyzer for dielectric property characterization (HP 4192).

Semiconductor analyzer (HP 4156 A, figure 3.17) evaluated electrical resistivity of pure and Cu doped ZnO.

Figure 3.17 Semiconductor parameter analyzer (HP 4156A).

Scanning electron microscope (SEM) (JEOL-FESEM) was used to observe image of samples and X-ray diffraction (XRD) (Bruker D8) characterized structural properties.

3.2.2 Device evaluation – Cantilever on shaker

Performance of devices was measured upon vibration. Figure 3.18 shows experimental setup for device output power measurement. A sample was attached on the sample stage at the center of the figure. Function generator (right top of figure) produced sine wave and the signal was amplified by an amplifier. The shaker moves up and down by the amplified signal. An accelerometer monitored vibration strength, and the amplifier controlled the acceleration value. An oscilloscope was connected to the device for output voltage measurement. No resistor was connected for open circuit voltage (OCV) measurement. Resistor was connected in parallel with the oscilloscope, and varied to evaluate the output voltage as a function of resistive load. Output

power was calculated by V_{rms}^2/R, where V_{rms} and R are root mean square (rms) of output voltage and connected resistive load.

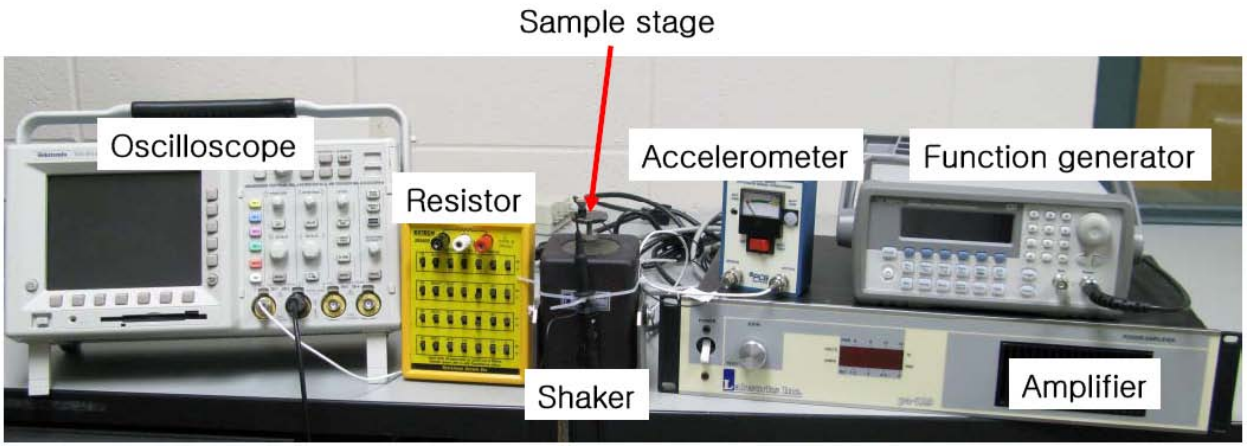

Figure 3.18 Experimental setup for device performance.

The PEHs were placed in a temperature box to evaluate performance of a device at elevated temperature condition as shown in figure 3.19. A resistive heater (right top of the figure) was placed in the conditioning box and temperature was controlled by a heater controller. A thermocouple was installed in the heating chamber to monitor temperature. Heat soaking time was given for 10 min when temperature was stable. The space for the sample and shaker was divided so that the shaker is not heated. Top side of the temperature box was closed with transparent acryl plate to monitor the sample. As described in device fabrication process and figure 3.19, the sample was fixed between metal holders to prevent change of sample holding strength.

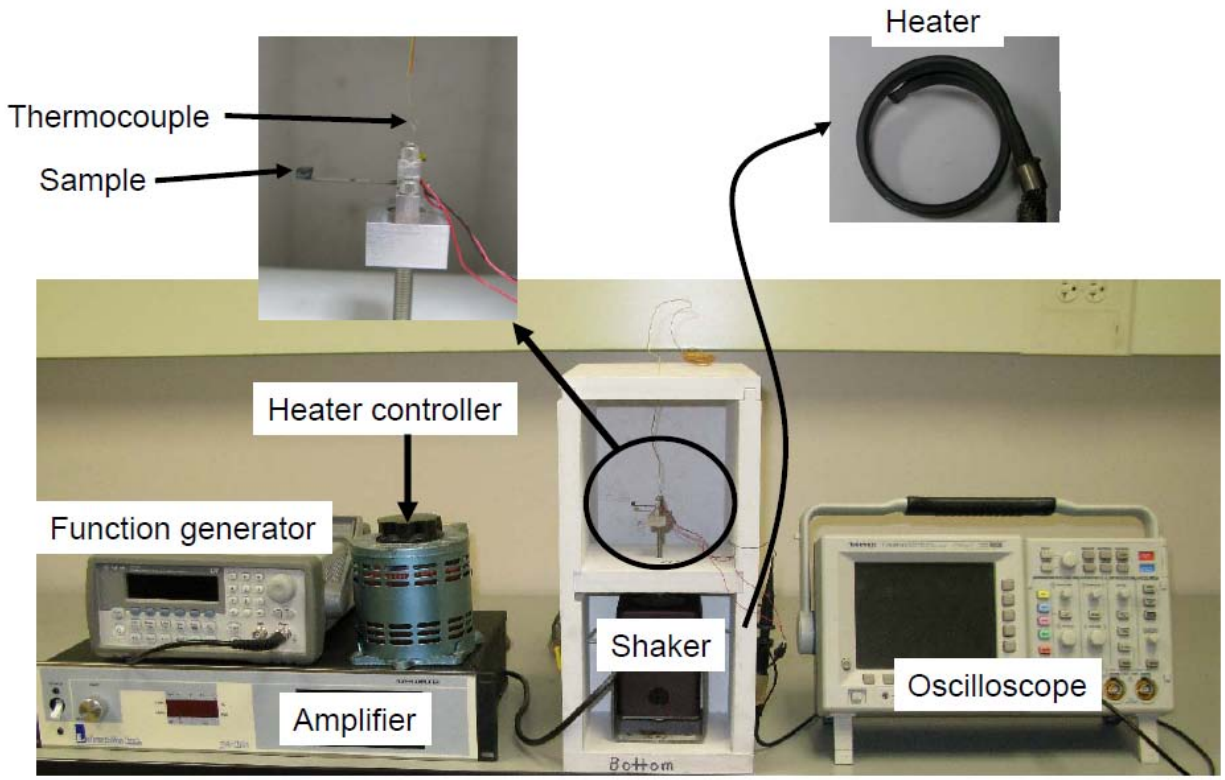

Figure 3.19 Experimental setup for output power measurement under temperature condition.

3.2.3 Device evaluation – Forced vibration by magnetic field

Figure 3.20 shows experimental setup for forced vibration of magnetic cantilever. A permanent magnet was installed on the shaker and vibrated in vertical direction by shaker's motion. The magnetic cantilever with piezoelectric materials was installed on the other stage. Signal from the device was read by oscilloscope.

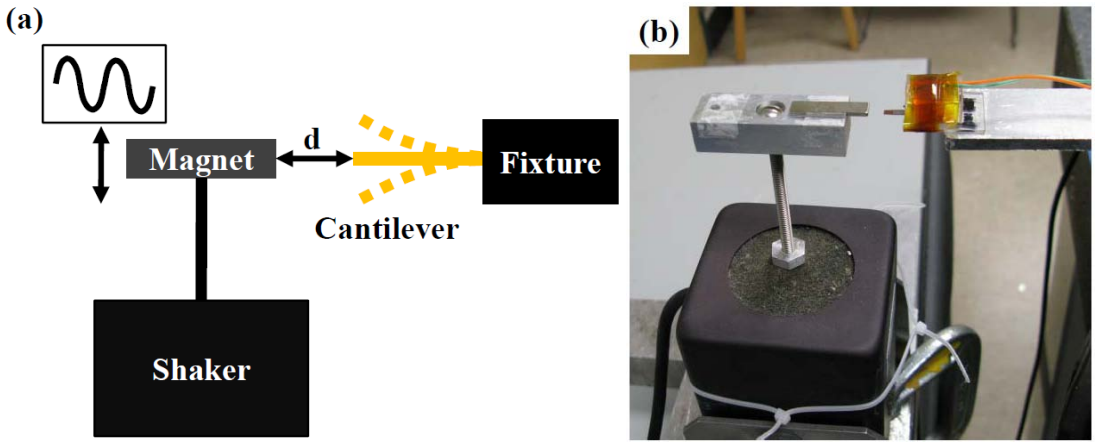

Figure 3.20 Experimental setup for forced vibration by magnetic field. (a) Schematic diagram (b) picture of the setup showing magnet and cantilever.

CHAPTER 4 MATHEMATICAL MODELING

4.1 Introduction

Motion of a device is result from combination of complex factors such as materials parameters and dynamics in a device. A clear modeling for the device provides understanding for contribution by each factor and working mechanism of the device. In addition, direction towards optimum design for device applications may be known through mathematical analysis.

Output power estimation model for the d_{31} mode PEH is based on Roundy's analytical model [8]. This chapter describes Roundy's model and modifications for unimorph and d_{33} mode device. Behavior of magnetically actuated Metglas based PEH is modeled by MATLAB Simulink.

4.2 Roundy's analytical model [8]

Roundy [8] developed a mathematical equation to estimate output power of a bimorph d_{31} mode PEH. This section summarizes Roundy's work because output power model of this research is based on the work. Figure 4.1 illustrates a PEH for modeling. The cantilever was fixed on vibrating stage and vibrated in *z* direction while stress was in *x* direction. Equivalent circuit was considered assuming mechanical components of the PEH as electrical components as given in figure 4.2. Input external vibration (σ_{iv}) ramifies to mechanical stress by proof mass (σ_{pm}), for damping element (σ_{dr}), for cantilever stiffness (σ_{E}), and for electric energy (σ_{ct}). The stress elements are described as alternative power source, inductor, resistor, capacitor, and transformer, respectively, which are calculated by equation (4.1) to (4.5).Variables and constants are listed in table 4.1. Damping elements was combined with other variables and simplified into

damping ratio. Geometrical factor g_f^* and g_f^{**} are calculated by equation (4.6) and (4.7). Area moment of inertia I is calculated by equation (4.8). Since stress energy elements are parts of input vibration energy, summation of stress elements is identical with input vibration as given in equation (4.9).

Table 4.1 Variables and constants used in equations.

m_{pm}	Proof mass
δ_{pc}	Strain in piezoelectric layer
b_r	Damping element
Y_{pc}	Elastic modulus of piezoelectric layer
d_{31}	Piezoelectric constant
E	Electric field between electrodes
g_f^* and g_f^{**}	Geometrical factor calculated by equation (4.6) and (4.7)
l_e	Length of electrode
l_{np}	Distance between neutral layer and center of piezoelectric layer, $(t_p+t_s)/2$
I	Area moment of inertia
w_c	Width of cantilever
n_p	Number of piezoelectric layer
t_p	Thickness of piezoelectric layer
Y_s	Elastic modulus of structural layer
t_s	Thickness of structural layer

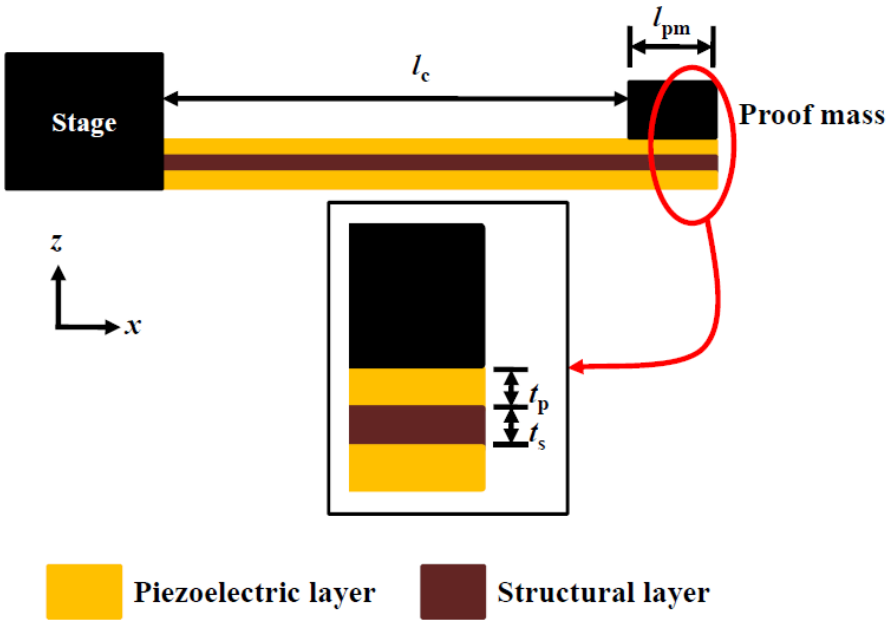

Figure 4.1 Schematic illustrations for a d_{31} mode bimorph for modeling.

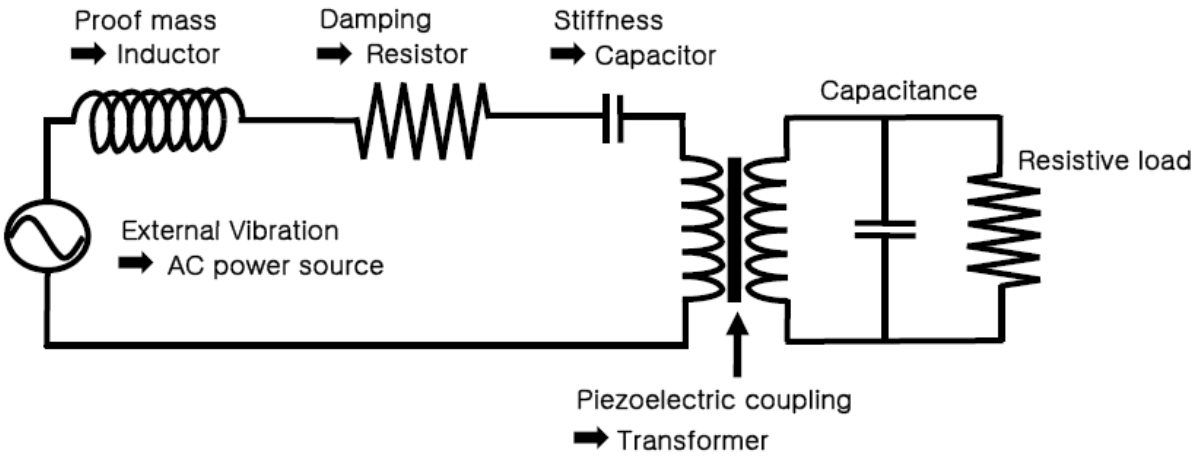

Figure 4.2 Equivalent circuit model of PEH.

$$\sigma_{iv} = \frac{m_{pm}}{g_f^{**}} \ddot{z} \tag{4.11}$$

$$\sigma_{pm} = \frac{m_{pm}}{g_f^{*} g_f^{**}} \ddot{\delta}_{pc} \tag{4.12}$$

$$\sigma_{dr} = \frac{b_r}{g_f^{*}} \dot{\delta}_{pc} \tag{4.13}$$

$$\sigma_E = Y_{pc} \delta_{pc} \tag{4.14}$$

$$\sigma_{ct} = -d_{31} Y_{pc} E \tag{4.15}$$

$$g_f^{*} = \frac{3 l_{np} \left(l_c + l_{pm} \right)}{l_c^2 \left(2 l_c + 1.5 l_{pm} \right)} \tag{4.16}$$

$$g_f^{**} = \frac{2I}{l_{np}(2 l_c + l_{pm} - l_e)} \tag{4.17}$$

$$I = \frac{w_c n_p t_p^2}{12} + w_c n_p l_{np}^2 + \frac{Y_{pc}}{Y_s} \frac{w_c t_s^3}{12} \tag{4.18}$$

$$\sigma_{iv} = \sigma_{pm} + \sigma_{dr} + \sigma_E + \sigma_{ct} \tag{4.19}$$

Right side of transformer in figure 4.2, capacitor and resistive load, indicates electrical components of the PEH, i.e. generated electric charge (Q_{tc}) is stored and consumed in the capacitor (Q_{pc}) and resistive load (Q_{rr}), respectively, as shown in equation (4.10). Q_{tc} is function of electrode area and dielectric displacement (D_p) as given equation (4.11). The current is obtained by equation (4.12) and (4.13) in capacitor and resistive load, respectively, where V_g is generated voltage; R_r is resistive load. C_{pc} is capacitance of piezoelectric layer and calculated by equation (4.14), where ε_0 and ε_r are dielectric permittivity of vacuum and relative dielectric constant.

$$\dot{Q}_{tc} = \dot{Q}_{pc} + \dot{Q}_{rr} \tag{4.20}$$

$$\dot{Q}_{tc} = n_p l_e w_c \dot{D}_p = n_p l_e w_c d_{31} Y_{pc} \dot{\delta}_{pc} \tag{4.21}$$

$$\dot{Q}_{pc} = 2C_{pc}\dot{V}_g \tag{4.22}$$

$$\dot{Q}_{rr} = V_g / R_r \tag{4.23}$$

$$C_{pc} = \frac{n_p \varepsilon_0 \varepsilon_r w_c l_e}{t_p} \tag{4.24}$$

Substitution of stress elements in equation (4.9) and rearrangement produce equation (4.15). Spring constant of cantilever k_s replaces $Y_{pc} g_f^{*} g_f^{**}$. Substitution of charge elements in equation (4.10) and rearrangement result equation (4.16). Laplace transformation changes the equations from time domain to complex domain as shown in equation (4.17) and (4.18), where u and s are Laplace transformed strain and Laplace variable. Equation for V_g is obtained by substituting u in equation (4.17) to (4.18) as given in equation (4.19). The term k_s/m_{pm}, $b_r g_f^{**}$, and $d_{31}^2 Y_{pc}/\varepsilon_0 \varepsilon_r$ can be simplified by natural frequency (ω_n^2), damping term ($2\zeta\omega_n$), and piezoelectric coupling coefficient (κ^2) as given in equation (4.20). Equation for voltage V_g at resonance condition is obtained by replacing Laplace variable with $i\omega_n$, where i is imaginary number. Imaginary number disappears in square of V_g as given in equation (4.21). Since output power is calculated by V_g^2/R_r, output power from bimorph PEH (P_{B31}) is calculated by equation (4.22). The resistance for maximum power (R_{mp}) is calculated by differentiating equation (4.22) and letting it zero as shown in equation (4.23).

$$\ddot{\delta}_{pc} = -\frac{Y_{pc} g_f^{*} g_f^{**}}{m_{pm}} \delta_{pc} - \frac{b_r g_f^{**}}{m_{pm}} \dot{\delta}_p + \frac{d_{31} Y_{pc} g_f^{*} g_f^{**}}{m_{pm} t_p} V_g + g_f^{*} \ddot{z} \tag{4.25}$$

$$\dot{V}_g = -\frac{d_{31} Y_{pc} t_p}{\varepsilon_0 \varepsilon_r} \delta'_{pc} - \frac{1}{R_r C_p} V_g \tag{4.26}$$

$$u = -\frac{\varepsilon_0 \varepsilon_r}{Y_{pc} d_{31} t_p}\left(s + \frac{1}{R_r}\right) \tag{4.27}$$

$$u\left(s^2 + \frac{b_r g_f^{**}}{m_{pm}} + \frac{k_s}{m_{pm}}\right) = \frac{k_s d_{31}}{m_{pm} t_p} V_g + g_f^* a_{in} \tag{4.28}$$

$$\begin{aligned} &\frac{Y_{pc} d_{31} t_p g_f^* a_{in}}{\varepsilon_0 \varepsilon_r} \\ &= -\frac{V_g}{s}\left[s^3 + s^2\left(\frac{1}{R_r C_{pc}} + \frac{b_r g_f^{**}}{m_{pm}}\right) + s\left(\frac{k_s}{m_{pm}} + \frac{k_s d_{31}^2 Y_p}{m_{pm}\varepsilon_0 \varepsilon_r} + \frac{b_r g_f^{**}}{m_{pm}} \cdot \frac{1}{R_r C_{pc}}\right) + \frac{k_s}{m_{pm} R_r C_{pc}}\right] \end{aligned} \tag{4.29}$$

$$\begin{aligned} &\frac{Y_{pc} d_{31} t_p g_f^* a_{in}}{\varepsilon_0 \varepsilon_r} \\ &= -\frac{V_g}{s}\left[s^3 + s^2\left(\frac{1}{R_r C_{pc}} + 2\zeta\omega_n\right) + s\left\{\omega_n^2(1+\kappa^2) + 2\zeta\omega_n \frac{1}{R_r C_{pc}}\right\} + \frac{\omega_n^2}{R_r C_{pc}}\right] \end{aligned} \tag{4.30}$$

$$V_g = \frac{a_{in}}{\omega_n} \frac{\dfrac{R_r C_{pc} Y_{pc} d_{31} t_p g_f^*}{\varepsilon_0 \varepsilon_r}}{\sqrt{(4\zeta^2 + \kappa^4)(R_r C_{pc}\omega_n)^2 + 4\zeta\kappa^2 (R_r C_{pc}\omega_n) + 4\zeta^2}} \tag{4.31}$$

$$P_{B31} = \frac{a_{in}^2}{\omega_n^2} \frac{R_r\left(\dfrac{C_{pc} Y_{pc} d_{31} t_p g_f^*}{\varepsilon_0 \varepsilon_r}\right)^2}{(4\zeta^2 + \kappa^4)(R_r C_{pc}\omega_n)^2 + 4\zeta\kappa^2 (R_r C_{pc}\omega_n) + 4\zeta^2} \tag{4.32}$$

$$R_{mp} = \frac{2\zeta}{\omega_n C_{pc} (4\zeta^2 + \kappa^4)^{1/2}} \tag{4.33}$$

4.3 Modification for unimorph d_{31} mode PEH

The differences between bimorph and unimorph are number of piezoelectric layer (n_p) and distance from neutral layer to center of piezoelectric layer. The modifications are substitution of n_p to 1 and replacement of l_{np} to l_{npu} of equation (4.24), where l_n is length from bottom to the neutral layer assuming piezoelectric layer is on the top of structural layer as calculated by equation (4.25) [66].

$$l_{npu} = t_s + \frac{t_p}{2} - l_n \tag{4.34}$$

$$l_n = \frac{\frac{Y_s}{Y_{pc}}\frac{t_s^2}{2} + t_p(t_s + \frac{t_p}{2})}{\frac{Y_s}{Y_{pc}}t_s + t_p} \tag{4.35}$$

4.4 Modification for unimorph d_{33} mode PEH

Electrode area and thickness of dielectric layer determine capacitance of dielectric layer as given in equation (4.14). Geometry of dielectric layer with IDE is different with that of sandwich structured capacitor, so the capacitance cannot be calculated from the dimension of electrode. In addition, piezoelectric constant d_{33} does not relate strain and generated electric field correctly as described in literature survey chapter. Therefore, configuration of IDE was transformed to that of TBE using conformal mapping. This section summarizes Igreja and Dias's work converting IDE to equivalent TBE, i.e. ratio of electrode area and thickness of dielectric layer.

Igreja and Dias [67] investigated a mathematical model to estimate capacitance of a dielectric layer with IDE. Figure 4.3 illustrates cross section of the dielectric layer with IDE. Two capacitors were assumed between oppositely charged finger electrodes. Environment of the

capacitor is divided to two types; external and internal capacitor. Only internal capacitor was counted in this research because number of finger electrode is more than 50, so contribution from external capacitors is negligible. Conformal mapping transformed geometry of internal capacitor to geometry of TBE through four mapping steps as illustrated in figure 4.4. Repeated IDE unit was regarded as spatial wavelength $\lambda_l=2(w+g)$, and surface ratio covered by electrode as metallization ratio $l_\eta=w/(w+g)=2w/\lambda_l$. Geometry of a internal capacitor (figure 4.4 (a)) can be assigned in real and imaginary axis of *u*-plane as in figure 4.4 (b). Ratio between thickness of dielectric layer and spatial wavelength was defined as $\gamma=t_d/\lambda_l$., which determines ratio of $K(m_0')$ and $K(m_0)$ as given in equation (4.26) and (4.27). v_2 and v_3 are the Jacobi theta functions. Mapping function from *u*-plane (figure 4.4 (b)) to *v*-plane (figure 4.4 (c)) is determined by equation (4.28). $K(m_0)$ is the complete elliptic integral of first kind with modulus m_0, where $m_0'=(1-m_0)^{1/2}$. Equation (4.29) is mapping function from *v*-plane to *x*-plane. $\mathrm{sn}(v,m_0)$ is the Jacobi elliptic function of modulus m_0. The points in *x*-plane are mapped to the points in *y*-plane by equation (4.30). Final mapping step is completed by calculating k_t by equation (4.31) and the complete elliptic integral of first kind with modulus k_t and k_t'. Therefore, capacitance of the internal capacitor is calculated by equation (4.32).

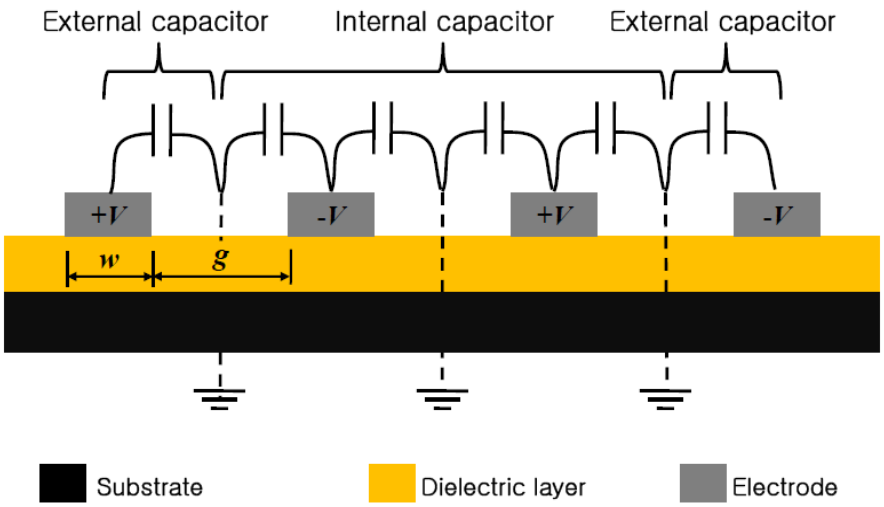

Figure 4.3 Cross section of a dielectric layer with IDE.

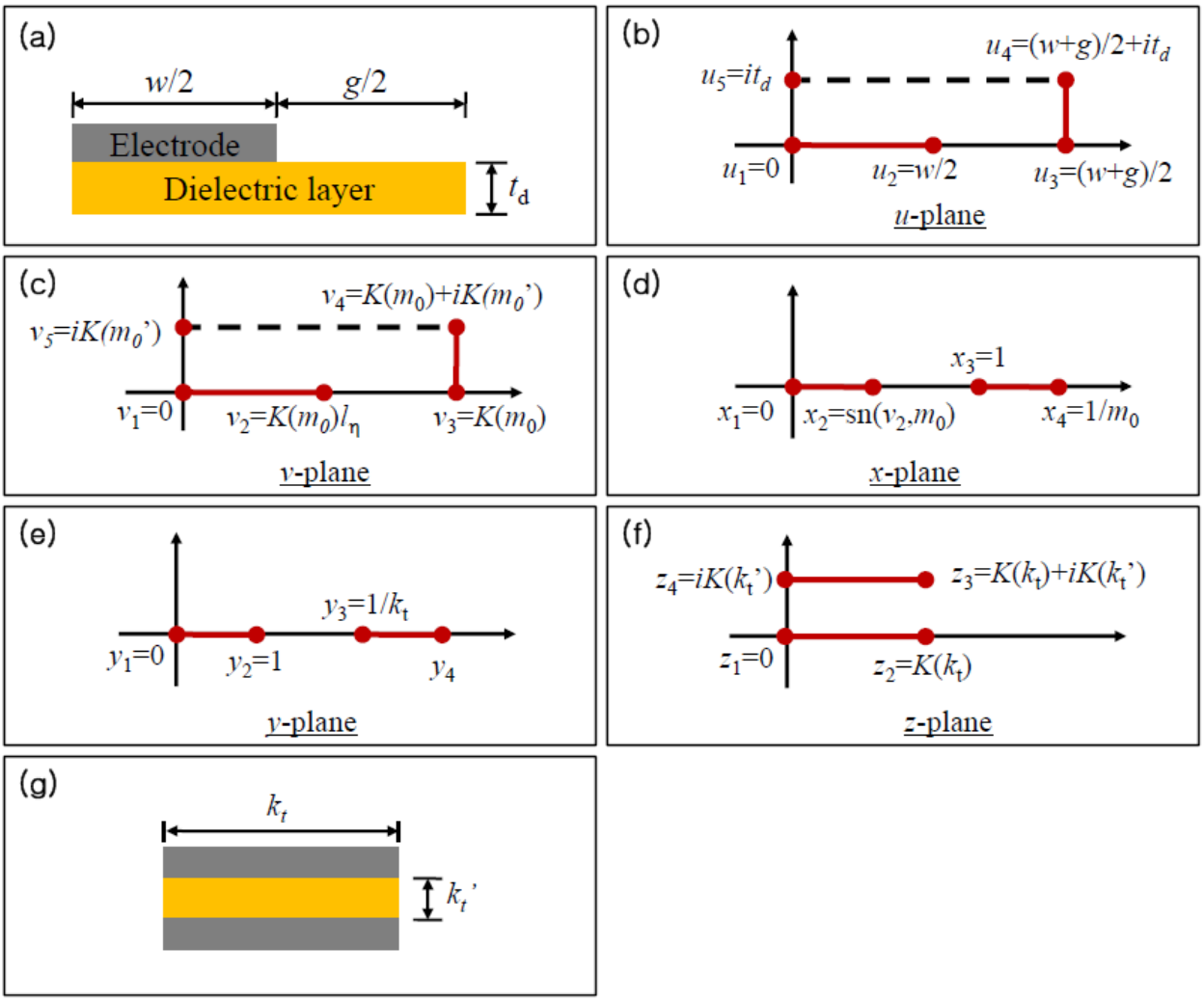

Figure 4.4 Simplified conformal mapping process. (a) An internal capacitor between finger electrode (b) Assignment of the internal capacitor to *u*-plane (c) mapping from *u*-plane to *v*-plane (d) mapping from *v*-plane to *x*-plane (e) mapping from *x*-plane to *y*-plane (f) mapping from *y*-plane to *z*-plane (g) realization of (f) to a device.

$$\exp(-4\pi\gamma) = c_1 \tag{4.36}$$

$$m_0 = \left(\frac{v_2(0,c_1)}{v_3(0,c_1)}\right)^2 \tag{4.37}$$

$$v = \frac{4K(m_0)}{\lambda_l} u \tag{4.38}$$

$$x = sn(v, m_0) \tag{4.39}$$

$$y = \frac{x}{x_2}\left(\frac{x_4^2 - x_2^2}{x_4^2 - x^2}\right)^{1/2} \tag{4.40}$$

$$k_t = x_2\left(\frac{x_4^2 - 1}{x_4^2 - x_2^2}\right)^{1/2} \tag{4.41}$$

$$C_t = \varepsilon_0 \varepsilon_r \frac{l_f K(k_f)}{K(k_f^{'})} \tag{4.42}$$

Elliptic integral of first kind ranges between 1.57 and 20.96 in equation (4.32), i.e. the conformal mapping does not result electrode area and dielectric layer thickness individually, but ratio of electrode area and dielectric layer thickness. In order to calculate the geometrical factors, coefficient F was introduced, and converted electrode area and thickness of piezoelectric layer are computed by $l_f K(k_f)F$ and $K(k_f')F$, respectively. The strain upon vibration should be identical in before and after transformation step, so the coefficient F satisfies $K(k_f')F = t_p$. Figure 4.5 illustrates capacitors as power sources (a) and conversion IDE configuration to TBE (b). The converted d_{31} mode PEH can be considered as parallel pairs of serially connected power sources as given figure 4.5 (c).

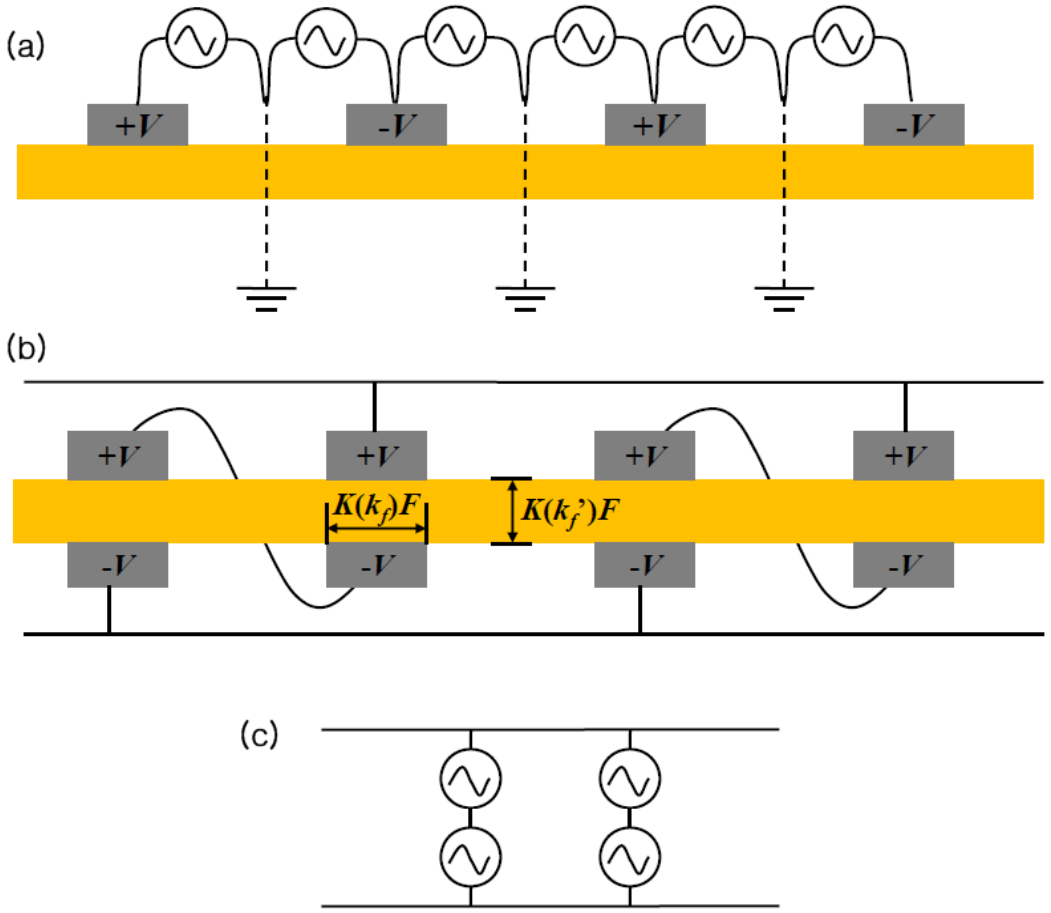

Figure 4.5 Cross section of a d_{33} mode PEH and assumption of capacitors between finger electrodes as power sources. (a) Before conformal mapping (b) after conformal mapping (only internal capacitors were illustrated) (c) simplification of transformed power sources to a circuit.

Output power equation was modified for the d_{33} mode unimorph PEH by following procedure. Since electrode area is $l_f K(k_f)F$, equation (4.33) replaces equation (4.11). Equation (4.15) and (4.16) are changed to equation (4.34) and (4.35), respectively, by changing electrode area and thickness of piezoelectric to $l_f K(k_f)F$ and $K(k_f')F$. Capacitance equation (4.14) is replaced by equation (4.32). Power from a capacitor is calculated by equation (4.36) following

similar process with the equation for the d_{31} mode PEH. Number of internal capacitor is 2(N-1), where N is number of finger electrode. Therefore, output power from the d_{33} mode unimorph PEH is calculated by equation (4.37).

$$\dot{Q}_{tc} = d_{33} Y_{pc} l_f K(k_f) \dot{\delta}_{pc} \tag{4.43}$$

$$\ddot{\delta}_{pc} = -\frac{k_s}{m_{pm}} \delta_{pc} + \frac{b_r g_f^{**}}{m_{pm}} \dot{\delta}_{pc} + \frac{k_s d_{33}}{m_{pm} K(k_f') F} V_g + g_f^{*} \ddot{z} \tag{4.44}$$

$$\dot{V}_g = -\frac{d_{33} Y_{pc} K(k_f') F}{\varepsilon_0 \varepsilon_r} \delta'_{pc} - \frac{1}{R_r C_t} V_g \tag{4.45}$$

$$P_{33p} = \frac{1}{\omega_n^2} \frac{R_r C_{pc}^2 \left(\frac{Y_{pc} d_{33} K(k_f') F g_f^{*}}{\varepsilon_0 \varepsilon_r} a_{in} \right)^2}{\left(4\zeta^2 R_r^2 C_{pc}^2 \omega_n^2 \right) \left(2\zeta_{pc} \omega_n \right)^2 + 4 \kappa^2 \left(R_r C_{pc} \omega_n \right) + 4^2} \tag{4.46}$$

$$P_{33u} = 2 P_{33p} (N - 1) \tag{4.47}$$

4.5 Equations for materials constant and resonance frequency

Materials parameters are required for output power estimation. As given equation (4.38), electromechanical coupling coefficient was calculated from antiresonant (f_a) and resonant frequency (f_r) measurement by impedance analyzer [68]. Damping ratio was obtained from amplitude measurement as given in equation (4.39). Amplitude of a cantilever is represented by output voltage when the device is vibrated at first resonance mode. Once external vibration is stopped, the output voltage decreases and the change was recorded by oscilloscope; x_1 and x_2 are adjacent amplitude during voltage decrease.

$$\kappa = \frac{\sqrt{\left(f_a^2 - f_r^2\right)}}{f_a} \tag{4.48}$$

$$\ln\left(\frac{x_1}{x_2}\right) = \frac{2\pi\varsigma}{\sqrt{1-\varsigma^2}} \tag{4.49}$$

Resonance frequency was calculated by Yi et al.'s work [63] shown in equation (4.40), where v_n is eigen value for n-th vibration mode (1.875 for the first mode), m_d is area mass density of cantilever calculated by equation (4.41), and D_p is calculated by equation (4.42). The authors used PZT and stainless steel as piezoelectric layer and substrate, respectively. Proof mass was assumed as point mass and calculation and experimental result showed reasonable agreement.

$$f_n = \frac{v_n^2}{2\pi}\frac{1}{l_c + l_{pm}}\sqrt{\frac{D_p}{m_d}} \tag{4.50}$$

$$m_d = \rho_{pc} t_{pc} + \rho_s t_s \tag{4.51}$$

$$D_p = \frac{Y_{pc}^2 t_p^4 + Y_s^2 t_s^4 + 2Y_{pc}Y_s t_{pc} t_s (2t_{pc}^2 + 2t_s^2 + 3t_{pc}t_s)}{12(Y_{pc}t_{pc} + Y_s t_s)} \tag{4.52}$$

CHAPTER 5 TEMPERATURE EFFECT ON THE PERFORMANCE OF PEH

5.1 Introduction

A PEH can be operated in diverse environmental conditions. Temperature is the most influential factor among the ambient factors because core of the PEH is piezoelectric material whose material parameters are highly temperature dependent. Especially, piezoelectric property disappears at temperature above Curie temperature, so electric energy is not generated from the PEH. Therefore, thermal effect on the performance of the PEH is essential. As described in literature survey chapter, Bedekar et al. [36] studied polycrystalline piezoelectric materials and piezoelectric single crystal under extreme temperature conditions. The authors showed that soft PZT exhibits the highest performance at room temperature, and single crystal of $YCa_4O(BO_3)_3$ and $La_3Ga_5SiO_4$ can produce stable signal at temperature higher than 500 ˚C. However, output power was three orders lower in the device employing the two single crystal piezoelectric materials than in the device using PZT. Sabat et al., Schultz et al., and Miclea et al. [37-39] studied materials' parameters of piezoelectric materials and output voltage as a function of temperature, but variation of output power and contribution of each material constant change were not investigated.

In this chapter, the performance of PEH is evaluated in terms of output power as function of temperature. The contribution of each materials parameter change is investigated through analysis of Roundy's analytical model. Two types of bulk devices were prepared based on soft and hard PZT to compare electric property change excluding mechanical property because the soft and hard PZT are characterized by doping elements from identical PZT. A MEMS scale PEH (d_{31} mode PEH of size type 2) was prepared to compared with the bulk scale

PEHs. Device fabrication process, experimental setup, and characterization procedure were covered in chapter 3. Roundy's analytical model for bimorph PEH was summarized in chapter 4.

5.2 Result and discussion

Figure 5.1 (a) shows output power of soft and hard PZT based bulk scale PEH. Both PEHs degraded as temperature increases. Hard PZT based PEH produced higher output power than soft PZT based device at room temperature. The output power is lower in hard PZT based PEH than soft based PEH at temperature higher than 80 ˚C due to faster degradation rate in hard PZT based device. The different degradation rate in the two types of devices is only dependent on electric property difference in soft and hard PZT, i.e. mechanical property difference can be excluded because the two types of PZT are made from identical PZT with different doping element; high valent doping element for soft PZT and low valent for hard PZT. Increase of the output power was observed in soft based PZT at temperature above 120 ˚C. Failure of bonding layer between shim and PZT is suspected as a cause. Strain in PZT layer might increase by slip of PZT layer due to melting of bonding layer, thus higher output power was observed.

Figure 5.1 (b) shows calculated output power by Roundy's analytical model (equation 4.22). Change of material parameters are given in figure 5.2 [69]. The calculated values have same order of output power and similar change trend as a function of temperature. The theoretical output power estimation is approximately three times of the experimental value. The deviation can be attributed to adhesion layer between shim and PZT layers, and error in damping constant and ignored nonlinear terms for simplification [38, 70].

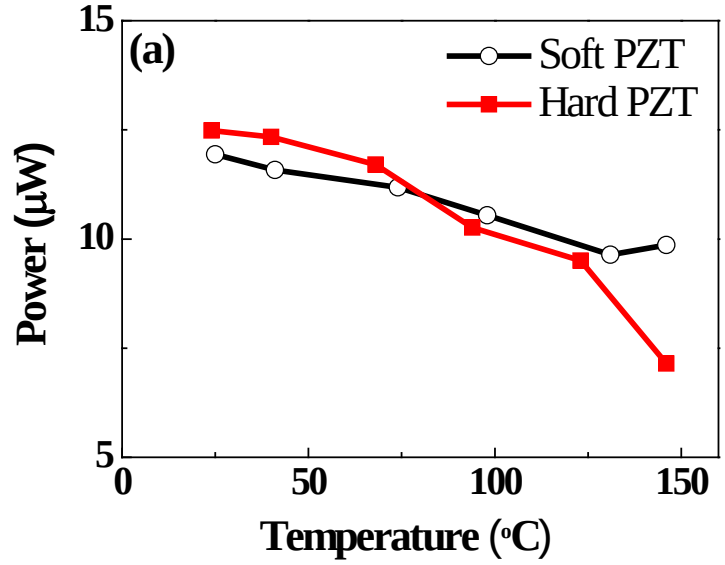
(a)
Soft PZT
Hard PZT
Power (μW)
15
10
5
0
50
100
150
Temperature (°C)

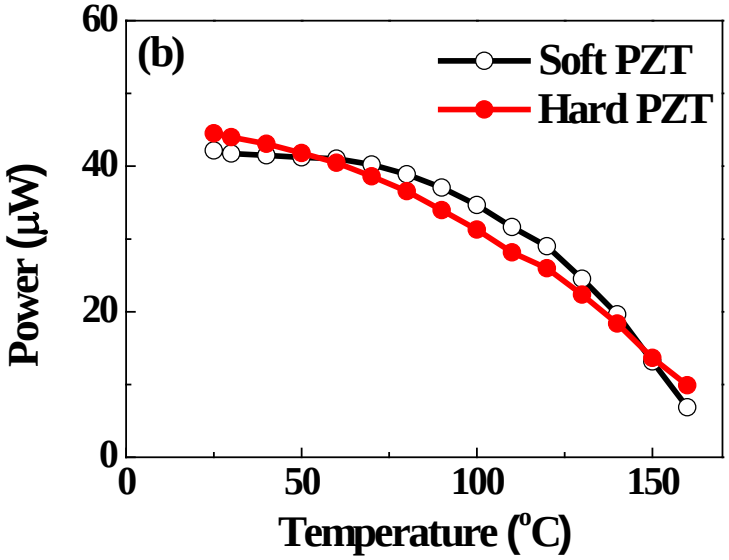
(b)
Soft PZT
Hard PZT
Power (μW)
60
40
20
0
0
50
100
150
Temperature (°C)

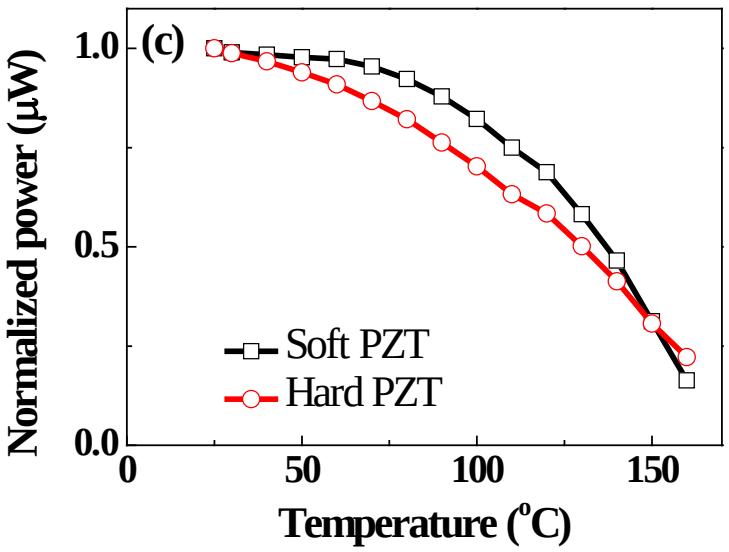

Figure 5.1 Output power from soft and hard PZT based PEH (a) in measurement (b) in calculation (c) Normalized calculated output power.

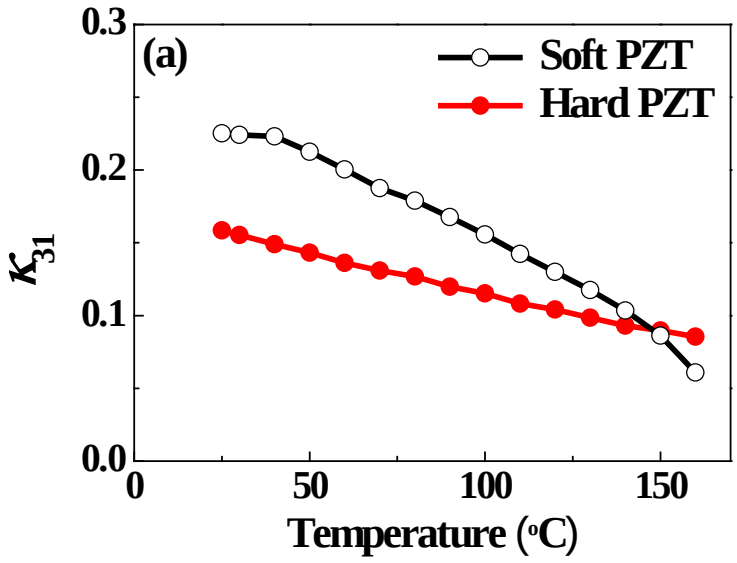

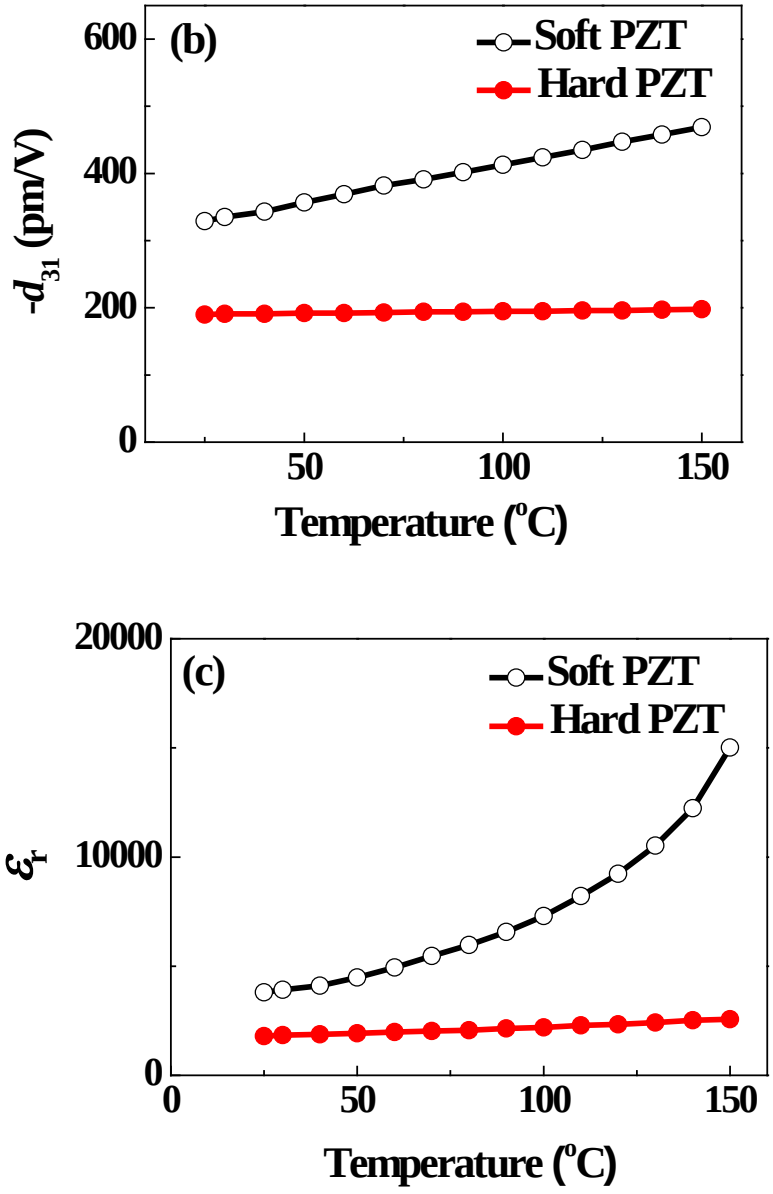

Figure 5.2 Materials parameters change as a function of temperature in soft and hard PZT. (a) Electromechanical coupling coefficient (b) piezoelectric constant (c) dielectric constant.

Measured output power is reliable at temperature between room temperature and 120 ˚C due to failure of bonding layer at temperature higher than 120 ˚C. Calculated output power was

used for analysis at temperature higher than 120 ˚C. Output power trends can be divided into two temperature range; room temperature to 100 ˚C and 100 ˚C to 150 ˚C. Degradation rate is faster in hard and soft PZT based PEH at low and high temperature range, respectively. In order to isolate temperature dependent material constant, equation (4.22) is simplified by integrating dimensional terms to constant C_0 as given in equation (5.1). Only the electromechanical coupling coefficient is different term in the soft and hard PZT based device, which proportional to piezoelectric constant and inverse of dielectric constant as given in equation (5.2). The piezoelectric constant varies linearly with temperature in both types of PZTs. The dielectric constant change in soft PZT is exponential with temperature while linear in hard PZT. Therefore, the dielectric constant variation difference can be a cause for following difference: degradation rate is slower in temperature range from room temperature to 100 ˚C and faster from 100 ˚C to 150 ˚C in soft PZT based PEH than hard PZT based device. Comparing materials constant variation in figure 5.2 (b) and (c), offsetting in material parameter variation is expected in temperature range from room temperature to 100 ˚C while the offsetting does not occur in soft PZT when temperature is higher than 100 ˚C owing to exponential increase in dielectric constant.

$$P_{B31} = C_0 \frac{1}{\omega^3} \frac{Y_c \kappa^2}{\left(4\zeta^2 + 1\right)\sqrt{4\zeta^2 + \kappa^4} + 4\zeta\kappa^2} \tag{5.53}$$

$$\kappa_{31}^2 \propto \frac{d_{31}^2}{\varepsilon_0 \varepsilon_r} \tag{5.54}$$

Different dielectric constant change trend in soft and hard PZT is attributed to mobility of dipoles. Highly mobile defect dipoles are formed by doping in hard PZT, so energy for domain switching increases. Therefore, domain and domain wall are so strongly immobile that

hard PZT is relatively insensitive to external energy [33].

Minimum output power degradation rate can be obtained by maximizing electromechanical coupling coefficient, i.e. minimum dielectric constant and maximum piezoelectric constant from analysis of equation (5.1) and (5.2). Since non-180 degree domain is responsible for piezoelectric property, and 180 degree domain for piezoelectric and dielectric property, the minimum degradation rate can be realized by followings: depinning of 180 degree domains and pinning of 180 degree domains [30, 37].

Figure 5.3 (a) shows output power variation in MEMS scale PEH as temperature increases. Output power was normalized by the value at room temperature and compared with bulk scale PEHs as given in figure 5.3 (b). Degradation rate of the MEMS scale PEH was lower than that of bulk scale PEHs. The difference should be originated from difference in PZT such as textured orientation and fine grain in PZT of MEMS scale device. PZT thin film was grown on (111) textured Pt bottom electrode and has texture and columnar structure as given figure 5.4. Motion of 180 degree domain is highly constrained by substrate in PZT grown on Pt. In addition, PZT grain is under high internal stress due to small grain size, which increases energy required for domain switching. Therefore, increase of the dielectric constant is slow with the temperature [33], thus lower degradation rate in MEMS scale PEH than bulk scale PEH. The lower thermal degradation can be achieved by using piezoelectric materials with high Curie temperature such PZT with Ti rich composition [34, 40].

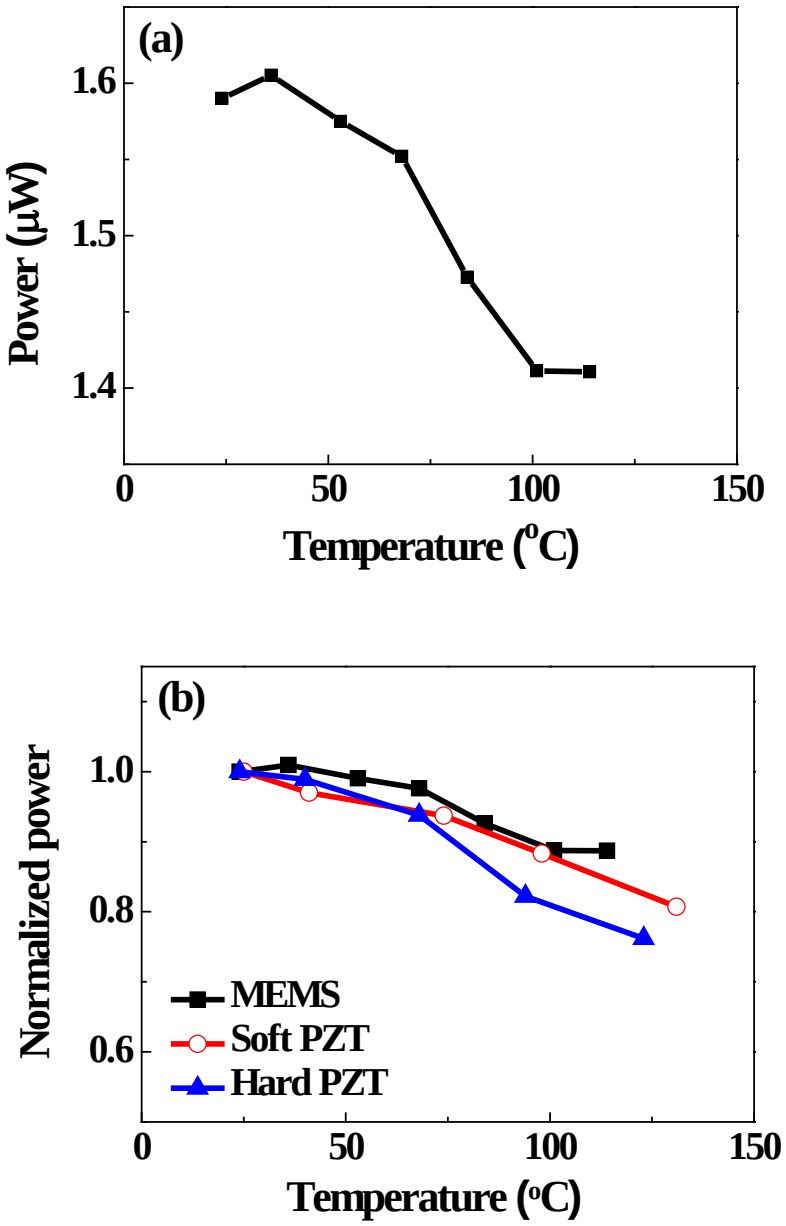

Figure 5.3 (a) Output power variation as a function of temperature in MEMS scale PEH (b) Comparison of normalized output power by the value at room temperature in two bulk scale and one MEMS scale PEH.

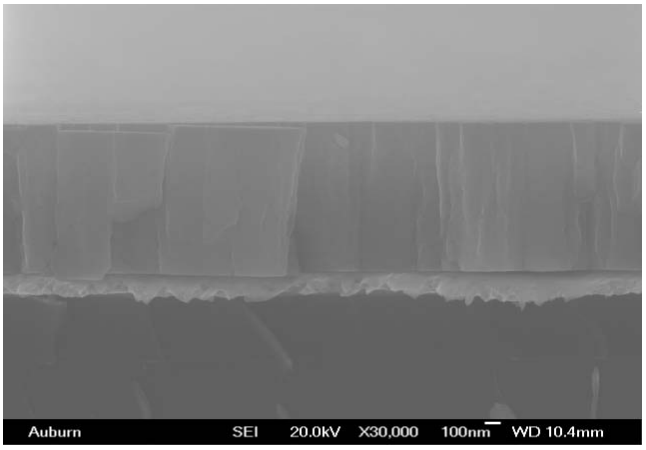

Figure 5.4 (a) Columnar structure of PZT grown on (111) textured Pt bottom electrode.

5.3 Conclusions

Output power was measured as a function of temperature in soft and hard PZT based bulk scale PEHs and MEMS scale PZT PEH. Comparing the two bulk scale PEHs, thermal degradation rate is high in hard PZT based PEH in low temperature range and in soft PZT based in high temperature range. MEMS scale PEH exhibited lower degradation rate than bulk scale PEHs. The difference between soft and hard PZT based PEH, and bulk scale PEH and MEMS scale PEH was attributed to different increasing rate in the dielectric constant with temperature. Therefore, minimum thermal degradation rate can be achieved by suppression of 180 degree domain motion with temperature because the 180 degree domain is responsible for dielectric constant.

CHAPTER 6 PIEZOELECTRIC MODE AND PERFORMANCE OF PEH

6.1 Introduction

A PEH's performance depends on electrode design because the electrode design determines piezoelectric mode, and piezoelectric constant differs in the piezoelectric modes. There are three piezoelectric modes available in the PEH; d_{33}, d_{31}, and d_{15} mode. In the most popular piezoelectric material PZT, piezoelectric constant is the highest in d_{15} mode as compared in table 2.1. However, it is not easy to realize the d_{15} mode PEH. A d_{33} mode based PEH is expected to possess two times of voltage constant g_{ij} of a d_{31} mode based one assuming identical dielectric constant in the two piezoelectric modes as calculated by equation 6.1. In addition, the d_{33} mode PEH has high potential in terms of output voltage because the output voltage is proportional to spacing between electrodes. The d_{33} mode device is constructed with IDE, whose inter-electrode spacing is larger than that of the d_{31} mode device. The spacing between electrodes is identical with thickness of the piezoelectric layer in the d_{31} mode device. In general, thickness of piezoelectric layer is less than 5 μm in a MEMS scale PEH, and finger spacing of IDE is larger than thickness of the piezoelectric layer. A PEH generates alternative current and it is converted to direct current for storage through electric circuit. The high output voltage reduces limitations and increases conversion efficiency in the rectifying circuit. The d_{31} mode based PEH has advantage in current generation because of large electrode area.

$$g_{ij} = \frac{d_{ij}}{\varepsilon_0 \varepsilon_r} \tag{6.55}$$

In the light of device fabrication, the d_{31} mode PEH has more merit than the d_{33} mode device. Piezoelectric material is formed on crystallized electrode in the d_{31} mode device while

on amorphous phase with aid of buffer layers in the d_{33} mode device. The former has more favorable condition for crystallization of piezoelectric layer than the latter. TBE of the d_{31} mode device does not require fine patterning while IDE of the d_{33} mode must be fabricated by fine patterning.

Although IDE fabrication requires fine patterning, the configuration of IDE, finger spacing and finger width, can be adjusted to control parameters for output power; i.e. output voltage and current. There are studies on output power of the d_{33} mode device, but no one organized and simulated effect of finger spacing and width on the performance of the d_{33} mode based PEH as introduced in literature survey chapter. It should be attributed to difficulties in modeling of the d_{33} mode PEH. In addition, performance of the PEH was not investigated in terms of piezoelectric mode although the two piezoelectric modes characterize output power.

This chapter verifies the theoretical modeling for d_{33} mode PEH using experimental result. Performance of the PEH is compared based on piezoelectric mode using mathematical calculation and fabricated device with identical dimension. The experimental methods were covered for device fabrication and characterization in chapter 3, and the theoretical modeling for output power estimation in chapter 4.

6.2 Output power estimation model for the d_{33} mode PEH

Mathematical equation was derived for d_{33} mode PEH output power estimation in chapter 4. This section verifies the modeling by experimental result.

6.2.1 Ferroelectric property of PZT with IDE and resonance frequency

Figure 6.1 shows polarization vs. electric field (P-E) hysteresis curve in the d_{33} mode

PEHs. P-E curve was not measured in all the devices because the wide range electric field sweep caused failure of device by electrical shortage. The P-E hysteresis loops show 200 kV/cm is reasonable strength of electric field to align electric dipoles. Saturation polarization value increases as finger spacing widens. The reason is discussed in the later of this section.

Resonance frequency of devices ranged between 243 and 249 Hz while calculated resonance frequency is 245 Hz.

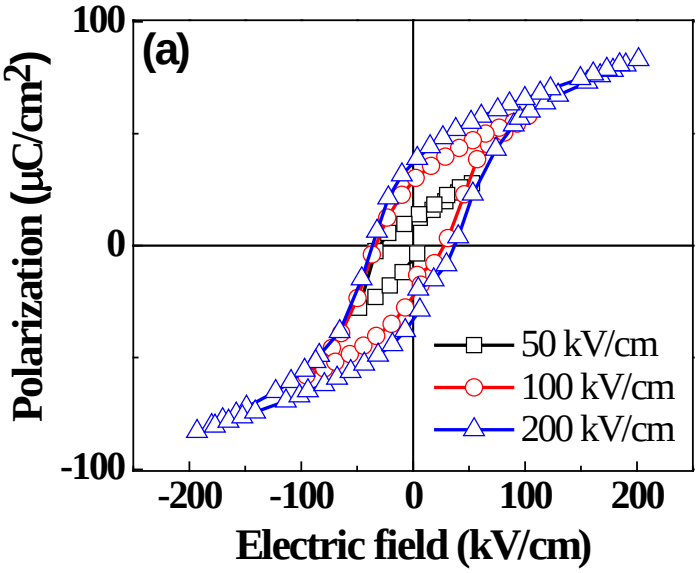

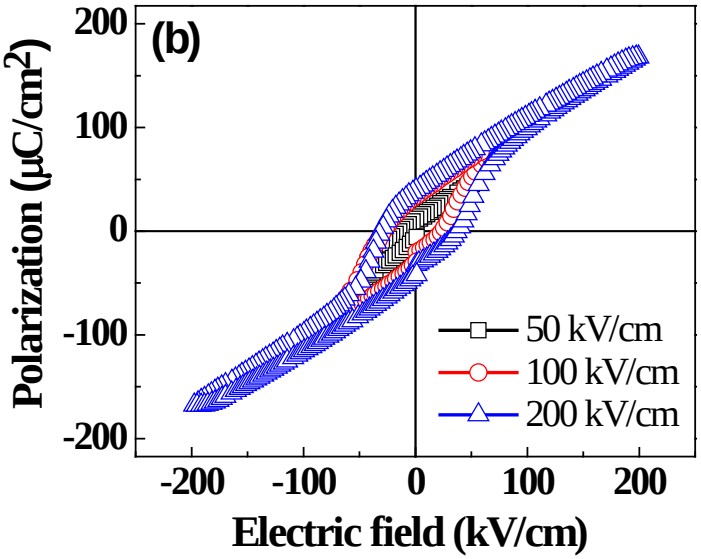

Figure 6.1 P-E hysteresis loops from the d_{33} mode devices with 16 μm finger width. Finger spacing is (a) 4 μm, and (b) 16 μm.

6.2.2 Dielectric constant in d_{33} mode devices

Dielectric constant of a piezoelectric layer was calculated from capacitance measurement, electrode area, and thickness of the layer in a sandwich structured capacitor. Since the calculation assumes straight electric field between electrodes, the principle does not cover a piezoelectric layer with IDE. Conformal mapping transforms configuration of IDE to equivalent TBE so that the dielectric constant can be calculated from capacitance measurement as described in chapter 4. In order to determine dielectric constant, capacitance was measured as function of frequency in the d_{33} mode devices with 12 μm finger width and various finger spacings as given in figure 6.2. Geometries of the IDEs were transformed to equivalent TBEs by conformal mapping as summarized in table 6.1. Capacitance was calculated assuming dielectric constant is 2500 as given in last column of table 6.1. The measurement and calculation are

compared in figure 6.3, and do not exactly match, but show reasonable agreement in value and changing trend as a function finger spacing.

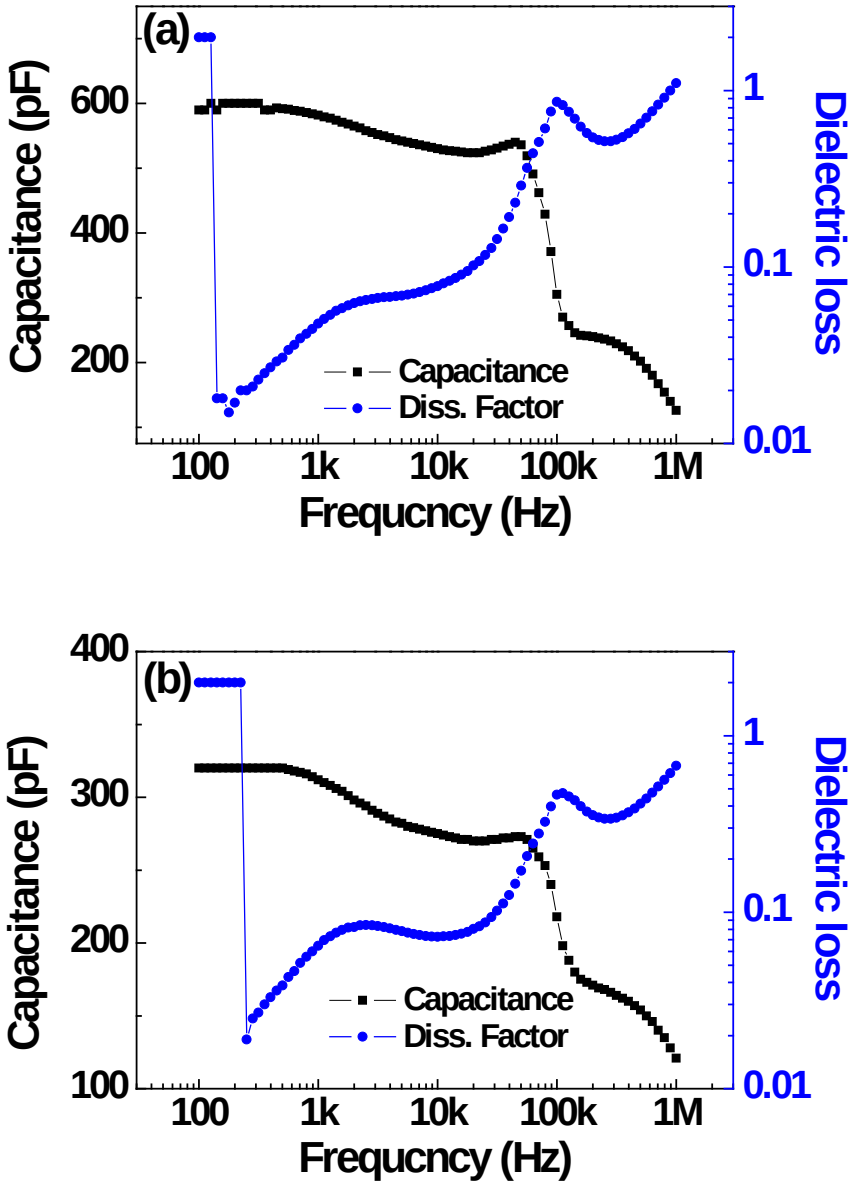

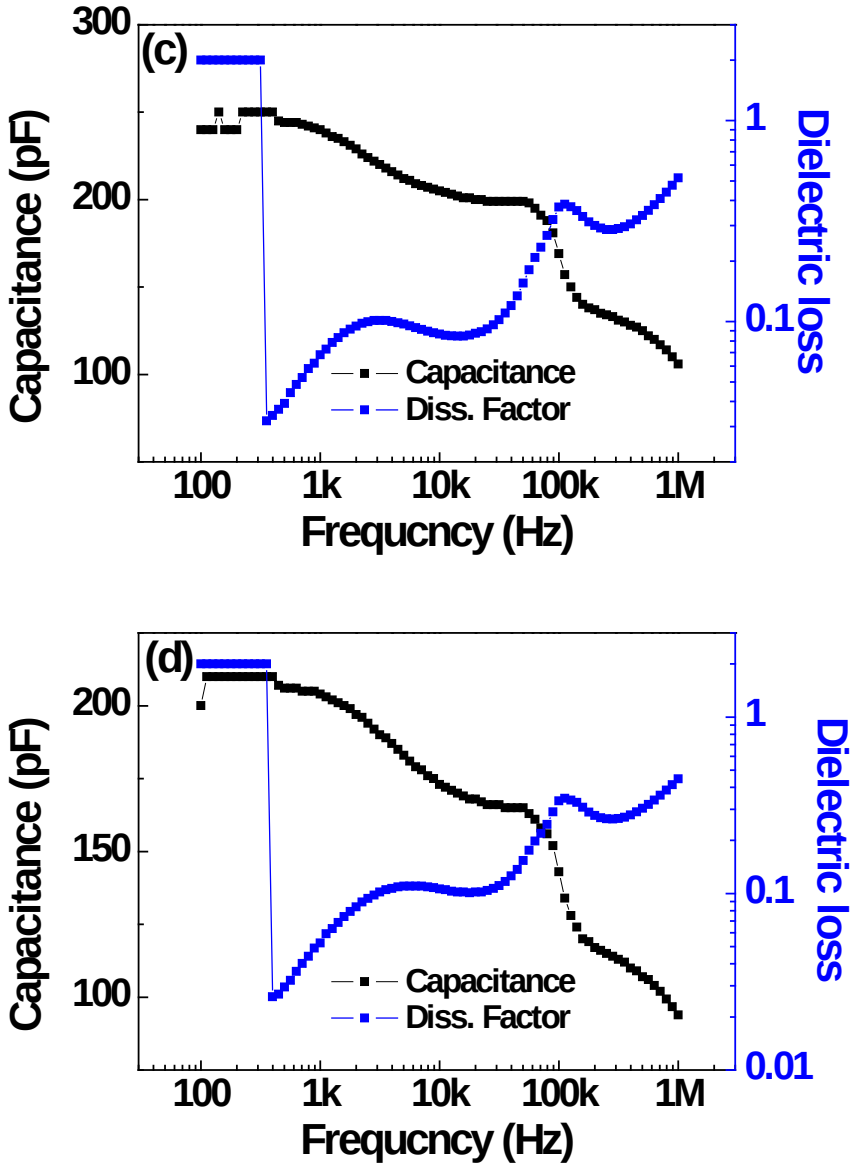

Figure 6.2 Capacitance measurements as a function of frequency in d_{33} mode PEHs with 12 μm finger width. Finger spacingsare (a) 4 μm, (b) 8 μm, (c) 12 μm, and (d) 16 μm.

Table 6.1 Calculated parameters and capacitance by conformal mapping when dielectric constant is 2500.

Finger spacing (μm)	Converted thickness (μm)	Converted width (μm)	Length of finger electrode (μm)	Number of finger electrode	Capacitance (pF, ε_r=2500)
4	1	2.43	748	187	637
8	1	4.52	736	150	270
12	1	6.54	724	125	153
16	1	7.38	712	107	114

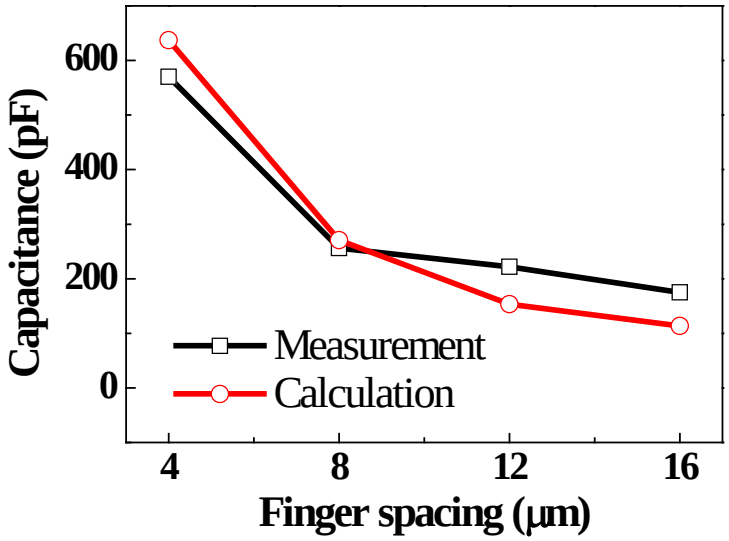

Figure 6.3 Comparison of measured and calculated capacitance assuming dielectric constant is 2500.

The dielectric constant 2500 is higher than that in thickness direction. Dielectric constant of PZT is about 1200 in out-of-plane direction, and deviation is not large in lots of studies as given in literature survey. Research on dielectric constant of PZT with IDE has not been reported. Zhang et al. [71] investigated dielectric properties of $BaSrTiO_3$ thin film with IDE using mathematical equation and fabricated samples. The dielectric permittivity was compared in in-plane and out-of-plane direction. The film with IDE exhibited more than three times of dielectric permittivity than the film with TBE. The cause for the difference was discussed as interface and grain structure. In case of the ferroelectric film with TBE, the interface between the ferroelectric thin film and the electrode possesses low dielectric constant. The $BaSrTiO_3$ thin film was grown with columnar structure, so the electric field was applied across the grain and grain boundary in the film with IDE while electric field crosses only grains. The difference in the electric field path and the interface can be applied to the dielectric constant difference in PZT based devices. Crystallographic orientation of PZT thin film may affect on the difference in dielectric constant. Figure 6.4 shows XRD patterns for the PZT in the d_{33} and d_{31} mode device. The PZTs were grown with random orientation on $PbTiO_3/ZrO_2$ seed layer and textured orientation on (111) platinum electrode. The latter was strongly influenced by textured bottom electrode, so the PZT film is under residual stress as inferred from XRD data of figure 6.4 (b). The stress was known to reduce dielectric constant of thin film PZT [72]. Jeon et al. [73] reported promotion of dielectric constant from PZT film with reduced residual stress. Taylor and Danjanovic [74] reported (111) oriented PZT may have high dielectric constant with release of residual stress. Therefore, dielectric constant 2500 is reasonable in the d_{33} mode devices.

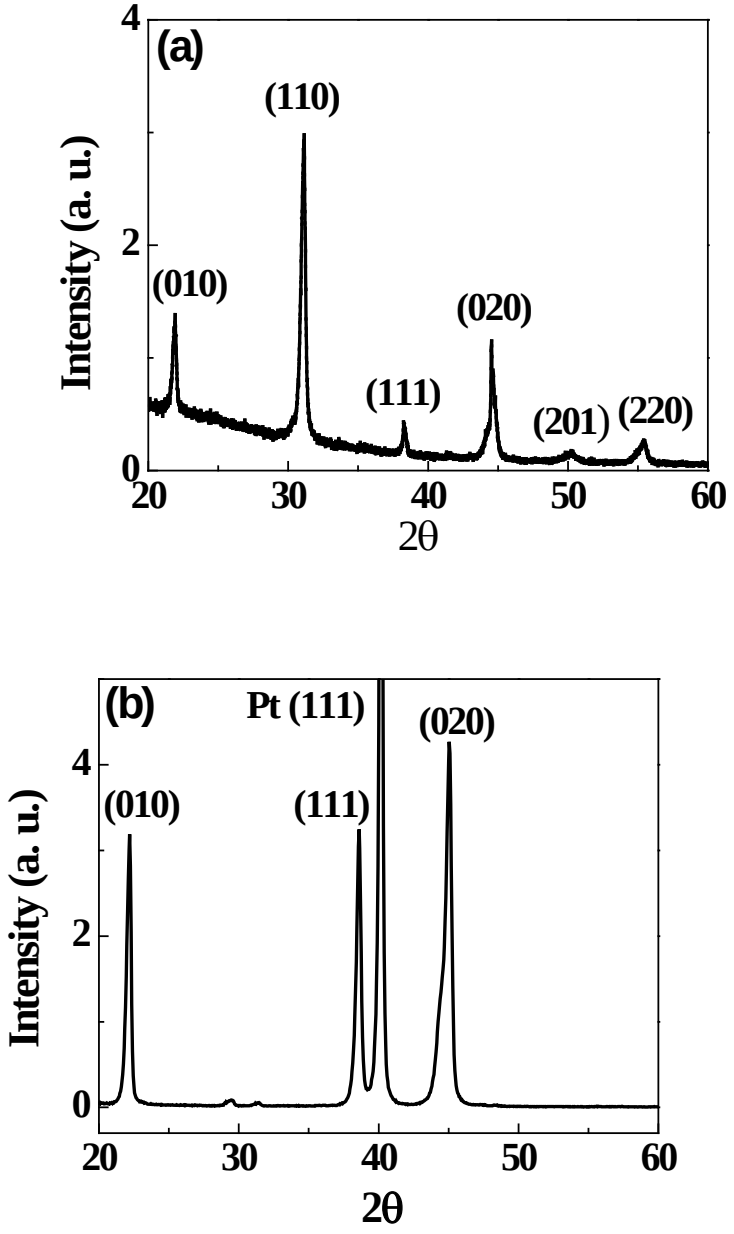

Figure 6.4 XRD patterns of PZTs in (a) ad_{33} mode device (b) ad_{31} mode device.

6.2.3 Output power in experiment and calculation

Output voltage was measured as a function of load resistance at resonance condition and output power was calculated based on the output voltage and resistance as shown in figure 6.5.

Maximum output power was regarded as output power of the device. Figure 6.6 shows output voltage of d_{33} mode PEHs with various finger widths as a function of finger spacing. The voltage does not increase linearly with finger spacing, and the cause is discussed in next subsection. Data was not recorded from two devices due to failure by electrical breakdown which was identified by current flow during poling. Finger width and finger spacing of the broken devices are 8, 4 μm, and 12, 16 μm shown as blank in figure 6.6.

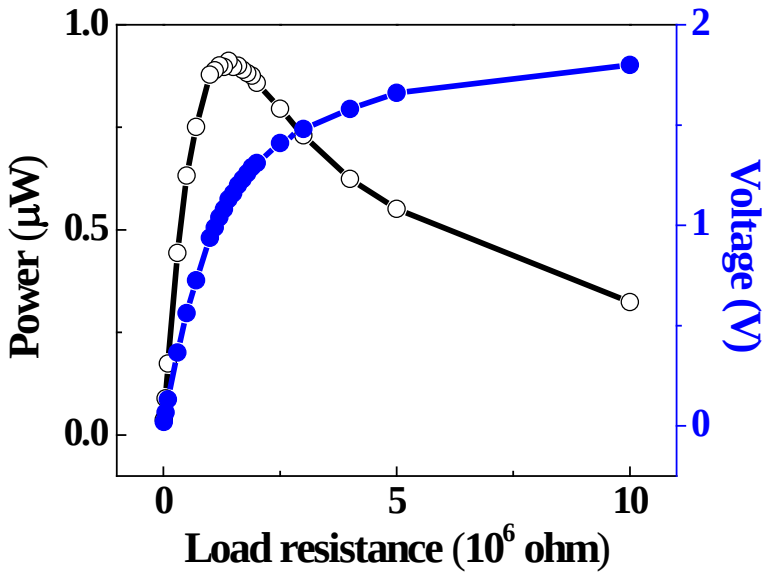

Figure 6.5 Measured output power for a d_{33} mode device. Finger electrode width and spacing are 16 and 12 μm, respectively.

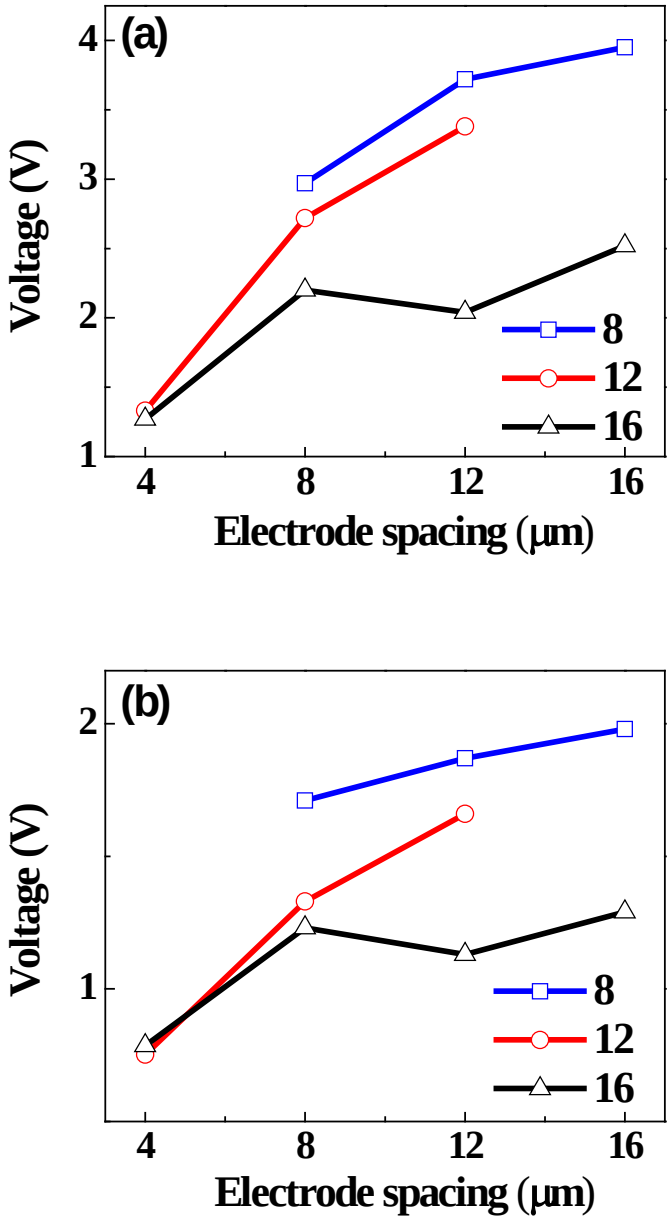

Figure 6.6 Output voltages from d_{33} mode PEHs with various finger widths as a function of finger spacing. (a) OCV (b) under optimum resistive load.

Output powers of the d_{33} mode PEHs were calculated by equation (4.37) and are compared with experimental result in table 6.2. The measured output power ranges 70 % to 85 %

of the theoretical value except for one device with 16 and 8 μm of finger width and spacing. The outlying device exhibited closer output power to calculation due to larger deflection than other devices. The larger deflection is due to non-uniform backside etching which is deduced from lower resonance frequency, 238 Hz, than the other devices. Except for the non-uniformly etched device, all the PEHs show agreement in output power value and change tendency as a function of finger spacing. Therefore, mathematical equation (4.37) is valid for estimation of output power from the d_{33} mode PEHs.

Table 6.2 Measured and calculated output power of d_{33} mode PEHs.

	Finger width (μm)					
	8		12		16	
Finger spacing (μm)	Output power (μW)					
	Measurement	Calculation	Measurement	Calculation	Measurement	Calculation
4		1.32	0.71	0.98	0.62	0.78
8	1.46	1.80	1.04	1.43	1.01	1.20
12	1.52	2.05	1.45	1.70	0.95	1.32
16	1.70	2.18		1.67	0.83	1.23

6.2.4 Discussion

The output power would increase with finger spacing based on previous output power estimation model because the report assumed that piezoelectric layer is inactive and active under finger electrode and between finger electrodes, respectively [51]. However, the output power does not increase linearly with finger spacing. Converted finger width was summarized with calculated output power as given in table 6.3 to investigate the cause for the nonlinearity in

output power variation. The converted finger width was named as effective spacing because the value corresponds to finger spacing before transformation and the space contributes for power generation. The effective spacing increases as finger spacing increases. However, the increasing rate of effective finger spacing decreases as finger spacing increase. The reduction of increasing rate is observed in output voltage variation of figure 6.6. The effective spacing is smaller than actual finger spacing and output power begins to decrease beyond certain point although effective finger spacing and output voltage increase. The reduction of output power is commonly observed when the effective spacing is less than actual finger spacing, i.e. the decrease of output power is attributed to the decreased portion of piezoelectric layer for power generation.

Table 6.3 Effective spacing and output power of d_{33} mode PEHs (calculation).

	Finger width (μm)					
	8		12		16	
Finger spacing (μm)	Effective spacing (μm)	Power (μW)	Effective spacing (μm)	Power (μW)	Effective spacing (μm)	Power (μW)
4	4.9	1.32	4.9	0.98	4.8	0.78
8	9.1	1.80	9.0	1.43	9.1	1.20
12	13.1	2.05	13.1	1.70	11.3	1.32
16	17.1	2.18	14.8	1.67	12.8	1.23
20	18.7	1.99	16.1	1.47	14.4	1.17
30	19.8	1.49	18.2	1.24	16.2	1.05
40	21.1	1.17	20.7	1.00	18.2	0.88
50	22.2	0.96	20.8	0.83	19.3	0.73

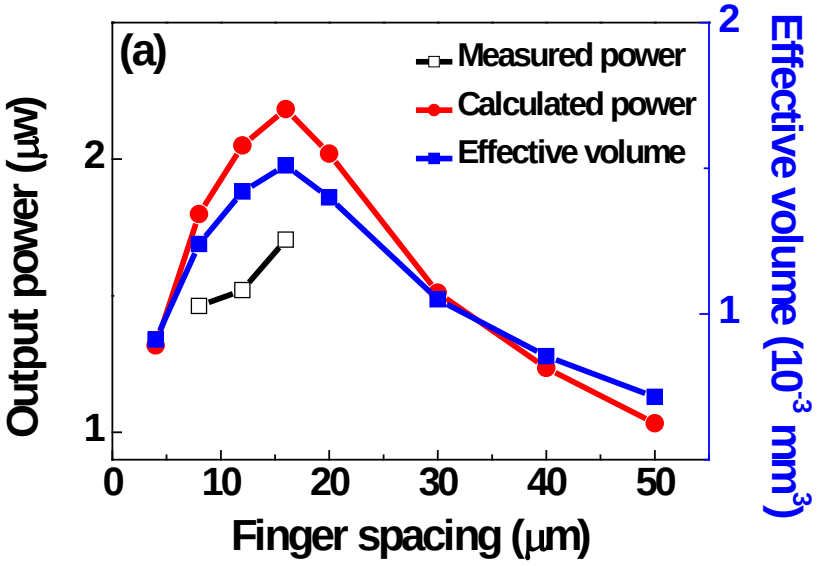
(a)
Measured power
Calculated power
Effective volume
Output power (μw)
Effective volume (10-3 mm3)
Finger spacing (μm)
0
10
20
30
40
50
1
2

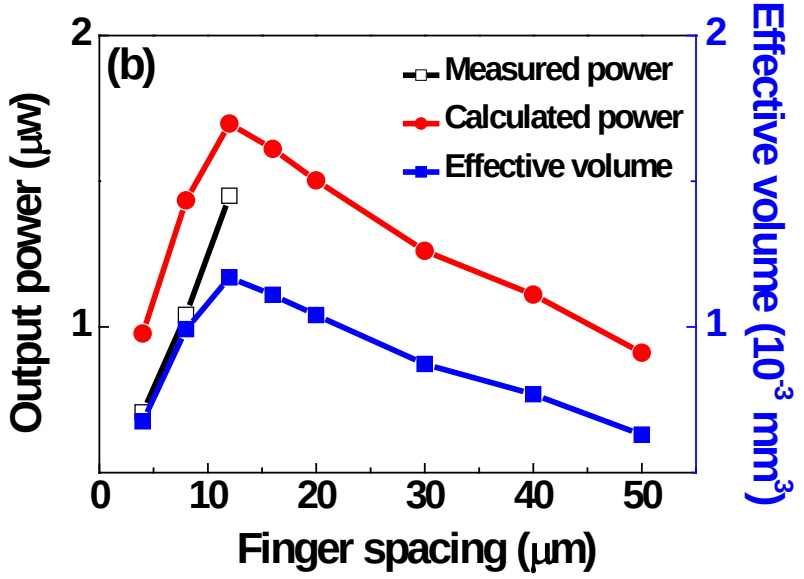
(b)
Measured power
Calculated power
Effective volume
Output power (μw)
Effective volume (10-3 mm3)
Finger spacing (μm)
0
10
20
30
40
50
1
2

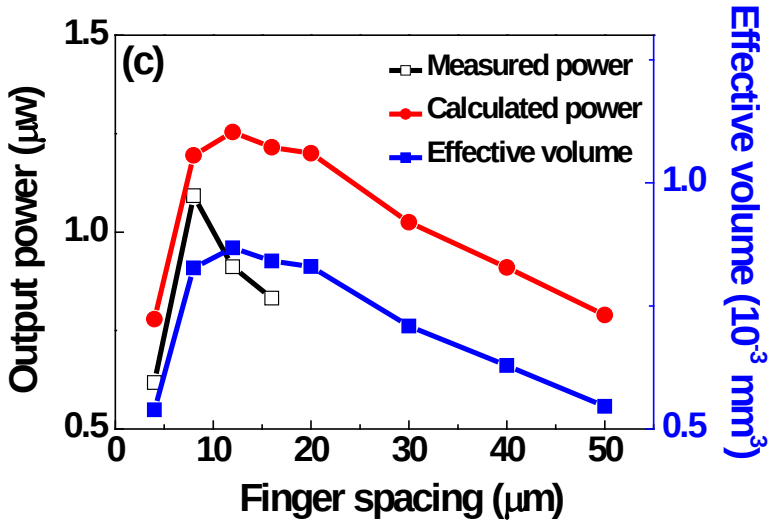

Figure 6.7 Measured output power, calculated output power, and effective volume as a function of finger spacing. Finger widths are (a) 8 μm, (b) 12 μm, and (c) 16 μm.

Dead area under the finger electrode reduces with increase of finger spacing when the area of piezoelectric layer for IDE is fixed. However, the effective finger spacing does not increase linearly with finger spacing. The effective volume was calculated to compare with measured and calculated output power as given in figure 6.7. The effective volume is volume of the piezoelectric layer contributing for power generation, calculated by number of finger (N-1), effective spacing ($2K(k_t')F$), transformed thickness ($K(k_t)F$), and length of finger (l_f) as given in equation (6.2). In the figure 6.7, output power is proportional to the effective volume. Variation of the effective volume follows that of effective spacing and number of finger electrode because the converted thickness is identical with the actual thickness of the piezoelectric layer, and length of finger electrode is fixed when the width of finger electrode is fixed. Therefore, effective spacing is determinant of output power variation.

$$V_{eff} = (N-1)\cdot K(k_t)F \cdot 2K(k_t^{'})F \cdot l_f \tag{6.56}$$

The output power of the d_{33} mode PEH is result of competition between dead layer and effective spacing in terms of IDE design. Increase of the finger spacing reduces the dead layer and increases the finger spacing when the finger width is fixed. However, ratio of the effective volume to the piezoelectric layer and output power decrease with the finger spacing when the ratio of effective spacing to actual finger spacing is less than unity. Reduction of the effective spacing is due to ineffectiveness of dc poling. Electric dipoles do not perfectly align along the electric field during the dc poling in the piezoelectric layer underneath the finger electrode [49, 75, 76], i.e. dead layer, because path for the electric field is too far to be applied through dead layer. The dead layer can be found between finger electrodes in the piezoelectric layer when the electrode spacing is larger than the effective finger spacing. The piezoelectric layer not contributing for power generation between finger electrodes can be called ineffective volume calculated by subtracting effective volume from the volume between finger electrodes, i.e. $l_f K(k_t)(g\text{-}2K(k_t'))$.

Saturation of the effective spacing and increase of the ineffective volume can be due to ineffective dc poling caused by polarization reversal and depolarizing field. Figure 6.8 illustrates three types of defects causing the ineffective dc poling; injected charges during dc poling, charged defects, and structural defects. Picture of the figure 6.8 is cross section image of PZT take by SEM in a d_{33} mode device. Surface image and cross section image are shown in figure 6.9. Charge injection occurs during the dc poling because the poling process is accompanied by charge flow and the charges are trapped around interface between PZT and electrode. Polarity of the injected charges induces internal bias opposite with aligned dipoles due to opposite direction with poling [77]. Figure 6.10 compares P-E hysteresis curves with different finger spacings in the d_{33} mode devices, 4 and 16 μm, when finger width is 16 μm. The two curves show similar

polarization value at low electric field. The polarization value differs in the two devices at high electric field range. The difference should be originated from IDE design because the two devices were made with the identical PZT and the difference is too large to be regarded as difference in dipole alignment. The ferroelectric property measurement system calculates polarization value from current flow during electric field application. The high polarization of the device with 16 μm finger gap is result of high current flow which retains charge around interface between electrode and piezoelectric material. Conduction mechanism in PZT supports charge injection. The main current source is space charge limited conduction in PZT during poling [78]. An IDE is current path during poling and has narrow contact area when finger spacing is wide, i.e. the path for current path is narrow and more charges pass through the finger electrode. Han and coworkers [79] reported larger polarization with larger electrode area on piezoelectric layer. Therefore, larger amount of charge injection occurs with wider finger spacing, which agrees with large polarization value in the device with 16 μm finger spacing. The area taken by injected charges would be within dead area if the amount of charge injection is small, but larger than dead area to invade the space between finger electrodes when large amount of charge is injected during poling, i.e. increase of ineffective volume.

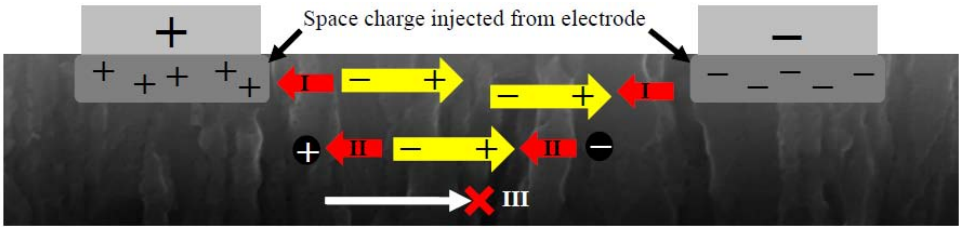

Figure 6.8 Three types of defects for ineffectiveness in dc poling. Type I: charge injection during poling, Type II: charged defects, Type III: structural defects (grain boundary).

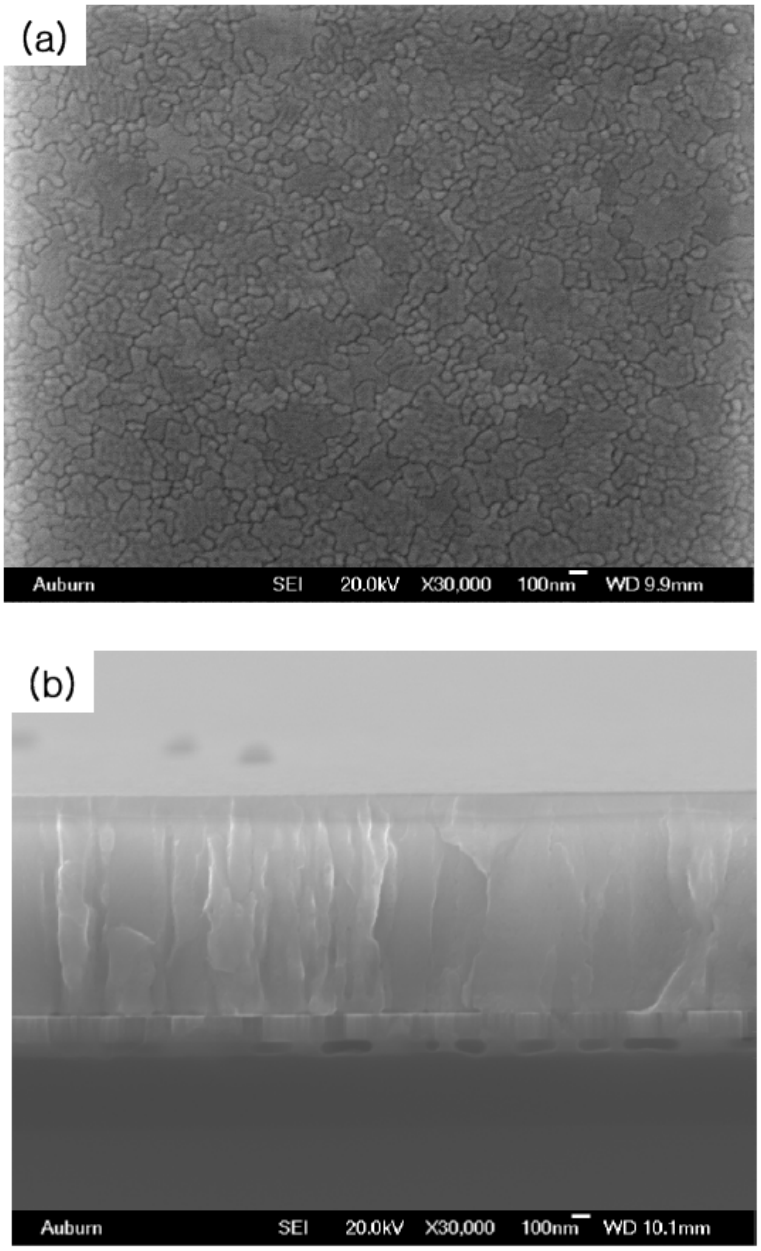

Figure 6.9 SEM image of PZT in a d_{33} mode device. (a) surface (b) cross section.

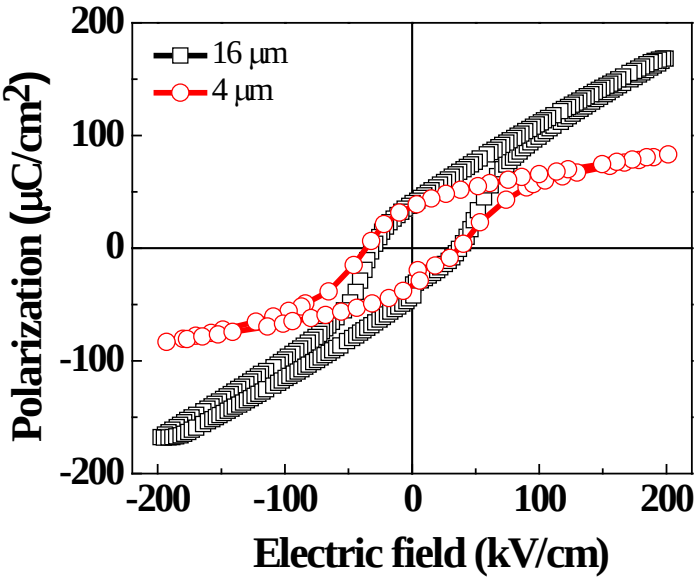

Figure 6.10 Comparison of P-E hysteresis curve from different finger spacing when finger width is 16 μm.

Type II of figure 6.8 is charged defects; grain boundaries, non-ferroelectric phases, oxygen vacancies, and interface between seed layer and PZT. In figure 6.9, the cross section and surface image show the PZT is grown with columnar structure and multi grains. Size of the grain is smaller than one micro-meter, so the electric field passes number of grain boundaries. The charged defects can immobilize the electric dipoles by pinning, which give rise inter bias for de-poling and polarization reversal [80].

Type III is obstacle for charge movement between finger electrodes. There would be more number of barriers for the mobile charges at larger finger spacing, so the poling efficiency is reduced with large finger spacing. The dipole can be pinned by interface between seed layer and PZT. The pinning effect increases with finger spacing [81].

6.3 Comparison between d_{33} and d_{31} mode based PEH

Figure 6.4 compares structural property of PZTs in a d_{33} and a d_{31} mode PEH. The PZT was grown with texture in the latter due to influence of Pt seed layer which is highly (111) oriented while grown with random orientation in the former although $PbTiO_3$ was deposited as a seed layer.

Table 6.4 compares material parameters of the PZTs and device constant in the d_{33} and d_{31} mode PEH. Young's modulus was measured by nanoindentation [82]. Damping ratio was calculated by equation (4.39) using experimental data. Dielectric constant was determined from capacitance measurement as described in previous section. Piezoelectric constant was found in previous studies [83-86]. Electromechanical coupling coefficient was calculated by equation (4.38).

Table 6.4 Comparison of material parameters of PZT in the d_{33} and d_{31} mode devices.

	d_{33}	d_{31}
Young's modulus (GPa)	150	
Damping ratio	0.00109	0.00103
Dielectric constant	2500	1250
Piezoelectric constant (pC/N)	100	-55
Electromechanical coupiling coefficient (%)	5.8	6.3

Figure 6.11 shows P-E hysteresis loop of PZT in a d_{31} mode device. Comparing the graphs with that in the d_{33} mode PEH of figure 6.10, both type of PZTs show saturation at 200 kV/cm and polarization is much higher in the d_{33} mode device. The difference in polarization can be attributed to difference in electrode area as there is large difference in polarization in the d_{33} mode device. The electrode area is much larger in a PEH with TBE than with IDE. A P-E hysteresis property characterization system calculates polarization value from current flow during electric field application. The larger leakage current might pass through with smaller electrode, thus higher polarization, which corresponds with Han's report [79].

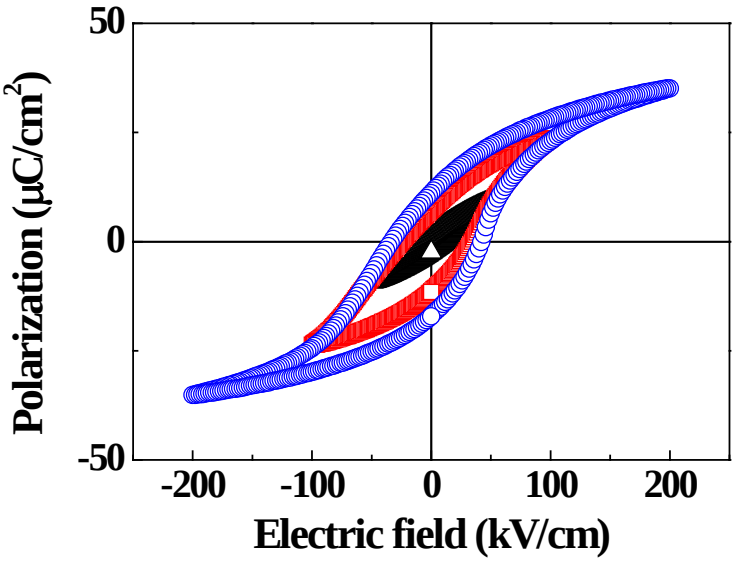

Figure 6.11 P-E hysteresis curve of PZT in d_{31} mode PEH.

Output power of the d_{31} mode device was characterized at 0.5 g vibration as a function of resistive load as shown in figure 6.12. Since electrode configuration does not change once dimension of the cantilever is determined in the d_{31} mode device, output power is fixed with

determined size of cantilever. Estimated output power of the d_{31} mode PEH is 2.33 μW, and measured is 2.15 μW (92.3 % of calculated value). Optimum resistance for maximum output power is 9.88 kilo-ohm. Output power of the d_{33} mode devices ranged between 0.62 and 1.71 μW (75 ~ 80 % of calculated output power) with optimum resistance between 80 kilo- to 1 mega-ohm in the d_{33} mode PEHs. The matching load resistance is much higher in the d_{33} mode devices, which should be due to wider electrode spacings in the d_{33} mode devices. Measured output power of the d_{33} mode devices deviates from computed value more than that of the d_{31} mode device. The deviation is partially attributed to error in piezoelectric constant. Piezoelectric constant d_{31} has been frequently reported using identical geometrical relationship between strain and electric field with d_{31} mode device [83, 85]. The d_{33} was measured in thickness direction [86] while strain and electric field are in in-plane direction in a the d_{33} mode PEH. Therefore, the piezoelectric electric constant d_{33} in literature might not correctly correlate stain and electric field in the d_{33} mode device. However, the modeling for d_{33} mode device is valid for output power estimation although there is difference in calculation and measurement because the deviation is acceptable range. Output voltage ranges 750 mV to 1.98 V at maximum output power in the d_{33} mode device while is less than 350 mV even at open circuit in the d_{31} mode device. The difference is discussed in the later of this section.

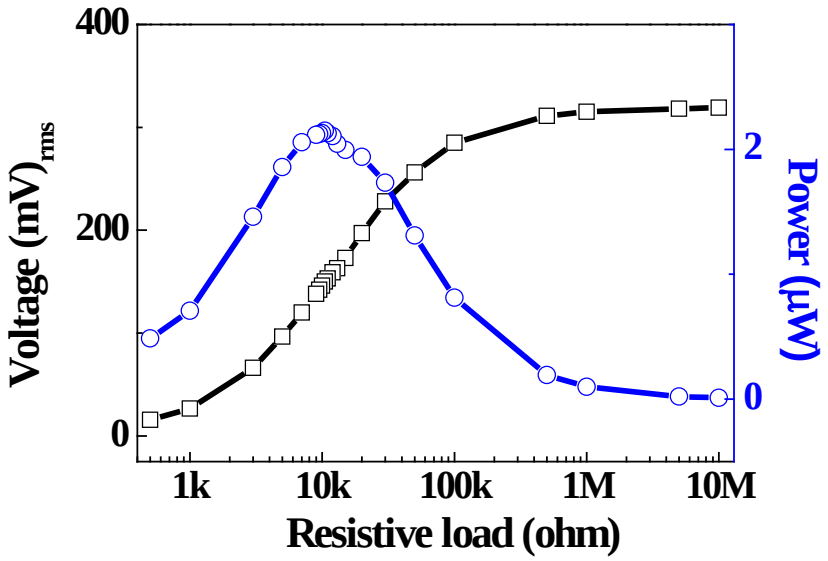

Figure 6.12 Measured output power in the d_{31} mode device.

Output power was increased with reduction of finger electrode width in the figure 6.7. Improved output power is due to decreased dead layer with reduced finger width. Equation (4.37) calculates output power of the d_{33} mode PEHs with narrow finger width (2 and 4 μm) to find IDE configuration exceeding the output power of the d_{31} mode PEH as given in figure 6.13. The plotted output power of the d_{33} mode device is 75 % of calculated power in figure 6.13. A d_{33} mode PEH can produce higher power than d_{31} mode PEH when finger electrode width is 2 μm and finger spacing is between 8 and 20 μm. The estimation does not consider failure during dc poling, so higher output in the d_{33} mode device than the d_{31} mode device is more feasible when finger spacing is 8 μm than is 20 μm.

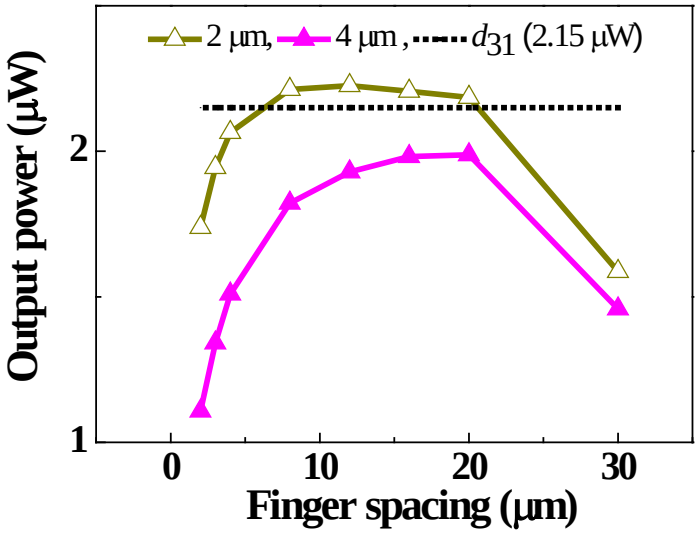

Figure 6.13 Calculated output power of the d_{33} mode devices with narrow finger electrode width (2 and 4 μm, solid lines) and comparison with the d_{31} mode device (dotted line).

Output voltage is higher in the d_{33} mode devices than the d_{31} mode device in figure 6.13. There are two factors determining output voltage; piezoelectric voltage constant and spacing between electrodes. Piezoelectric voltage constant g_{33} can be expected to be higher than two times of g_{31} by equation (6.1) assuming identical dielectric constant in the PZTs of the d_{33} and d_{31} mode device. However, g_{33} and g_{31} are 0.00452 and 0.00497, respectively. The similarity in piezoelectric voltage constant is attributed to two times higher dielectric constant in PZT of the d_{33} mode PEH than that of the d_{31} mode device. Therefore, electrode spacing results difference in output voltage of the d_{33} and d_{31} mode device. Figure 6.14 compares OCV at identical electrode spacing in d_{33} and d_{31} mode devices. OCV of the d_{31} mode device was multiplied by finger spacing of the d_{33} mode devices (4 to 16) for identical electrode gap. Figure 6.14 shows similar voltage at identical electrode spacing, which indicates determinant of the output voltage

of the PZT based PEH is electrode spacing rather than piezoelectric voltage constant.

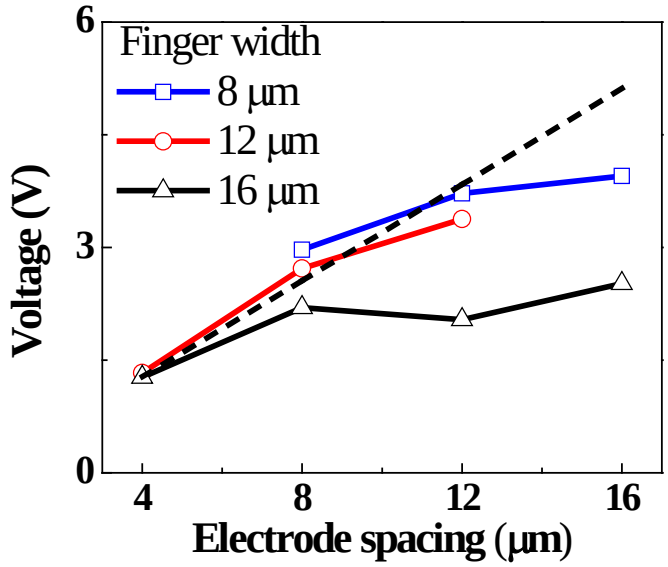

Figure 6.14 Comparison of OCV at identical electrode spacing in the d_{33} and d_{31} mode devices. Electrode spacing is 1 μm in the d_{31} mode device. OCV of the d_{31} mode device is multiplied by finger spacing of the d_{33} mode devices (4 to 16). Solid represents output voltage of the d_{33} mode device. Dotted line denotes multiplied output voltage of the d_{31} mode device.

Table 6.5 compares geometrical parameters in a d_{33} and a d_{31} mode device. The d_{33} mode device possesses 2 μm finger width and 12 μm finger spacing, which exhibits higher power than the d_{31} mode device. Electrode spacing is physical distance between fingers. Electrode area and volume of piezoelectric layer were calculated by conformal mapping. The d_{33} mode PEH can exhibit superior performance to the d_{31} mode PEH although volume of piezoelectric layer is always larger in the latter due to dead layer of the former. The higher performance of the d_{33} mode device than the d_{31} mode device is because the output power is

product of voltage and current, where the voltage proportional to electrode spacing and current to electrode area. Therefore, one of the biggest advantage of the d_{33} mode PEH to the d_{31} mode device is in electrode design, i.e. IDE, because output voltage and current are controlled by finger width and spacing.

Table 6.5 Geometry comparison for the d_{33} and d_{31} mode device. Finger width and spacing of IDE are 2 and 12 μm in the d_{33} mode device, respectively. Electrode area and output power of the d_{33} mode device are calculated value.

	d_{33}	d_{31}
Electrode gap (μm)	12	1
Electrode area (mm^2)	0.154	2.88
Volume of piezoelectric layer (mm^3)	0.00205	0.00288
Output power (μW)	2.23*	2.15
Power density ($\mu W g^{-2} mm^{-3}$)	8.39	8.09

* 75 % of calculated value

A PEH is typically equipped a rectifying circuit to transform produced ac to dc for storage. The circuit consists of diodes activated at voltage higher than threshold voltage. In case of the d_{33} mode PEH, there would be less limitation and loss in the diodes due to high output voltage. Therefore, the d_{33} mode device provides higher tolerance than the d_{31} mode device in the light of device applications. On the contrary, the d_{31} mode PEH is more advantageous than the d_{33} mode PEH in device fabrication because of simple structure of TBE and requirement of

fine pattering in IDE.

6.4 Conclusions

PEHs were designed and fabricated with the d_{33} and d_{31} mode in identical MEMS scale to compare the effect of piezoelectric mode on the performance of the PEH. A mathematical model was derived to estimate and analyze output power of the d_{33} mode PEH.

The theoretical modeling was validated by comparing experimental result and calculated output power in value and changing trend as function of finger width and finger spacing. The equation criticizes previous output power model expecting linear increase of output power with finger spacing. The measurement and calculation showed decrease of output power when finger spacing exceeds effective finger spacing. As finger spacing increases, dead layer underneath finger electrode reduces and the volume of piezoelectric layer contributing for power generation saturates. Ineffectiveness of poling by de-poling and polarization reversal was discussed as a cause of effective volume saturation. There may be larger amount of charge injection and charged defects with wider finger spacing. Therefore, the maximum output power of the d_{33} mode PEH can be achieved when finger spacing/effective spacing is unity.

The d_{31} mode device produced higher power than the d_{33} mode devices in fabricated devices. The characteristics of power generation were analyzed by mathematical equations. Determinant of voltage difference in the d_{33} and d_{31} mode device is spacing between electrodes rather than piezoelectric voltage constant. Therefore, electrode design is dominant factor for output power of the PEH. IDE configuration was found to produce higher power from the d_{33} mode PEH than from the d_{31} mode PEH. In practical applications, the d_{33} mode PEH with appropriate IDE configuration is superior to the d_{31} mode PEH due to high output power and

voltage. In the view of device fabrication, the d_{31} mode is more suitable due to simple structure.

CHAPTER 7 PEH WITH WIDEBAND

7.1 Introduction

One of the most serious demerits of a PEH converting mechanical energy to electric energy is narrow working frequency range. Various structures were proposed to widen band width using movable cantilever, stopper of cantilever, a cantilever with two degree of freedom, and nonlinear cantilever as summarized in table 2.3. Roundy summarized frequency of vibration sources from ambient and the frequency ranges from 60 to 240 Hz [7, 8]. There is no device covering the frequency range although frequency was fairly extended by the various approaches.

Piezoelectric property was combined with magnetic property using multiferroic materials and composite of ferroelectric-ferromagnetic materials. Working frequency was extended in the energy harvester employing multiferroic material, but the device was based on array of cantilever with various length [87]. Magnetoelastic material was deposited on piezoelectric material to induce strain from magnetic field [88]. The strain mediation by magnetic field may not be sufficient because there is limitation in magnetic material deposition which should be amorphous phase.

In this chapter, a PEH demonstrates vibration energy harvesting in almost entire frequency range available from surroundings. The PEH is based on magnetic substrate to be effectively actuated by magnetic field. ZnO was used as a piezoelectric material. In order to preserve magnetic property of the substrate, all the fabrication processes were performed at room temperature except for photoresist baking. Cu was doped in ZnO to improve electrical property of ZnO on amorphous phase substrate as described in chapter 3.

7.2 Electric property of Cu doped ZnO

In order to increase electric resistivity, Cu was doped in ZnO. Figure 7.1 shows resistivity change as a function of Cu sputtering power. The electric property was characterized with 0.5 mm x 0.5 mm sized electrode before device fabrication. Doping concentration was not measured by an EDS (Energy-Dispersive x-ray Spectroscopy) due to limitation of the system, so the doping power represents difference in Cu concentration. As fabricated un-doped ZnO is naturally n-type semiconductor due to defects such as oxygen vacancies and Zn interstitials. In-situ and post heat treatment have been performed to reduce electrical conductivity in ZnO [89-92]. In this research, undoped ZnO exhibited low resistivity and as given in the figure 7.1. Resistivity was increased by Cu doping and is maximum at 1 W Cu doping. The electrical property improvement may be due to reduced negative carrier by recombination. Cu oxide, CuO and Cu_2O, provided positive carrier because vacant 3d shell of Cu ion provide positive charge, i.e. p-type doping. Cu_2O exhibited p-type semiconducting property mainly due to Cu vacancies [93]. Wang [94, 95] investigated electric property of Cu doped ZnO for electric resistivity and piezoelectric property improvement, and reported divalent Cu ions possess positive charges and recombine with negative charges. Decreased resistivity at 3 and 5W Cu doping may be attributed to limited solubility of Cu in ZnO matrix because metallic Cu and Cu ion in interstitial site can contribute to electric conduction [96, 97]. Metallic Cu is more stable than Cu ion with excessive Cu doping. Therefore, c-axis preferred growth is disturbed and resistivity reduced.

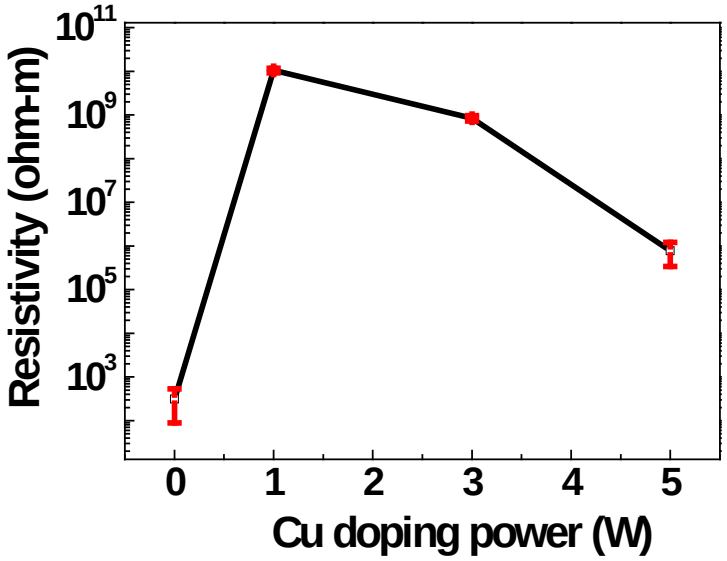

Figure 7.1 Resistivity change in Cu doped ZnO. Red line indicates error bar.

Figure 7.2 compares dielectric constant and dielectric loss as a function of frequency. Amplitude of the ac electric field is 100 mV. The pure and 5W Cu doped ZnO showed too small and too high dielectric constant due to electrical leakage. The 1W and 3W Cu doped ZnO exhibited dielectric behavior. Reasonable dielectric constant was not measured in low frequency range, which might be due to limitation in sensitivity of the instrument. Table 7.1 summarizes dielectric constant and loss of 1W and 3W Cu doped ZnO. 1W Cu doped ZnO showed higher dielectric constant and lower dielectric loss than 3W Cu doped ZnO, and it corresponds with electric resistivity measurement. Excessive positive carrier doping may be responsible for the dielectric loss in 3 W Cu doped ZnO. It is elaborated in next subsection.

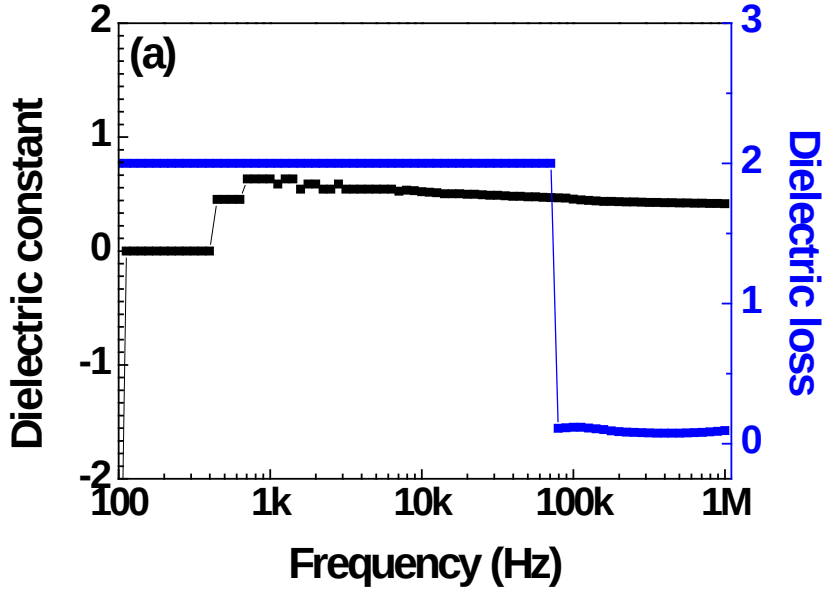
(a)
Dielectric constant
Dielectric loss
Frequency (Hz)
2
1
0
-1
-2
3
2
1
0
100
1k
10k
100k
1M

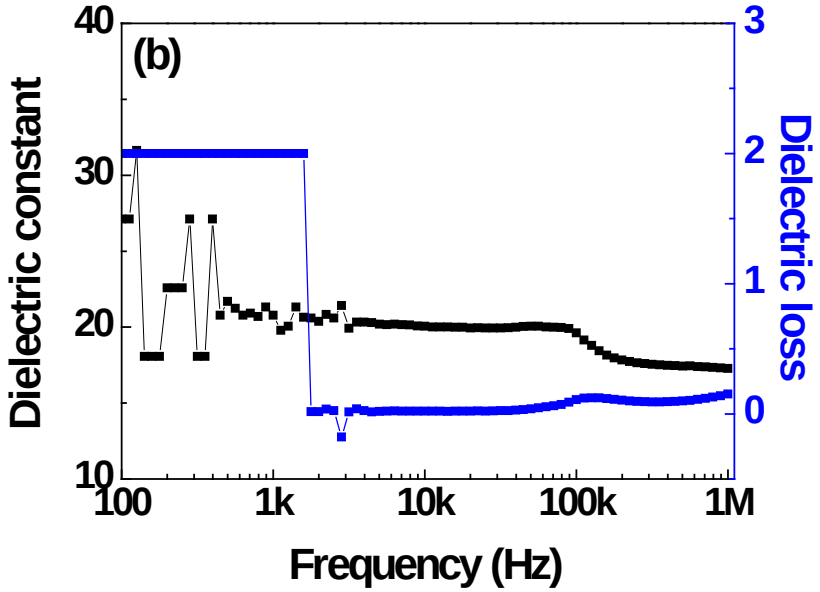
(b)
Dielectric constant
Dielectric loss
Frequency (Hz)
40
30
20
10
3
2
1
0
100
1k
10k
100k
1M

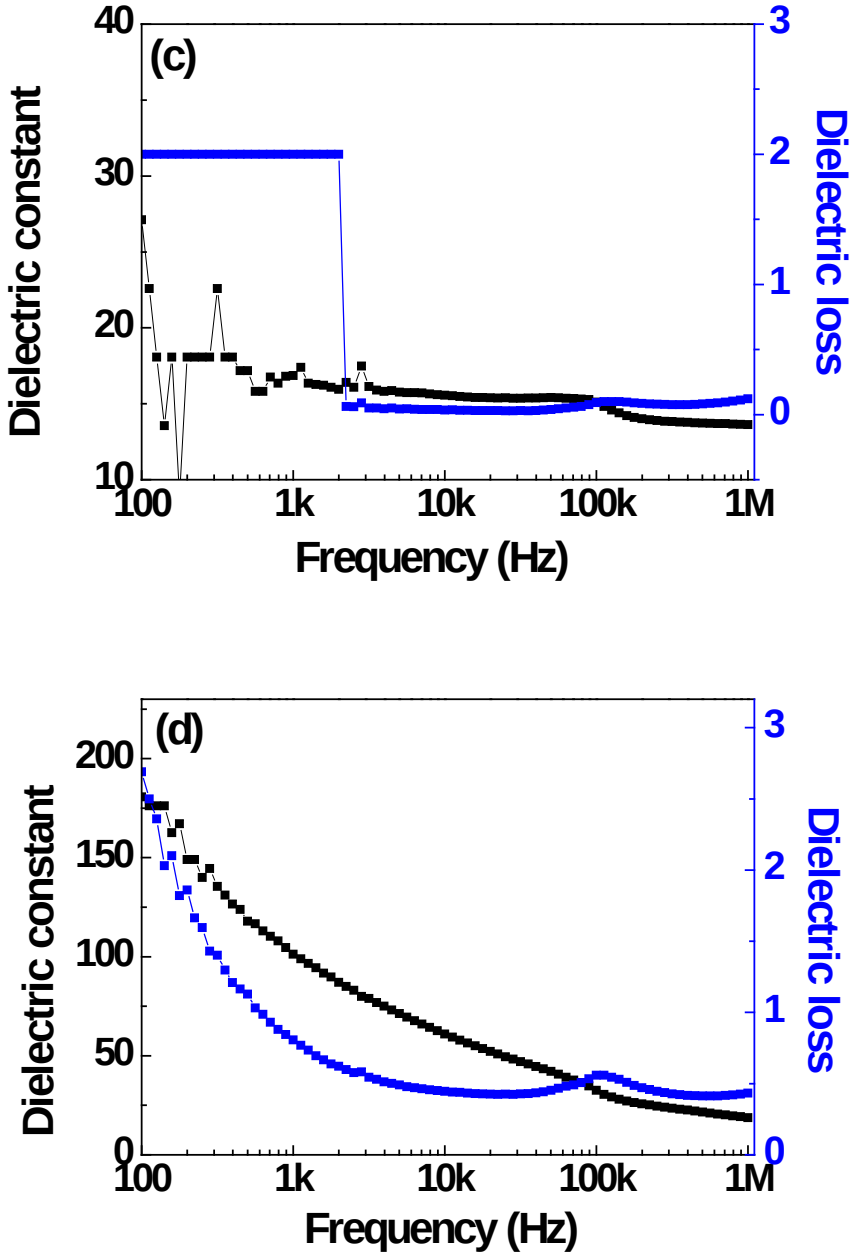

Figure 7.2 Dielectric constant and dielectric loss as a function of frequency. (a) Pure ZnO (b) 1 W Cu doped ZnO (c) 3 W Cu doped ZnO (d) 5 W Cu doped ZnO.

Table 7.1 Dielectric constant and loss of 1W and 3W Cu doped ZnO at 10 kHz.

	1W Cu doping	3W Cu doping
Dielectric constant	20	15.6
Dielectric loss (%)	2.1	3.5

7.3 Performance of device

Cantilever devices were fabricated with Metglas substrate to evaluate performance of the devices. The devices were vibrated on a shaker at 1 g (g=9.8 m/s^2) vibration. Output power was measured in two devices with 1 W and 3 W Cu doped ZnO as presented in figure 7.4. Cantilevers with pure and 5 W Cu doped ZnO did not produce output power due to low electric resistivity. Maximum output power was observed from 1 W Cu doped ZnO cantilever, and 3 W Cu doped device generated two orders lower output power than 1 W Cu doped ZnO cantilever. It might be due to higher dielectric loss in the 3 W Cu doped ZnO than the 1 W Cu doped ZnO.

In order to check origin of the output power difference from the two devices, electric property was measured in device scale. Table 7.2 shows electric property at dc electric field application. Higher resistivity was observed in 1 W doped ZnO than in 3 W Cu doped ZnO. Figure 7.6 is response upon ac field application. Since operation frequency range is lower than 1 kHz, dielectric loss was compared at frequency lower than 10 kHz. Dielectric loss of the 1 W Cu doped ZnO cantilever was lower than 10 % at frequency up to 1 kHz. That of the 3 W Cu doped ZnO device ranged between 20 and 10 %. Output power generation from PEH is similar to the ac electric field application. Therefore, the origin of the different output power from the 1 W and the 3 W Cu doped ZnO device can be attributed to dielectric loss difference, i.e. generated

charge was dissipated due to dielectric, ionic relaxation or conduction electrons in 3 W Cu doped device.

Excessive Cu doping might be responsible for the reduced resistivity at dc electric field application and higher dielectric loss at ac electric field application in the 3 and 5 W Cu doped ZnO than the 1 W Cu doped ZnO. Acceptor level of Cu ion in ZnO is too high to be activated, so it can be assumed as a bound positive charge [69, 98]. However, excessive Cu doping may form metallic Cu at interstitial site, so that it might participate in conduction.

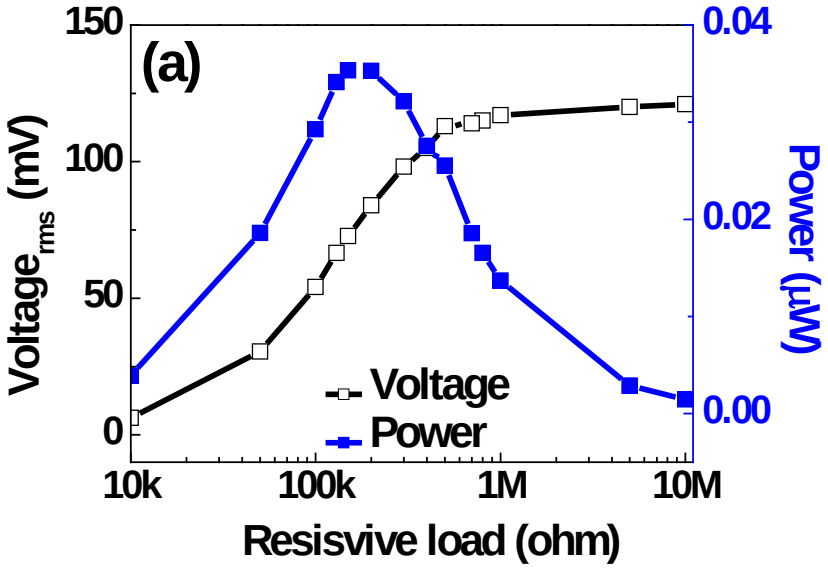

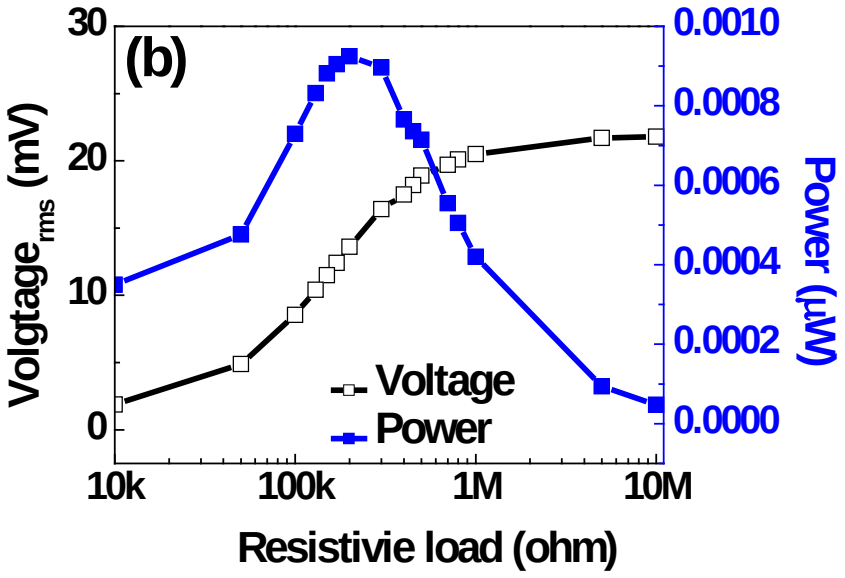

Figure 7.3 Output power and voltage as a function of resistive load. (a) 1 W (b) 3 W Cu doped ZnO cantilever.

Table 7.2 Resistivity of 1 W and 3 W Cu doped ZnO at device scale.

	Resisitivty (ohm-m)
1 W Cu doped ZnO	1.6×10^{10}
3W Cu doped ZnO	8.2×10^{8}

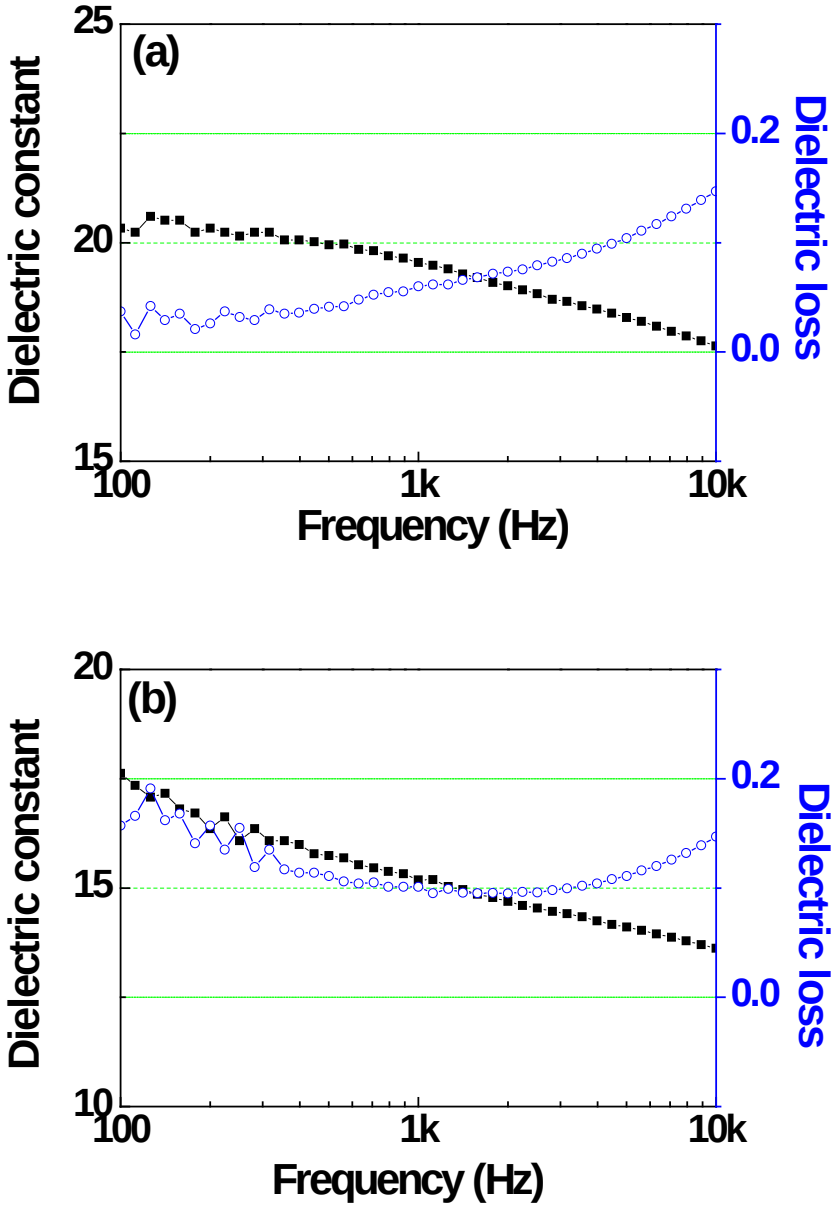

Figure 7.4 Electric property comparison in Cu doped ZnO cantilevers at ac field application. Dielectric constant and loss of (a) 1 W Cu doped ZnO cantilever (b) 3 W Cu doped ZnO cantilever.

Piezoelectric constant was estimated from dynamic vibration of cantilever based on equation (7.1). The equation (7.1) was derived from equation (4.22) by assuming infinite

resistance at open circuit condition. Dimensions, material parameters, and estimated piezoelectric constant d_{31} are summarized in table 7.3. Electromechanical coupling coefficient was determined from frequency vs. impedance measurement as given in figure 7.7 and equation (7.2), where f_a and f_r are anti-resonance and resonance frequency. The impedance was measured from only the 1W Cu doped ZnO due to negligible response from the 3 W Cu doped ZnO, so k_{31} of the 3 W Cu doped ZnO was substituted by that of the 1 W Cu doped ZnO. The estimated piezoelectric constant shows improvement of piezoelectric property by Cu doping and optimum Cu doping power is 1 W although the value is not exact.

Table 7.3 Piezoelectric constants and materials parameters for piezoelectric constant estimation.

		1 W Cu doping	3 W Cu doping
Fixed end to proof mass (m)	l_c	0.004	0.004
Length of proof mass (m)	l_{pm}	0.003	0.003
Neutral layer to center of piezoelectric layer (m)	l_{npu}	0.0000145	0.0000145
Geometrical factor	g_f^*	1.5225	1.5225
Young's modulus (Pa)	Y_{pc}	1.2E+11	1.2E+11
Resonant frequency (Hz)	f_r	342	339.67
Resonant angular frequency	ω_r	2148.848928	2134.209109
Thickness of piezoelectric layer (m)	t_{pc}	0.000001	0.000001
Dielectric constant	ε_r	23	17
Vacuum permitivitty (F/m)	ε_0	8.854E-12	8.854E-12
Open circuit voltage (V) ($V_{p-p}/2$)	V_{oc}	0.12	0.02
Damping ratio	ζ	0.00964826	0.00964826
Electromechanical coupling coefficient*	κ_{31}	0.077	0.077
Piezoelectric constant	d_{31}	1.24678E-11	1.51503E-12

*k_{31} of 3 W Cu doped ZnO is that of 1 W Cu doped ZnO.

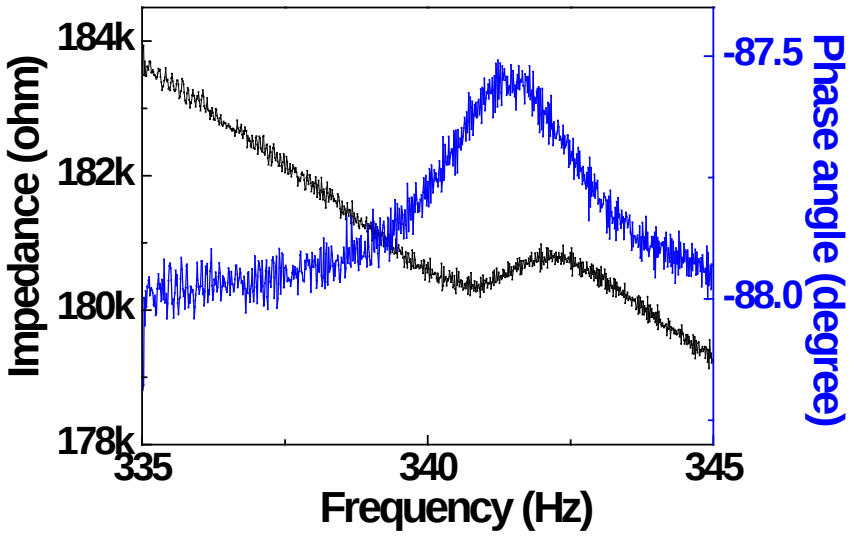

Figure 7.5 Impedance and phase angle measurement as a function of frequency.

$$V_{oc} = \frac{Y_{pc} d_{31} t_{pc} g_f^{*}}{\varepsilon_0 \varepsilon_r} \frac{1}{\sqrt{\omega_n{}^4 \kappa^4 + 4\zeta^2 \omega_n{}^4}} \tag{7.57}$$

$$k_{31} = \frac{\sqrt{\left(f_a^2 - f_r^2\right)}}{f_a} \tag{7.58}$$

7.4 Device evaluation by using oscillating magnetic force

Metglas based Cu doped ZnO cantilever was vibrated by oscillating magnetic force using the experimental setup described in figure 3.20. Since 1 W Cu doped ZnO produced the highest output, 1 W Cu doped ZnO cantilever was used in this evaluation. Working frequency range was measured by recording open circuit voltage with shaker's vibrating frequency sweep from 20 to 200 Hz. Acceleration value was 1.5 g and displacement of the shaker decreased exponentially as shown in figure 7.8. Figure 7.9 shows generated output voltage from 20 to 180

Hz and it shows that the device covers almost entire frequency range of vibration source in surroundings.

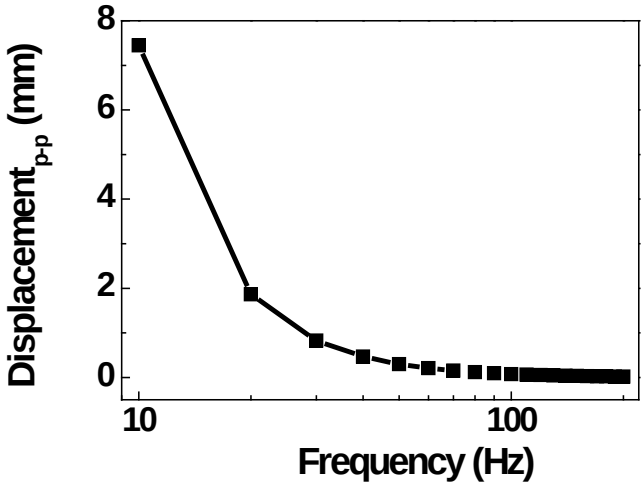

Figure 7.6 Displacement of shaker as a function of frequency at 1.5g vibration.

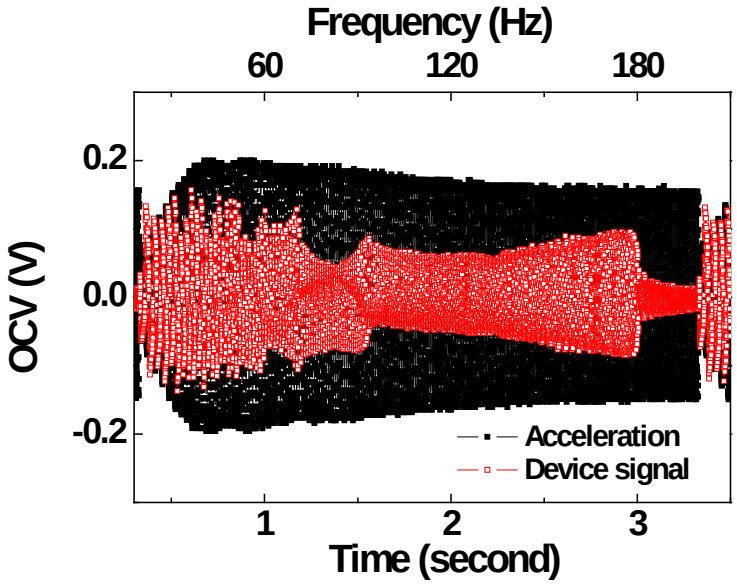

Figure 7.7 Frequency sweep from 20 to 200 Hz. Black and red square line denote signal from the accelerometer and the device, respectively.200 mV_{pk-pk} corresponds to 1g in the accelerometer.

Behavior of device was investigated by measuring output voltage from 20 to 180 Hz with 10 Hz interval of shaker's frequency as given in figure 7.10. The magnet was not vibrated from 0 to 20 Hz due to unstable vibration of the shaker. Output signal is mixture of shaker's frequency and first mode resonance frequency of cantilever at low frequency range (<100 Hz). The output signal begins to follow frequency of shaker from 100 Hz and phase difference between shaker and output voltage becomes bigger as shaker's frequency increases. The first mode resonance frequency represents free vibration of the cantilever because the cantilever is out of magnetic force range, i.e. in figure 7.11, the cantilever vibrates with the first mode resonance frequency after the magnet bounces the cantilever upward and moves up further. This assumption was verified by simulating the cantilever using MATLAB Simulink. The modeling does not consider exact parameters in the device, but aims simulation of wave shape of output voltage. Block diagram at 20 Hz is shown in figure 7.12. In block part 1, magnet on shaker is vibrated with sine wave and force exerted to cantilever is proportional to square of inverse of distance between the magnet and the cantilever. In block part 2, the cantilever was assumed as a linear spring-mass-damper model. The simulated wave form is given in figure 7.13, and the wave form is similar with the measured the output signal in figure 7.10

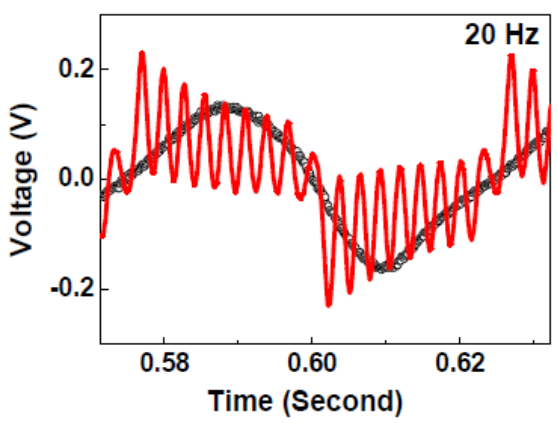
20 Hz
Voltage (V)
0.2
0.0
-0.2
0.58
0.60
0.62
Time (Second)

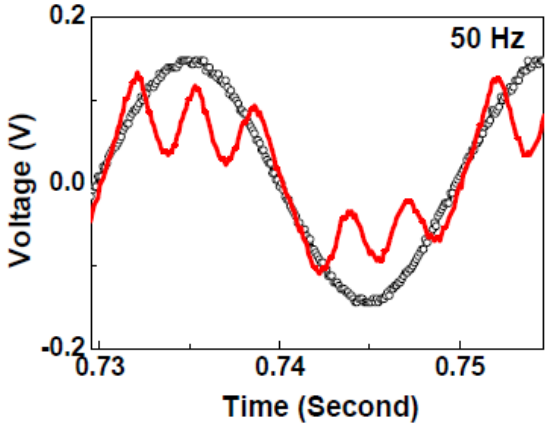
50 Hz
Voltage (V)
0.2
0.0
-0.2
0.73
0.74
0.75
Time (Second)

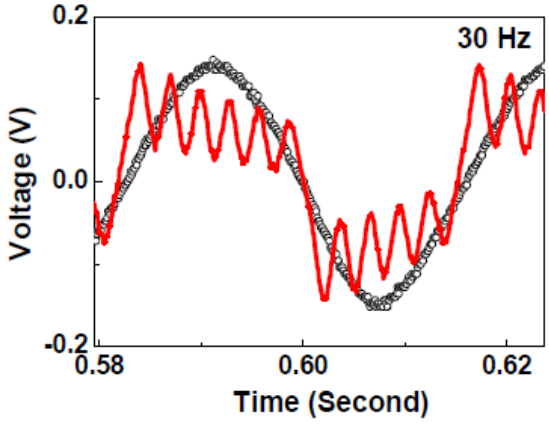
30 Hz
Voltage (V)
0.2
0.0
-0.2
0.58
0.60
0.62
Time (Second)

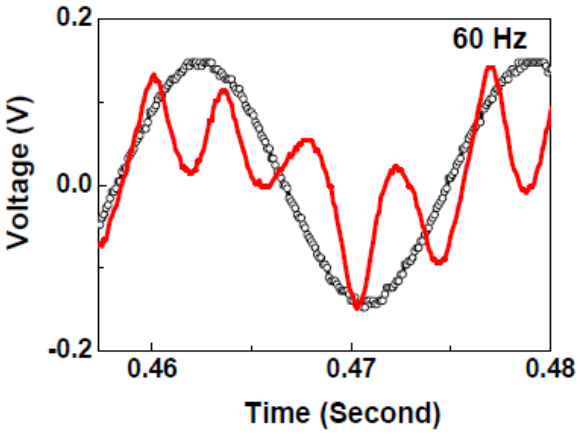
60 Hz
Voltage (V)
0.2
0.0
-0.2
0.46
0.47
0.48
Time (Second)

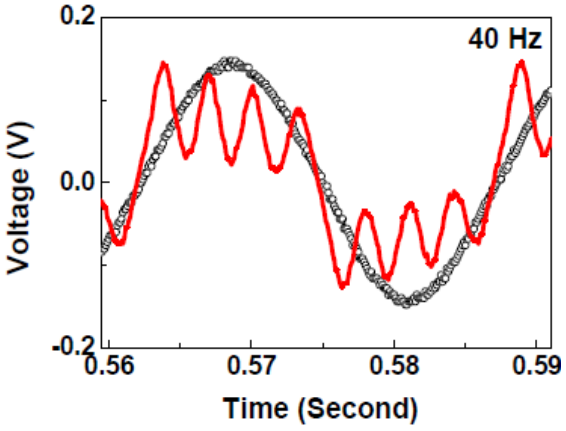
40 Hz
Voltage (V)
0.2
0.0
-0.2
0.56
0.57
0.58
0.59
Time (Second)

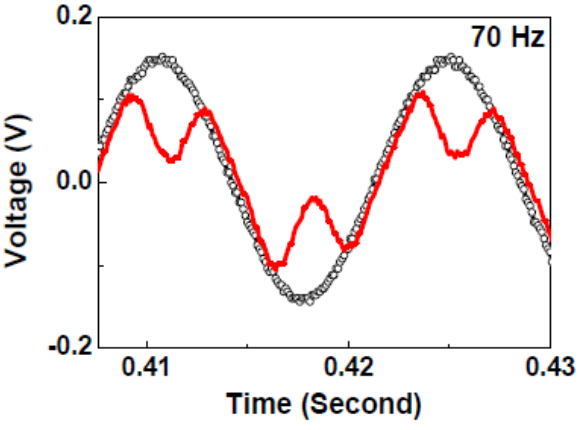
70 Hz
Voltage (V)
0.2
0.0
-0.2
0.41
0.42
0.43
Time (Second)

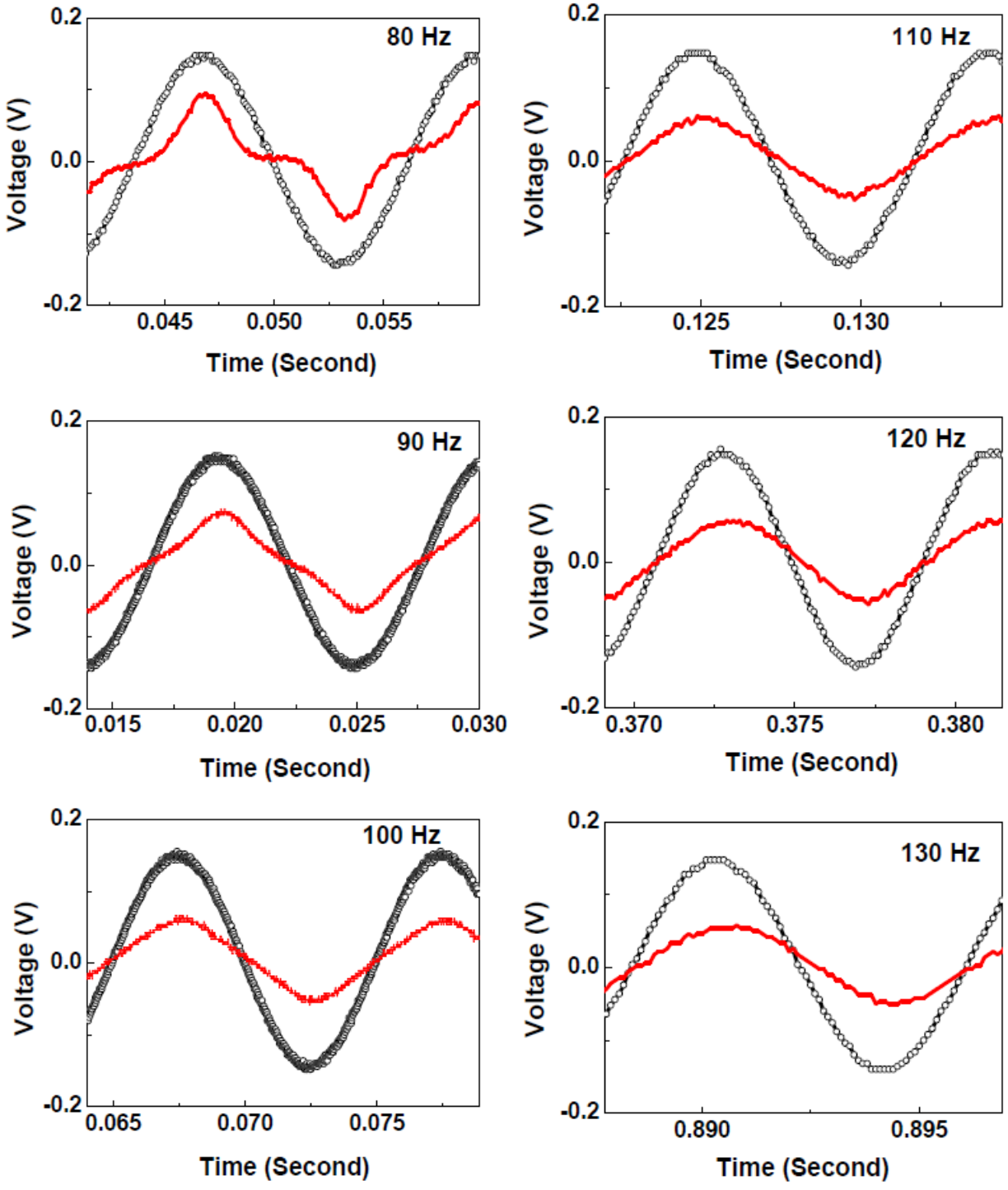
80 Hz
110 Hz
90 Hz
120 Hz
100 Hz
130 Hz
Voltage (V)
Time (Second)
0.2
0.0
-0.2
0.045
0.050
0.055
0.125
0.130
0.015
0.020
0.025
0.030
0.370
0.375
0.380
0.065
0.070
0.075
0.890
0.895

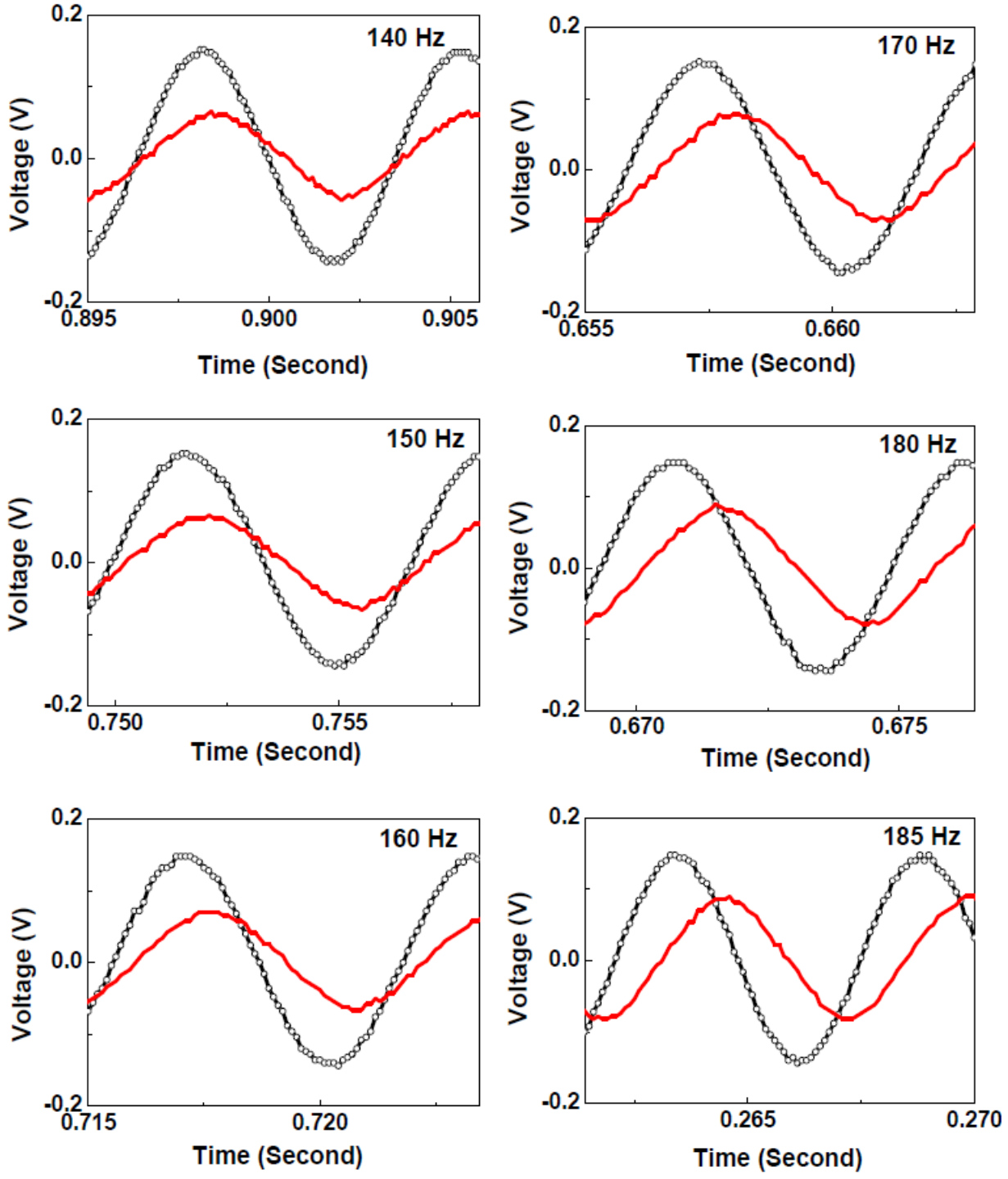

Figure 7.8 Output voltage (OCV) at various vibration frequency of the magnet. Black (open circle) and red line denote acceleration of shaker and device signal, respectively.

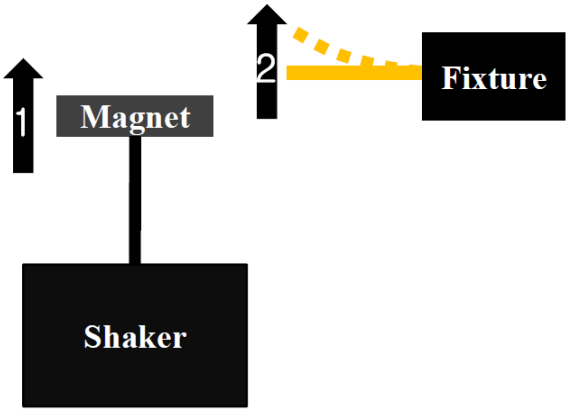

Figure 7.9 Motion of the shaker and response of the magnetic cantilever when the magnet moves from bottom to top.

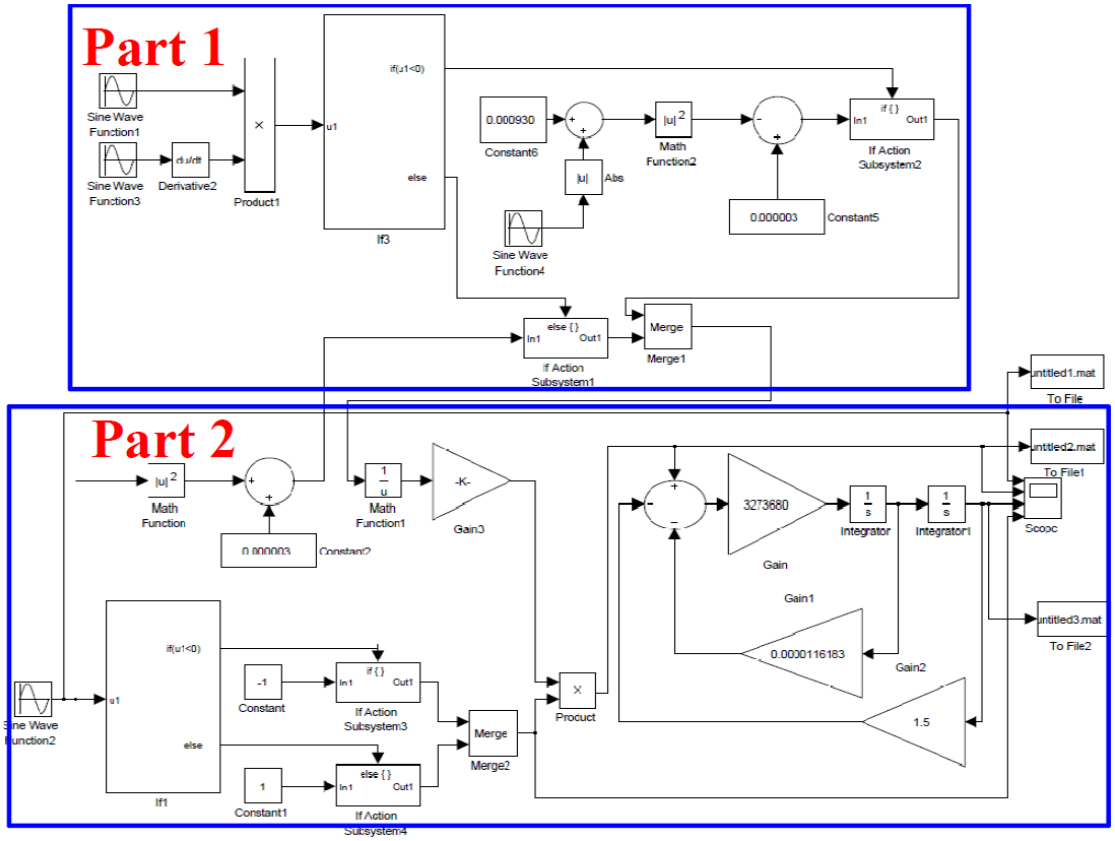

Figure 7.10 MATLAB Simulink block diagram for forced vibration of mass-spring model at 20 Hz.

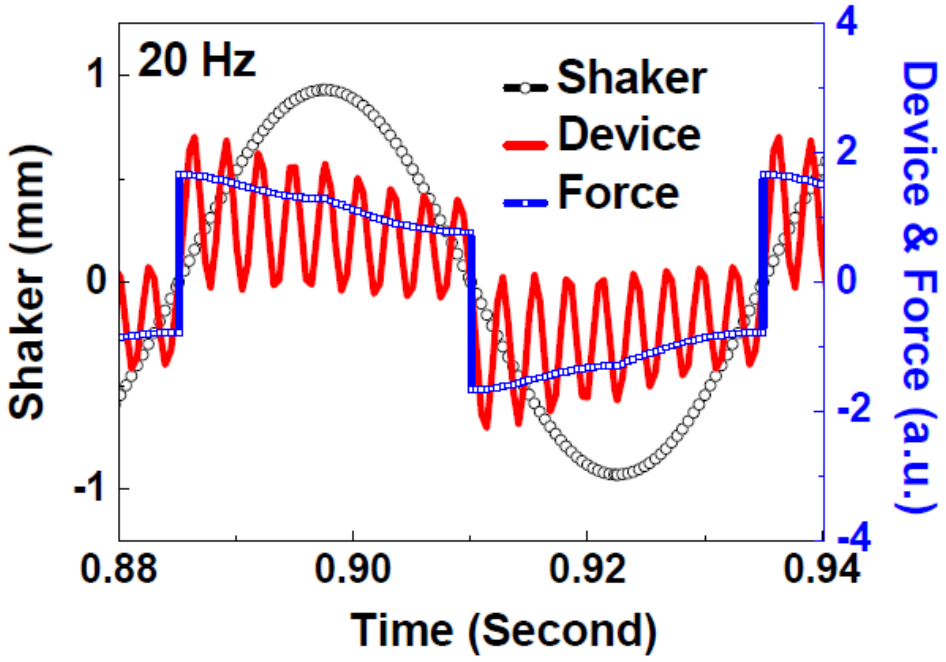

Figure 7.11 Simulated wave shape of output voltage at 20 Hz.

7.5 Conclusions

A PEH with wide working frequency range was studied by magnetic substrate based ZnO cantilever. Piezoelectric ZnO was obtained on amorphous substrate by Cu doping. Cu doping power was 1 W for the maximum power in the system. Behavior of cantilever was modeled by MATLAB Simulink assuming the cantilever as spring-mass-damper model. Output power was generated from 20 to 180 Hz, which covers almost entire frequency range of vibration source available from ambient.

CHAPTER 8 CONCLUSIONS AND FUTURE WORKS

8.1 Conclusions

Three subjects were studied for maximum output power density in a PEH. Temperature effect on the performance of PEH was investigated to prevent thermal degradation of output power. PEHs based on the d_{33} and d_{31} piezoelectric mode were compared to find a piezoelectric mode for maximum output power. A PEH was demonstrated to show output power generation in wide frequency range. The PEH was based on flexible magnetic substrate and vibrated by oscillating magnetic field.

To prevent performance degradation by environmental conditions, temperature effect on the output power of the PEH was investigated because temperature is the most influential factor in our surroundings. The temperature was increased from room temperature to 150 ˚C. Soft and hard PZT based bulk scale PEHs were compared as a function of temperature to find the most influential material parameter in the thermal degradation of the PEH. Those two bulk scale PEHs were compared with MEMS scale PEH to study size effect in the thermal degradation of PEH. As a result of the research, the dielectric constant was found as the most influential material parameter to the difference in the thermal degradation of soft and hard PZT based bulk scale PEH. In comparison between bulk and MEMS scale PEH, MEMS scale device showed a lower thermal degradation rate than bulk scale devices. The cause of the difference between the bulk and the MEMS scale devices was found to be the dielectric constant. Therefore, thermal degradation of PEH can be prevented by controlling the dielectric constant, i.e. suppression of dielectric constant increase.

MEMS PZT PEHs with d_{33} and d_{31} mode were fabricated, evaluated, and simulated to

investigate piezoelectric mode dependent performance of the PEH. Since a correct mathematical model for the d_{33} mode PEH has not been reported, a theoretical model for the d_{33} mode PEH was presented to predict output power of the d_{33} mode PEH and verified by the fabricated d_{33} mode devices. Output power of the d_{33} mode PEH should have increased continuously with finger spacing based on the previous model, but did not increase in the fabricated devices and mathematical model in this research due to the increase of defects responsible for ineffectiveness of poling. The maximum output power of the d_{33} mode PEH can be achieved when physical finger spacing is identical with effective finger spacing. The d_{33} and d_{31} mode based PEHs were compared in terms of output voltage and current. Output voltage and current were higher in the d_{33} and d_{31} mode device, respectively, due to large electrode spacing and electrode area, respectively. Comparing geometrical terms, electrode area and volume for power generation, in identical overall dimensions, the two terms are always higher in the d_{31} mode device than the d_{33} mode device because of dead layer underneath finger electrode in the d_{33} mode device. All of the fabricated d_{33} mode devices exhibited lower performance than the d_{31} mode PEH, but simulation showed the d_{33} mode PEH could generate higher power than the d_{31} mode device with reduced finger width. Therefore, the d_{33} mode device is superior in practical application ignoring fabrication issue because of high voltage enabling low loss during power transformation and higher power with ideal IDE design than the d_{31} mode PEH.

A PEH with wide working frequency range was demonstrated. The PEH was based on magnetic substrate and vibrated by oscillating magnetic field. Output power was produced from 20 to 180 Hz, which covers almost the entire frequency range available from ambient vibration source.

8.2 Future works

Future works are proposed to improve quality of research in this dissertation.

In the temperature effect study, there was relatively large difference in experiment and mathematical estimation. Refinement of output power model would reduce discrepancy with measurement, and analysis of thermal degradation will be more strongly supported by the mathematical equations.

In the piezoelectric mode effect study, the d_{33} and d_{31} mode devices were compared because it is difficult to fabricate a d_{15} mode PEH. However, it is not impossible to realize the d_{15} mode PEH. Fabrication of the d_{15} mode device would enable comparison of all available piezoelectric modes in the PEH.

In the study of a PEH with wide working frequency range, ZnO was used as a piezoelectric material. Piezoelectric constant of the ZnO has low piezoelectric constant, so output power was relatively low. The ZnO can be replaced with other piezoelectric materials having high piezoelectric constant to increase output power of the PEH.

REFERENCES

[1] X. Jiang, *et al.*, "Perpetual environmentally powered sensor networks," in *Information Processing in Sensor Networks, 2005. IPSN 2005. Fourth International Symposium on*, 2005, pp. 463-468.

[2] H. Long, *et al.*, "Battery allocation for wireless sensor network lifetime maximization under cost constraints," presented at the Proceedings of the 2009 International Conference on Computer-Aided Design, San Jose, California, 2009.

[3] W. Qin, *et al.*, "A Realistic Power Consumption Model for Wireless Sensor Network Devices," in *Sensor and Ad Hoc Communications and Networks, 2006. SECON '06. 2006 3rd Annual IEEE Communications Society on*, 2006, pp. 286-295.

[4] S. Chalasani and J. M. Conrad, "A survey of energy harvesting sources for embedded systems," in *Southeastcon, 2008. IEEE*, 2008, pp. 442-447.

[5] R. Vijay, *et al.*, "Design considerations for solar energy harvesting wireless embedded systems," in *Information Processing in Sensor Networks, 2005. IPSN 2005. Fourth International Symposium on*, 2005, pp. 457-462.

[6] K. A. Cook-Chennault, *et al.*, "Powering MEMS portable devices—a review of non-regenerative and regenerative power supply systems with special emphasis on piezoelectric energy harvesting systems," *Smart Materials and Structures*, vol. 17, p. 043001, 2008.

[7] S. Roundy, "On the effectiveness of vibration-based energy harvesting," *Journal of Intelligent Material Systems and Structures*, vol. 16, pp. 809-824, 2005.

[8] S. Roundy, *et al.*, "A study of low level vibrations as a power source for wireless sensor nodes," *Computer Communications*, vol. 26, pp. 1131-1144, 2003.

[9] P. D. Mitcheson, *et al.*, "Energy Harvesting From Human and Machine Motion for Wireless Electronic Devices," *Proceedings of the IEEE,* vol. 96, pp. 1457-1486, 2008.

[10] A. J. Moulson and J. M. Herbert, *Electroceramics: Materials, Properties, Applications*, 2nd ed.: John Wiley & Sons, Ltd, 2003.

[11] M. de Graef and M. McHenry, *Structure of Materials: An Introduction to Crystallography, Diffraction, and Symmetry*. Cambridge, UK: Cambridge University Press, 2007.

[12] T. C. Goel, *et al.,* "Processing and Dielectric Properties of Sol-Gel Derived PMN-PT (68:32) Thin Films," *Journal of Electroceramics,* vol. 13, pp. 503-507, 2004.

[13] C. Jagadish and S. Pearton, *Zinc oxide bulk, thin films and nanostructures: processing, properties and applications*: Elsevier Science Ltd, 2006.

[14] T. S. Low and W. Guo, "Modeling of a three-layer piezoelectric bimorph beam with hysteresis," *Jounal of Microelectromechanical Systems,* vol. 4, pp. 230-237, 1995.

[15] S. Ping, *et al.*, "Design and fabrication of PIN-PMN-PT single-crystal high-frequency ultrasound transducers," *Ultrasonics, Ferroelectrics and Frequency Control, IEEE Transactions on*, vol. 56, pp. 2760-2763, 2009.

[16] P. Srinivasan and S. M. Spearing, "Optimal Materials Selection for Bimaterial Piezoelectric Microactuators," *Microelectromechanical Systems, Journal of*, vol. 17, pp. 462-472, 2008.

[17] S. Tadigadapa and K. Mateti, "Piezoelectric MEMS sensors: state-of-the-art and perspectives," *Measurement Science and Technology,* vol. 20, p. 092001, 2009.

[18] J. George A. Rossetti, *et al.*, "Phase coexistence near the morphotropic phase boundary in lead zirconate titanate ($PbZrO_3$-$PbTiO_3$) solid solutions," *Applied Physics Letters*, vol. 88, p. 072912, 2006.

[19] V. Giurgiutiu and S. E. Lyshevski, *Micromechatronics: Modeling, analysis, and design*

with MATLAB vol. 10: CRC, 2009.

[20] B. Noheda, *et al.*, "A monoclinic ferroelectric phase in the $Pb(Zr_{1-x}Ti_x)O_3$ solid solution," *Applied Physics Letters,* vol. 74, pp. 2059-2061, 1999.

[21] R. Guo, *et al.*, "Origin of the High Piezoelectric Response in $PbZr_{1-x}TiO_3$," *Physical Review Letters,* vol. 84, pp. 5423-5426, 2000.

[22] Q. Tan, *et al.*, "Ferroelectric behaviours dominated by mobile and randomly quenched impurities in modified lead zirconatetitanate ceramics," *Philosophical Magazine Part B,* vol. 76, pp. 59-74, 1997/07/01 1997.

[23] I. Piezo Systems. (2011). *Piezo.com (Piezoceramic Application Data).*

[24] M. Hammer, *et al.*, "Correlation between Surface Texture and Chemical Composition in Undoped, Hard, and Soft Piezoelectric PZT Ceramics," *Journal of the American Ceramic Society,* vol. 81, pp. 721-724, 1998.

[25] S.-E. Park and T. R. Shrout, "Ultrahigh strain and piezoelectric behavior in relaxor based ferroelectric single crystals," *Journal of Applied Physics,* vol. 82, pp. 1804-1811, 1997.

[26] P. Muralt, "Recent Progress in Materials Issues for Piezoelectric MEMS," *Journal of the American Ceramic Society,* vol. 91, pp. 1385-1396, 2008.

[27] S. H. Baek, *et al.*, "Giant Piezoelectricity on Si for Hyperactive MEMS," *Science,* vol. 334, pp. 958-961, November 18, 2011 2011.

[28] D. Damjanovic, "Ferroelectric, dielectric and piezoelectric properties of ferroelectric thin films and ceramics," *Reports on Progress in Physics,* vol. 61, p. 1267, 1998.

[29] L. Wu, *et al.*, "Piezoelectric properties of modified PZT ceramics," *Journal of Physics C: Solid State Physics,* vol. 16, p. 2813, 1983.

[30] Q. M. Zhang, *et al.*, "Direct evaluation of domain-wall and intrinsic contributions to the

dielectric and piezoelectric response and their temperature dependence on lead zirconate-titanate ceramics," *Journal of Applied Physics,* vol. 75, pp. 454-459, 1994.

[31] U. Robels and G. Arlt, "Domain wall clamping in ferroelectrics by orientation of defects," *Journal of Applied Physics,* vol. 73, pp. 3454-3460, 1993.

[32] D. V. Taylor and D. Damjanovic, "Piezoelectric properties of rhombohedral Pb(Zr, Ti)O_3 thin films with (100), (111), and ``random" crystallographic orientation," *Applied Physics Letters,* vol. 76, pp. 1615-1617, 2000.

[33] F. Xu, *et al.*, "Domain wall motion and its contribution to the dielectric and piezoelectric properties of lead zirconate titanate films," *Journal of Applied Physics,* vol. 89, pp. 1336-1348, 2001.

[34] D.-J. Kim, *et al.*, "Evaluation of intrinsic and extrinsic contributions to the piezoelectric properties of Pb($Zr_{1-X}T_X$)O_3 thin films as a function of composition," *Journal of Applied Physics,* vol. 93, pp. 5568-5575, 2003.

[35] D. Shen, *et al.*, "Analysis of Piezoelectric Materials for Energy Harvesting Devices under High-g Vibrations," *Japanese Journal of Applied Physics,* vol. 46, p. 6755, 2007.

[36] V. Bedekar, *et al.*, "Comparative Study of Energy Harvesting from High Temperature Piezoelectric Single Crystals," *Japanese Journal of Applied Physics,* vol. 48, p. 091406, 2009.

[37] R. G. Sabat, *et al.*, "Temperature dependence of the complete material coefficients matrix of soft and hard doped piezoelectric lead zirconate titanate ceramics," *Journal of Applied Physics,* vol. 101, p. 064111, 2007.

[38] M. J. Schulz, *et al.*, "Piezoelectric Materials at Elevated Temperature," *Journal of Intelligent Material Systems and Structures,* vol. 14, pp. 693-705, November 1, 2003 2003.

[39] C. Miclea, *et al.*, "Effect of Temperature on The Main Piezoelectric Parameters of A Soft PZT Ceramic," *Romanian Journal of Information Science and Technology,* vol. 10, p. 8, 2007.

[40] R. A. Wolf and S. Trolier-McKinstry, "Temperature dependence of the piezoelectric response in lead zirconate titanate films," *Journal of Applied Physics,* vol. 95, pp. 1397-1406, 2004.

[41] S.-J. Jeong, *et al.*, "PROPERTIES OF A MULTI-STACK TYPE PIEZOELECTRIC ENERGY HARVESTING DEVICE," *Integrated Ferroelectrics,* vol. 98, pp. 208-215, 2008/06/13 2008.

[42] H. W. Kim, *et al.*, "Energy Harvesting Using a Piezoelectric "Cymbal" tansducer in Dynamic Environment," *Japanese Journal of Applied Physics,* vol. 43, p. 6178, 2004.

[43] S. Roundy, *et al.*, "Improving power output for vibration-based energy scavengers," *Pervasive Computing, IEEE,* vol. 4, pp. 28-36, 2005.

[44] D. Isarakorn, *et al.*, "The realization and performance of vibration energy harvesting MEMS devices based on an epitaxial piezoelectric thin film," *Smart Materials and Structures,* vol. 20, p. 025015, 2011.

[45] K. Morimoto, *et al.*, "High-efficiency piezoelectric energy harvesters of c-axis-oriented epitaxial PZT films transferred onto stainless steel cantilevers," *Sensors and Actuators A: Physical,* vol. 163, pp. 428-432, 2010.

[46] B. Ren, *et al.*, "Piezoelectric energy harvesting using shear mode $0.71Pb(Mg_{1/3}Nb_{2/3})O_3$-$0.29PbTiO_3$ single crystal cantilever," *Applied Physics Letters,* vol. 96, p. 083502, 2010.

[47] Y. K. Hong, *et al.*, "Single-Crystal Film Piezoelectric Sensors, Actuators and Energy Harvesters with Interdigitated Electrodes," *Ferroelectrics,* vol. 342, pp. 1-13, 2006/10/01

2006.

[48] W. Choi, *et al.*, "Energy harvesting MEMS device based on thin film piezoelectric cantilevers," *Journal of Electroceramics*, vol. 17, pp. 543-548, 2006.

[49] C. Bowen, *et al.*, "Optimisation of interdigitated electrodes for piezoelectric actuators and active fibre composites," *Journal of Electroceramics*, vol. 16, pp. 263-269, 2006.

[50] W. Beckert and W. S. Kreher, "Modelling piezoelectric modules with interdigitated electrode structures," *Computational Materials Science*, vol. 26, pp. 36-45, 2003.

[51] J. C. Park, *et al.*, "Modeling and Characterization of Piezoelectric d_{33}-Mode MEMS Energy Harvester," *Journal of Microelectromechanical Systems*, vol. 19, pp. 1215-1222, 2010.

[52] S.-E. Jo, *et al.*, "A resonant frequency switching scheme of a cantilever based on polyvinylidene fluoride for vibration energy harvesting," *Smart Materials and Structures*, vol. 21, p. 015007, 2012.

[53] H. Liu, *et al.*, "Investigation of a MEMS piezoelectric energy harvester system with a frequency-widened-bandwidth mechanism introduced by mechanical stoppers," *Smart Materials and Structures*, vol. 21, p. 035005, 2012.

[54] L. Gu, "Low-frequency piezoelectric energy harvesting prototype suitable for the MEMS implementation," *Microelectronics Journal*, vol. 42, pp. 277-282, 2011.

[55] J. W. Xu, *et al.*, "Right-angle piezoelectric cantilever with improved energy harvesting efficiency," *Applied Physics Letters*, vol. 96, p. 152904, 2010.

[56] I.-H. Kim, *et al.*, "Broadband energy-harvesting using a two degree-of-freedom vibrating body," *Applied Physics Letters*, vol. 98, p. 214102, 2011.

[57] V. R. Challa, *et al.*, "A vibration energy harvesting device with bidirectional resonance

frequency tunability," *Smart Materials and Structures,* vol. 17, p. 015035, 2008.

[58] F. Cottone, *et al.*, "Nonlinear Energy Harvesting," *Physical Review Letters,* vol. 102, p. 080601, 2009.

[59] S. C. Stanton, *et al.*, "Reversible hysteresis for broadband magnetopiezoelastic energy harvesting," *Applied Physics Letters,* vol. 95, p. 174103, 2009.

[60] A. Erturk, *et al.*, "A piezomagnetoelastic structure for broadband vibration energy harvesting," *Applied Physics Letters,* vol. 94, p. 254102, 2009.

[61] A. Hajati and S.-G. Kim, "Ultra-wide bandwidth piezoelectric energy harvesting," *Applied Physics Letters,* vol. 99, p. 083105, 2011.

[62] X. Dai, *et al.*, "Tuning of nonlinear vibration via topology variation and its application in energy harvesting," *Applied Physics Letters,* vol. 100, p. 031902, 2012.

[63] J. W. Yi, *et al.*, "Effect of length, width, and mode on the mass detection sensitivity of piezoelectric unimorph cantilevers," *Journal of Applied Physics,* vol. 91, pp. 1680-1686, 2002.

[64] J.-H. Park, "Development of MEMS Piezoelectric Energy Harvesters," Ph. D, Materials Engineering, Auburn University, Auburn 2010.

[65] Metglas. (2012, Technical Bulletin (2826MB). *2012 (Mar. 2012),* http://www.metglas.com/downloads/2826mb.pdf.

[66] Q.-M. Wang and L. E. Cross, "Determination of Young's modulus of the reduced layer of a piezoelectric RAINBOW actuator," *Journal of Applied Physics,* vol. 83, pp. 5358-5363, 1998.

[67] R. Igreja and C. J. Dias, "Analytical evaluation of the interdigital electrodes capacitance for a multi-layered structure," *Sensors and Actuators A: Physical,* vol. 112, pp. 291-301, 2004.

[68] F. F. C. Duval, *et al.*, "Fabrication and modeling of high-frequency PZT composite thick film membrance resonators," *Ultrasonics, Ferroelectrics and Frequency Control, IEEE Transactions on*, vol. 51, pp. 1255-1261, 2004.

[69] H. L. Pan, *et al.*, "Electrical properties and stability of p-type ZnO film enhanced by alloying with S and heavy doping of Cu," *Applied Physics Letters*, vol. 97, p. 142101, 2010.

[70] S.-N. Chen, *et al.*, "Analytical modeling of piezoelectric vibration-induced micro power generator," *Mechatronics*, vol. 16, pp. 379-387, 2006.

[71] X.-Y. Zhang, *et al.*, "Ferroelectric $Ba_xSr_{1-x}TiO_3$ thin-film varactors with parallel plate and interdigital electrodes for microwave applications," *Journal of Applied Physics*, vol. 104, p. 124110, 2008.

[72] W. C. Goh, *et al.*, "Pseudo-epitaxial lead zirconate titanate thin film on silicon substrate with enhanced ferroelectric polarization," *Applied Physics Letters*, vol. 87, p. 072906, 2005.

[73] Y. Jeon, *et al.*, "Residual Stress Analysis of Pt Bottom Electrodes on $ZrO_2/SiO_2/Si$ and SiO_2/Si Substrates for $Pb(ZrTi)O_3$ Thick Films," *Japanese Journal of Applied Physics*, vol. 39, p. 2705, 2000.

[74] D. V. Taylor and D. Damjanovic, "Piezoelectric properties of rhombohedral $Pb(Zr,Ti)O_3$ thin films with (100), (111), and random crystallographic orientation," *Applied Physics Letters*, vol. 76, pp. 1615-1617, 2000.

[75] W. Beckert and W. S. Kreher, "Modelling piezoelectric modules with interdigitated electrode structures," *Computational Materials Science*, vol. 26, pp. 36-45, 2003.

[76] C. H. Cheng, *et al.*, "Effect of poling conditions on out-of-plane displacement for a shear mode PZT actuator," *Sensors and Actuators A: Physical*, vol. 126, pp. 386-395, 2006.

[77] S. Buhlmann, *et al.*, "Polarization reversal due to charge injection in ferroelectric films,"

Physical Review B, vol. 72, p. 214120, 2005.

[78] I. Stolichnov and A. Tagantsev, "Space-charge influenced-injection model for conduction in $Pb(Zr_xTi_{1-x})O_3$ thin films," *Journal of Applied Physics,* vol. 84, pp. 3216-3225, 1998.

[79] G. Han, *et al.*, "Experimental investigation on the effect of top electrode diameter in PZT thick films," *Materials Letters,* vol. 65, pp. 2193-2196, 2011.

[80] U. Boettger, *et al.*, "The influence of non-ferroelectric interface layers and inclusions on the imprint behavior of ferroelectric thin film capacitors," in *Applications of Ferroelectrics, 2007. ISAF 2007. Sixteenth IEEE International Symposium on*, 2007, pp. 32-34.

[81] H. Qu, *et al.*, "Nanoscale polarization manipulation and conductance switching in ultrathin films of a ferroelectric copolymer," *Applied Physics Letters,* vol. 82, pp. 4322-4324, 2003.

[82] D. Liu, *et al.*, "Determination of the True Young's Modulus of $Pb(Zr_{0.52}Ti_{0.48})O_3$ Films by Nanoindentation: Effects of Film Orientation and Substrate," *Journal of the American Ceramic Society,* vol. 94, pp. 3698-3701, 2011.

[83] C. Ayela, *et al.*, "Determination of the d[sub 31] piezoelectric coefficient of $PbZr_xTi_{1-x}O_3$ thin films using multilayer buckled micromembranes," *Journal of Applied Physics,* vol. 100, p. 054908, 2006.

[84] P. Muralt, "PZT thin films for microsensors and actuators: Where do we stand?," *IEEE Transactions on Ultrasonics, Ferroelectrics and Frequency Control,* vol. 47, pp. 903-915, 2000.

[85] J. F. Shepard Jr, *et al.*, "The wafer flexure technique for the determination of the transverse piezoelectric coefficient (d_{31}) of PZT thin films," *Sensors and Actuators A: Physical,* vol. 71, pp. 133-138, 1998.

[86] F. Xu, *et al.*, "Longitudinal piezoelectric coefficient measurement for bulk ceramics and

thin films using pneumatic pressure rig," *Journal of Applied Physics*, vol. 86, pp. 588-594, 1999.

[87] C. L. Zhang and W. Q. Chen, "A wideband magnetic energy harvester," *Applied Physics Letters*, vol. 96, p. 123507, 2010.

[88] T.-D. Onuta, *et al.*, "Energy harvesting properties of all-thin-film multiferroic cantilevers," *Applied Physics Letters*, vol. 99, p. 203506, 2011.

[89] G. Ferblantier, *et al.*, "Deposition of zinc oxide thin films for application in bulk acoustic wave resonator," *Sensors and Actuators A: Physical*, vol. 122, pp. 184-188, 2005.

[90] I. Sayago, *et al.*, "Structural studies of zinc oxide films grown by RF magnetron sputtering," *Synthetic Metals*, vol. 148, pp. 37-41, 2005.

[91] J.-B. Lee, *et al.*, "Relationships between material properties of piezo-electric thin films and device characteristics of film bulk acoustic resonators," *Thin Solid Films*, vol. 516, pp. 475-480, 2007.

[92] L. Schuler, *et al.*, "The Effect of Substrate Material and Postannealing on the Photoluminescence and Piezo Properties of DC-Sputtered ZnO," *Journal of Electronic Materials*, vol. 36, pp. 507-518, 2007.

[93] M. Nolan and S. D. Elliott, "The p-type conduction mechanism in Cu_2O: a first principles study," *Physical Chemistry Chemical Physics*, vol. 8, pp. 5350-5358, 2006.

[94] X. B. Wang, *et al.*, "Microstructure and properties of Cu-doped ZnO films prepared by dc reactive magnetron sputtering," *Journal of Physics D: Applied Physics*, vol. 38, p. 4104, 2005.

[95] X. B. Wang, *et al.*, "The influence of different doping elements on microstructure, piezoelectric coefficient and resistivity of sputtered ZnO film," *Applied Surface Science*,

vol. 253, pp. 1639-1643, 2006.

[96] M. Labeau, *et al.*, "Thin films of high-resistivity zinc oxide produced by a modified CVD method," *Thin Solid Films*, vol. 213, pp. 94-98, 1992.

[97] A. Hartmann, *et al.*, "Influence of Copper Dopants on the Resistivity of ZnO Films," *Surface and Interface Analysis*, vol. 24, pp. 671-674, 1996.

[98] R. Dingle, "Luminescent Transitions Associated With Divalent Copper Impurities and the Green Emission from Semiconducting Zinc Oxide," *Physical Review Letters*, vol. 23, pp. 579-581, 1969.